Karlsruhe Institute of Technology

Light–Matter Interactions in 2D Nanostructures and Chiral Cavities

Zur Erlangung des akademischen Grades eines
DOKTORS DER NATURWISSENSCHAFTEN (Dr. rer. nat.)

von der KIT-Fakultät für Physik
des Karlsruher Instituts für Technologie (KIT)
angenommene

DISSERTATION

von

M. Sc. David Dams

am Institut für Theoretische Festkörperphysik

Tag der mündlichen Prüfung:	12. Dezember 2025
Referent:	Prof. Dr. Carsten Rockstuhl
Korreferent:	Prof. Dr. Garnett Bryant

Abstract

This thesis investigates light–matter interactions in two-dimensional nanostructures and chiral optical cavities.

To this end, we first introduce `GRANAD` (Graphene NANoflakes with ADatoms), a differentiable tight-binding framework for simulating the optoelectronic response of finite nanostructures under classical electromagnetic illumination. Built within the JAX ecosystem, `GRANAD` enables automatic differentiation, GPU acceleration, and gradient-based inference of physical parameters. The framework unifies time- and frequency-domain treatments of optical response, incorporates non-Hermitian extensions for relaxation and dephasing, and supports common tight-binding models for materials such as graphene, hexagonal boron nitride, and topological model systems.

Applications illustrate `GRANAD`'s versatility in modeling nanostructure optoelectronics, fitting material parameters, and exploring exotic phenomena in topological systems. In particular, we show that spin angular momentum (SAM) selectivity naturally emerges in finite topological nanoflakes described by the Haldane model. Analysis of their linear optical response reveals a pronounced SAM sensitivity arising from the interplay between broken time-reversal symmetry and chiral edge states, which benefits from topological protection and may thus serve as a robust experimental platform.

As a next step in our investigation, we extend our theoretical framework beyond the semi-classical description of light to include intrinsically chiral nanostructures of molecular dimensions embedded in optical cavities that selectively interact with light of a given handedness. Such systems offer promising prospects for pharmaceutical applications, particularly in the design and control of chiral drugs. Whereas most previous studies have focused on idealized cavities containing a single enantiomeric species, we instead address the effects of cavity imperfections and the coexistence of molecules with opposite handedness.

Using a chiral Hopfield model that remains valid in the strong light–matter coupling regime, we develop a fully quantum mechanical description of the photonic degrees of freedom to capture the emergence of hybrid light–matter excitations, or polaritons. We analyze chirality-selective energy transfer processes and demonstrate that, energy transfer is suppressed in the deep strong coupling regime due to diamagnetic effects.

Zusammmenfassung

Diese Arbeit untersucht Licht-Materie-Wechselwirkungen in zweidimensionalen Nanostrukturen und chiralen optischen Resonatoren.

Zunächst wird `GRANAD` (Graphene NANoflakes with ADatoms) vorgestellt, ein differenzierbares Tight-Binding-Framework zur Simulation der optischen und elektronischen Antwort endlicher Nanostrukturen unter klassischer elektromagnetischer Beleuchtung. Entwickelt innerhalb des JAX-Ökosystems ermöglicht `GRANAD` automatische Differenzierung, Beschleunigung auf GPU und gradientenbasierte Inferenz physikalischer Parameter. Das Framework vereinheitlicht zeit- und frequenzbereichsbasierte Beschreibungen der optischen Antwort, integriert nicht-Hermitesche Erweiterungen zur Berücksichtigung von Relaxation und Dekohärenz und unterstützt gängige Tight-Binding-Modelle für Materialien wie Graphen, hexagonales Bornitrid und topologische Modellsysteme.

Anwendungsbeispiele illustrieren die Vielseitigkeit von `GRANAD` bei der Modellierung optoelektronischer Eigenschaften von Nanostrukturen, der Anpassung von Materialparametern und der Erforschung exotischer Phänomene in topologischen Systemen. Insbesondere zeigen wir, dass eine Selektivität des Spin-Drehimpulses (SAM) auf natürliche Weise in endlichen topologischen Nanoflocken auftritt, die durch das Haldane-Modell beschrieben werden. Die Analyse ihrer linearen optischen Antwort offenbart eine ausgeprägte SAM-Empfindlichkeit, die aus dem Zusammenspiel zwischen gebrochener Zeitumkehrsymmetrie und chiralen Randzuständen resultiert. Diese profitiert von topologischem Schutz und könnte somit als robuste experimentelle Plattform dienen.

Im nächsten Schritt erweitern wir unsere theoretische Betrachtung über die semiklassische Beschreibung des Lichts hinaus, um intrinsisch chirale Nanostrukturen molekularer Dimension zu berücksichtigen, die in optische Resonatoren eingebettet sind und selektiv mit Licht einer bestimmten Händigkeit wechselwirken. Solche Systeme bieten vielversprechende Perspektiven für pharmazeutische Anwendungen, insbesondere bei der Entwicklung und Kontrolle chiraler Wirkstoffe. Während sich die meisten bisherigen Studien auf idealisierte Resonatoren mit einer einzigen enantiomeren Spezies konzentriert haben, untersuchen wir stattdessen die Auswirkungen von Unvollkommenheiten in der Resonator und das gleichzeitige Vorhandensein von Molekülen mit entgegengesetzter Händigkeit.

Unter Verwendung eines chiralen Hopfield-Modells, das auch im Regime starker Kopplung zwischen Licht und Materie gültig bleibt, entwickeln wir eine vollständig quantenmechanische Beschreibung der photonischen Freiheitsgrade, um die Entstehung hybrider Anregungen aus Licht und Materie zu erfassen, sogenannter Polaritonen. Wir analysieren chiraliätsselektive Energietransferprozesse und zeigen, dass im Regime starker Kopplung der Energietransfer aufgrund diamagnetischer Effekte unterdrückt ist.

Publications

As part of the work on this thesis, I was involved in the research published in the peer-reviewed articles and conference contributions listed below.

Peer-reviewed articles

[P1] D. Dams and C. Rockstuhl, "Enantiomer selectivity and energy transfer in imperfect chiral cavities", Physical Review A **112**, 033707 (2025).

[P2] M. Pelc, D. Dams, A. Ghosh, M. Kosik, M. M. Müller, G. Bryant, C. Rockstuhl, A. Ayuela, and K. Słowik, "Single-particle approach to many-body relaxation dynamics", Physical Review A **109** (2024).

[P3] D. Dams and C. Rockstuhl, "Optical spin angular momentum sensitivity of topological nanoflakes", Physical Review B **111**, 235147 (2025).

[P4] D. Dams, M. Kosik, M. Müller, A. Ghosh, A. Babaze, J. Szczuczko, G. W. Bryant, A. Ayuela, C. Rockstuhl, M. Pelc, and K. Słowik, "Granad - simulating graphene nanoflakes with adatoms", Computer Physics Communications **317**, 109818 (2025).

Conference contributions

[C1] C. Rockstuhl, M. Pelc, D. Dams, A. Ghosh, M. Kosik, M. M. Müller, G. Bryant, A. Ayuela, and K. Słowik, "Understanding excitations in nano-antennas made from 2d-materials and hybrid systems", Conference talk (2024).

[C2] D. Dams, M. Kosik, M. Müller, A. Ghosh, J. Szczuczko, G. W. Bryant, A. Ayuela, C. Rockstuhl, M. Pelc, and K. Słowik, "GRANAD: simulating quantum optoelectronics at the nanoscale", Conference poster presentation (2024).

Contents

1. Introduction

By nanostructures, we refer to engineered systems whose relevant degrees of freedom are confined on the nanometer scale. They have become central platforms for studying and exploiting light–matter interactions [1]. Two-dimensional (2D) crystals and their heterostructures, in particular graphene [2], hexagonal boron nitride (hBN) [3], and transition-metal dichalcogenides (TMDCs) [4], offer atomically sharp control over optoelectronic properties [5] and have enabled a broad range of photonic and optoelectronic phenomena [6–9]. Tailoring light–matter coupling in such systems permits, for example, the manipulation of absorption and emission, the control of excitonic and plasmonic resonances [2, 9], and the design of nanoscale waveguides and resonators [6].

A closely related frontier is provided by topological materials. Chern insulators, first introduced at the model level by Haldane on the honeycomb lattice [10], exhibit quantized Hall conductance without net magnetic flux and host robust chiral edge states with striking transport and optical signatures [11, 12]. Experimental realizations span engineered ultracold fermionic [13], ferromagnetic [14], Moiré [15], localized spin systems [16], or buckled Xene monolayers such as silicene, germanene, stanene, and plumbene [17]. These realizations provide an avenue to capitalize on topological phenomena, such as edge currents, in the realm of materials design. The interplay between topology, finite-size effects, and optical driving provides a rich setting for theory and simulation [18] [19].

At nanoscopic length scales, electronic structure and optical response are governed by quantum mechanics. Classical continuum models miss essential ingredients such as quantum confinement, lattice termination, and orbital-scale selection rules. Reliable predictions therefore require microscopic approaches able to resolve atomic lattices, localized orbitals, and their couplings [20] [19].

A wide spectrum of simulation tools exists, trading off accuracy, interpretability, and computational cost. On one end, *ab initio* electronic-structure packages (*e.g.*, `VASP` [21], `SIESTA` [22], `Quantum ESPRESSO` [23], `Turbomole` [24]) provide first-principles accuracy at the expense of substantial computational resources and limited transparency for analytical exploration [19]. Their scaling with system size and the complexity of repeated parameter sweeps can be prohibitive for large nanostructures or when extensive model variation is required.

Between first-principles and minimal models lies density-functional tight binding, as implemented *e.g.* by `DFTB+` [25], a well-established “bridging” methodology that downfolds DFT information into a reduced basis while retaining self-consistency and access to a range of observables [26]. At the other end of the spectrum, *parametric* tight-binding (TB) models emphasize physical intuition, compactness, and speed [19]. They are particularly well suited for exploring finite-size and edge effects, disorder, transport, and topological quantities while permitting rapid hypothesis testing.

A mature ecosystem of TB codes now supports diverse use cases and numerical strategies.

Packages such as `Kwant` [27] and `KITE` [28] cover electronic transport, large sparse systems, and spectral methods including the kernel polynomial method (KPM). The `pythtb` [29] package provides a concise interface for Bloch-band and Berry-phase calculations, while tools like `pybinding` [30] focus on the rapid construction and manipulation of large finite or periodic TB models. Many codes are implemented in Python [31] atop the `NumPy` [32] and `SciPy` [33] stack, reflecting Python's central role in scientific computing.

In parallel with advances in machine learning, *differentiable programming* has emerged as a unifying paradigm. For physics, this enables gradient-based fitting of model parameters to data, sensitivity analysis, and the integration of neural networks with physics-informed components. In condensed-matter simulations, automatic differentiation (AD) unlocks derivative-based observables (*e.g.*, polarizabilities as Hessians of the ground-state energy) and efficient parameter inference and optimization under physical constraints.

To capitalize on these opportunities, we developed `GRANAD` (GRAphene NANoflakes with ADatoms) [P4], a simulation framework for nanostructure optoelectronics combining an ergonomic high-level interface with an efficient numerical backend. Developed in collaboration among the Institute of Theoretical Solid State Physics at KIT, the Institute of Physics at Nicolaus Copernicus University in Toruń, the Donostia International Physics Center, and the Nanoscale Device Characterization Division at NIST, `GRANAD` has evolved into a general tight-binding platform for finite and periodic structures with a particular focus on hexagonal lattices. Built on JAX, it provides automatic differentiation, just-in-time compilation, and GPU acceleration.

Three design principles guide `GRANAD`: differentiable core routines enabling gradient evaluation of physical quantities and parameter fitting; a dual approach to optical response in time- and frequency-domain; and customizability and ergonomics for defining geometries, interactions, and extensions. While the default is tight binding, interfaces permit importing matrix elements from *ab initio* workflows. Relative to transport-focused (`Kwant`) or topology-oriented (`pythtb`) tools, `GRANAD` targets nanostructure *optoelectronics* with a strong emphasis on time-domain driven dynamics under classical illumination and frequency-domain correlation functions based on microscopic formulations.

Within this work, `GRANAD`'s frequency-domain engine is used to investigate the interplay between topology and optics by studying *spin–angular–momentum (SAM)–selective* coupling of light to finite topological structures. We uncover SAM selectivity in finite Haldane nanoflakes by evaluating dipole–dipole and current–current correlators and projecting the induced response onto the channels responsible for chiral charge transport. This microscopic formulation connects intuitive edge-current physics to measurable differential spectra under circularly polarized illumination. The resulting SAM-selective resonances are traced to transitions among mid-gap edge states, exhibit systematic size scaling, and remain resilient under geometric symmetry breaking and random onsite perturbations.

The theoretical and numerical tools presented so far are tailored to cases where the external electromagnetic illumination can be treated as a *classical* field. For many nanophotonic and material-design problems, this approximation provides an accurate and tractable description. However, there exists a growing class of systems where the electromagnetic field must be treated *quantum mechanically*. Such situations arise when field quantization plays an essential role in determining material properties or when light–matter interactions enter regimes beyond perturbative coupling, most notably in the domain of *chiral cavities*.

Chirality refers to the fundamental geometrical property of an object that cannot be superimposed onto its mirror image through any sequence of rotations and translations [34]. Many molecules exhibit chirality, making it central to biology [35], chemistry [36], and pharmacology [37]. In recent years, chirality has also become a key concept in nanophotonics and quantum optics, where structured light fields and nanophotonic environments enable selective interactions between optical modes of distinct helicities and chiral matter.

Substantial progress has been achieved both theoretically [38–47] and experimentally [48, 49] in the design of chiral optical cavities that selectively support photonic modes of specific handedness. Combined with emitters or molecular ensembles exhibiting intrinsic or externally controllable chirality [50, 51], these systems form the foundation of the emerging field of *chiral polaritonics*. In this field, strong or ultrastrong light–matter coupling in a chiral environment gives rise to hybrid quasiparticles, referred to as *chiral polaritons*, whose optical and chemical properties depend on the handedness of the underlying constituents.

The interplay between quantum electrodynamics and chirality opens prospects for applications such as enantioselective detection [43, 52], asymmetric energy transfer [53, 54], and reaction-rate enhancement [55–57]. Theoretical analyses also suggest possibilities for collective phenomena such as superradiance [58] and chirality-dependent photon transport [59]. This underscores the need for a fully quantum description.

A key hallmark of chiral polaritonics is the emergence of discriminatory ground-state energy splittings between enantiomeric species, predicted to persist even in the ultrastrong coupling regime [38]. However, limitations due to diamagnetic contributions and reduced effective coupling in the deep-strong regime [60, 61] remain underexplored, and practical imperfections such as cavity asymmetry or mixed enantiomeric content are rarely included.

To address these challenges, we extend the semiclassical framework underlying `GRANAD` to a fully quantum description of light–matter interactions in chiral environments. We detail the quantization of light in cavities and its coupling to matter, sketching the conceptual connection to the tight-binding formalism introduced earlier. This leads to a generalized Hopfield-type model forming the basis for a theoretical investigation of energy transfer and spectral properties in imperfect chiral cavities [P1]. The model captures both photonic and matter degrees of freedom, their mutual coupling, and the influence of chirality and asymmetries, enabling the analysis of polaritonic eigenmodes and their evolution from the weak to deep-strong coupling regimes.

This thesis is divided into seven chapters.

After introducing the general setting in the first chapter, we develops the semiclassical theoretical framework used throughout the work. It presents the tight-binding formalism as a versatile microscopic model for finite and periodic systems, supplemented by approximate treatment of electronic interactions beyond the independent-particle formalism.

In the third chapter, we introduce the `GRANAD` simulation framework and discuss its design principles, implementation, and capabilities.

The fourth chapter illustrates the use of `GRANAD` through applications to nanostructure optoelectronics. After validating standard linear-response benchmarks, the main section investigates SAM–selective optical coupling in finite topological nanoflakes.

In the fifth chapter, we extend the theoretical framework beyond the semiclassical regime to include quantum aspects of light–matter interaction, which we apply in the sixth chapter to the resulting chiral Hopfield model in the study of enantiomer selectivity and energy transfer in imperfect chiral cavities.

Finally, the seventh chapter provides the conclusion and outlook.

2. Theoretical Framework

In this chapter, we develop the theoretical framework to describe nanostrctures underlying `GRANAD`.

In the *time-domain*, electrons are described as *independent particles* (IP) moving under the influence of an effective *mean-field* potential generated by all other electrons, as well as external potentials. These external couplings may represent classical fields such as experimental electric probes, lattice vibrations, or magnetic fields. The corresponding evolution equation is formulated for the *one-particle reduced density matrix* (1RDM) of the nanostructure. This representation enables access to all *single-particle* observables, including experimentally relevant quantities such as the *current* and the *polarization*. Electron dynamics are desribed by a *master equation*, a standard tool in quantum optics and the theory of open systems. Using this tool grants access not only to *nonlinear* response, but also, in principle, to *non-equilibrium dynamics*, thereby lifting the requirement that the system return to its initial state after the perturbation.

In the *frequency domain*, however, we rely on the standard (equilibrium) linear-response formalism, where the *Green's function* encodes the system's response to external perturbations. This description can be systematically improved by using the *random phase approximation* (RPA), which allows the inclusion of electron-electron interactions beyond mean-field treatments.

Both approaches require operations on the matrix kernels of the involved operators, whose computational cost scales steeply with the size of the underlying basis set used to expand the electronic wave functions. To address this, we typically employ a minimal *tight-binding* basis set. A graphical summary of this dual approach is given in Figure 2.1.

The present chapter aims to clarify the technical terms highlighted above, presenting a selection of topics from condensed matter and open-systems theory. Emphasis is placed on pedagogical transparency to lay the groundwork for the computational implementation of the `GRANAD` simulation framework. Original derivations are usually relegated to the appendix, while standard results are stated with reference to the appropriate literature.

We begin with the independent-particle approximation, where electrons are described as occupying single-particle orbitals governed by an effective Hamiltonian. This perspective naturally leads to the second-quantized operator formalism and the construction of ground and excited states as Slater determinants. Building on this, the tight-binding approximation is introduced as a particularly useful representation for localized electronic systems such as graphene nanostructures, where it provides both physical transparency and computational efficiency [62].

The second part of the chapter turns to the reduced density matrix (RDM) formalism. The 1RDM emerges as a key quantity for evaluating single-particle observables and for

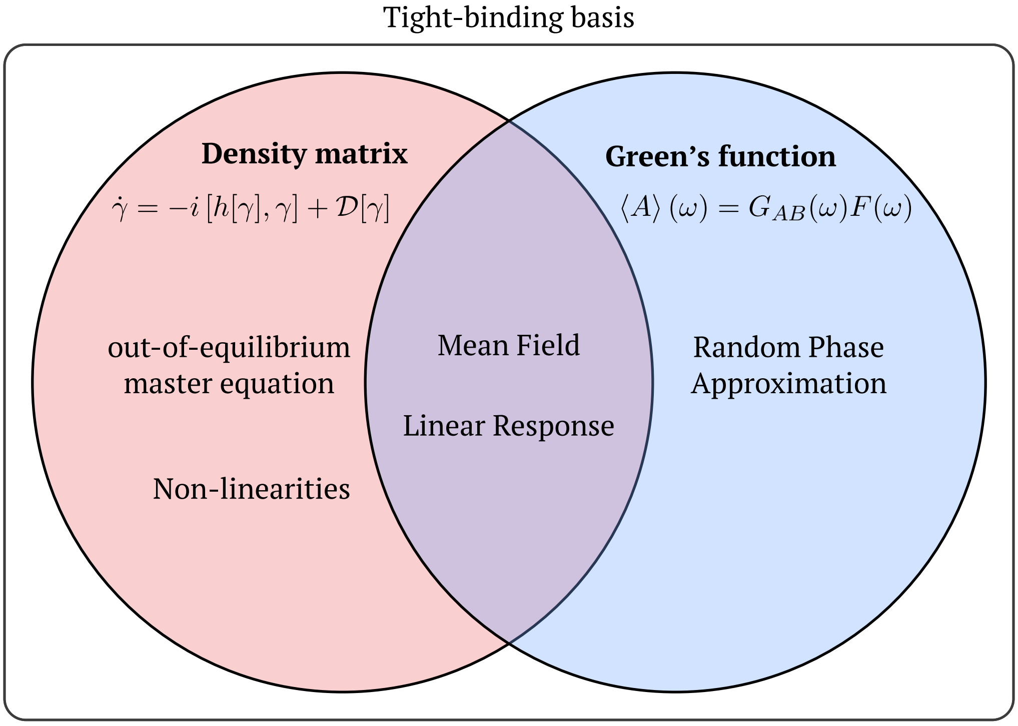

Figure 2.1.: Theoretical framework employed in this thesis: A complementary approach in both *time-* and *frequency-domain* is used. The real-time propagation of the *one-particle reduced density matrix* enables the study of *out-of-equilibrium* phenomena *via* an open-system *master equation*. On the other hand, the equilibrium *Green's function* unlocks genuine many-body effects *via* the *Random Phase Approximation*. Both of these pillars are unified in a *tight-binding* framework as the default basis adopted for theoretical transparency and computational efficiency.

describing time-dependent dynamics under external perturbations [P2]. Its equation of motion parallels the von Neumann equation and forms the basis for the time-domain simulation engine of `GRANAD`. To account for environmental effects and finite lifetimes, dissipative extensions in the form of phenomenological and Lindblad-type master equations are introduced.

We then connect this formalism to response theory, which provides a systematic framework to calculate the linear and non-linear response of quantum systems to weak external fields [63]. Central results such as the Lehmann representation, frequency-domain correlators, and sum rules are discussed, highlighting the fundamental role of causality and gauge invariance [64].

Finally, we extend the discussion to include electron–electron interactions. Starting from the Coulomb two-body operator, we motivate the mean-field approximation as a computationally accessible approach that replaces the full interacting problem with an effective single-particle Hamiltonian. Its time-dependent extension closes the BBGKY hierarchy and enables tractable dynamical simulations [65]. Beyond mean-field, we outline the RPA, which incorporates collective Coulomb effects in the frequency domain and provides access to optical response functions of interacting systems [63].

The methodological framework to be described in this chapter constitutes the basis for all the work discussed in the upcoming chapters.

2.1. Independent Particles

The starting point of most quantum mechanical calculations is the solution of the time-independent Schrödinger equation to find the eigenvalues E and eigenstates ψ of the Hamiltonian operator H according to [63]

$$H\psi = E\psi \,. \tag{2.1}$$

We will neglect electronic interactions for now and consider an IP system of N particles as the foundation of our theoretical analysis. In this case, the Hamiltonian can be written as a sum of kinetic and potential energy operators acting separately on each electron

$$H = \frac{1}{2m}\sum_{i=1}^{N} \boldsymbol{p}_i^2 + \sum_{i=1}^{N} V(\boldsymbol{x}_i) \,, \tag{2.2}$$

where m denotes the electronic mass and $V(\boldsymbol{x}_i)$ captures the influence of static external potentials, such as those generated by immobile atomic nuclei. The eigenvalue problem Equation (2.1) is typically approached by expanding the Hamiltonian in a convenient set of basis functions. Such basis functions are chosen to resemble physically meaningful single-particle states hosting one electron only. Depending on the system under study, the most apt choice is typically given by atomic orbitals [66], molecular orbitals, or plane waves [67]. Projecting the Hamiltonian onto the chosen basis set yields matrix elements of the form

$$h_{ab} = \langle a|H|b\rangle \ , \tag{2.3}$$

where $|a\rangle$ and $|b\rangle$ denote basis functions associated with single-particle states. The matrix h is often referred to as the Hamiltonian kernel. Using the formalism of *second quantization*, we can then find the spectrum of H purely algebraically by rewriting the Hamiltonian as [68]

$$H = \sum_{ij} h_{ij}\, c_i^\dagger c_j \,, \tag{2.4}$$

where $c_i^\dagger$ and c_j are fermionic ladder operators creating and annihilating electrons in single-particle states i and j and the sum runs over all basis elements. These operators obey the canonical anti-commutation relations [68]

$$\{c_i, c_j\} = \{c_i^\dagger, c_j^\dagger\} = 0 \,, \tag{2.5}$$

$$\{c_i, c_j^\dagger\} = \langle\phi_i|\phi_j\rangle \ , \tag{2.6}$$

$$c_i^\dagger \,|0\rangle = |\phi_i\rangle \ , \tag{2.7}$$

$$c_i \,|0\rangle = 0 \,, \tag{2.8}$$

where $|0\rangle$ denotes the vacuum state. In this thesis, we usually consider orthogonal single-particle states such that $\langle\phi_i|\phi_j\rangle = \delta_{ij}$. From Equation (2.5), it follows immediately that $c_i^2 = (c_i^\dagger)^2 = 0$, reflecting the Pauli exclusion principle. The matrix kernel h can now be diagonalized by a unitary transformation U, which defines a new set of operators

$$a_i = \sum_j U_{ij}\, c_j\,. \tag{2.9}$$

In this basis the Hamiltonian acquires the diagonal form

$$H = \sum_k \epsilon_k\, a_k^\dagger a_k\,, \tag{2.10}$$

where ϵ_k denotes IP energies, which we assume to be non-degenerate. We consider the associated single-particle states to be spinful, such that each state can carry either one or no electron in the zero-temperature ground state. The ground state energy E for the N -electron system is then given by adding the N lowest of these eigenvalues

$$E = \sum_{i=1}^{N} \epsilon_i\,. \tag{2.11}$$

The highest single-particle energy ϵ_N is often called the Fermi level and denoted by E_f. Heuristically, extended systems that allow for states arbitrarily close to the Fermi level are classified as metals, while systems with a gap separating the Fermi level from the manifold of unoccupied states exhibit insulating behavior. Consequently, the corresponding ground-state $|\psi\rangle$ fulfilling

$$E = \langle\psi|H|\psi\rangle\,, \tag{2.12}$$

is easily verified to be given by

$$|\psi\rangle = \prod_{i=1}^{N} a_i^\dagger\,|0\rangle\,. \tag{2.13}$$

In position space, $|\psi\rangle$ is a single Slater determinant, *i.e.* an antisymmetric N -electron wavefunction [68]. Every independent-particle Hamiltonian is characterized by a ground state of this kind. Excited states can be constructed analogously by populating higher-energy single-particle levels.

From a computational perspective, one of the principal challenges in electronic-structure theory is the size and structure of the matrix kernel h. The accuracy of numerical results depends crucially on the choice of basis set: a basis that is well adapted to the physical problem requires fewer elements to achieve convergence of observables [64]. In the next subsection, we will cover our approach to constructing a problem-adapted basis for the efficient and accurate description of nanostructures: the *tight-binding* approximation.

2.2. The Tight-Binding Approximation

In this section, we introduce the tight-binding approximation as a compact and physically transparent way to describe electronic structure in systems where electrons remain localized around atomic sites. It captures essential band features using only a few parameters, typically hopping amplitudes between neighboring orbitals. We then employ automatic differentiation to efficiently optimize the parameters of an exemplary tight-binding model for graphene against *ab initio* or experimental data, enabling systematic and reproducible model construction.

2.2.1. Theoretical Motivation

In many condensed-matter systems, electrons remain strongly localized in the vicinity of atomic cores. This observation motivates the *tight-binding* (TB) approximation [19], which employs a basis of localized orbitals with minimal spatial spread.

In practice, tight-binding Hamiltonians are often constructed semi-empirically based on either experimental data or more elaborate *ab initio* calculations [19], which typically employ large basis sets. A tight-binding Hamiltonian is constructed to reproduce the experimental or *ab initio* target data with a reduced number of parameters, called “hopping amplitudes”, often restricted to a frequency or energy range of interest. Since the fitting target already incorporates electronic interactions, the hopping parameters usually already contain electronic interactions to a degree. The resulting model describes an effective independent-particle ensemble and can not be clearly separated into, *e.g.* kinetic and interaction terms. The actual underlying Hamiltonian can thus not be recovered. As such, tight-binding is commonly not considered an *ab initio* method, but both conceptually transparent and computationally efficient.

For illustration, consider an infinite periodic solid described by an independent-particle Hamiltonian of the form

$$H = \sum_{ab} \sum_{\boldsymbol{R}_i, \boldsymbol{R}_j} h_{ab}(\boldsymbol{\Delta}_{ij})\, a_i^\dagger b_j \,, \tag{2.14}$$

where $\boldsymbol{R}_i$ denotes the lattice vectors, $\boldsymbol{\Delta}_{ij} = \boldsymbol{R}_i - \boldsymbol{R}_j$ the distance, or displacement, vector between sites, and $a_i^\dagger$ creates one of K localized single-particle states on site i. The matrix kernel h_{ab} is assumed to be a function of inter-orbital displacement only. We will take this expression to be the *ground truth*, an assumption that is not too far fetched in practice since many *ab initio* methods such as density functional theory (DFT) or Hartree-Fock (HF) generate “effective” independent-particle Hamiltonians of this kind [69]. As such, the number K of orbitals per atom might be very large, yielding a rather unwieldy kernel h_{ab} in orbital space with long-range spatial interaction. We want to capture the essential electronic information contained in h with a minimal tight-binding model requiring a smaller number of parameters. Tho this end, we introduce the Fourier transforms of the operators and matrix kernel,

$$a^\dagger_{\boldsymbol{k}} = \sum_i a^\dagger_i e^{-i\boldsymbol{k}\cdot\boldsymbol{R}_i} , \tag{2.15}$$

$$h_{ab}(\boldsymbol{k}) = \sum_i h_{ab}(\boldsymbol{R}_i) e^{-i\boldsymbol{k}\cdot\boldsymbol{R}_i} , \tag{2.16}$$

with $\boldsymbol{k}$ restricted to the first Brillouin zone. Now, the Hamiltonian can be written compactly in reciprocal space as

$$H = \sum_{ab} \sum_{\boldsymbol{k}} a^\dagger_{\boldsymbol{k}} b_{\boldsymbol{k}} \, h_{ab}(\boldsymbol{k}) , \tag{2.17}$$

where we keep and explicit summation over each wave vector $\boldsymbol{k}$. The Hamiltonian kernel $t_{ab}(\boldsymbol{k})$ can be diagonalized to yield the functions $\epsilon_i(\boldsymbol{k}), i \leq K$ characterizing the *band structure* of the solid. A tight-binding kernel approximating h can then be constructed in various ways. A common approach is to truncate the number of orbitals entering the ground-truth Hamiltonian in Equation (2.14). This is the conceptual underpinning of *Wannierization*, where a DFT Hamiltonian is expressed in a (maximally) localized basis and its sparsified version yields effective tight-binding Hamiltonians [19]. A prominent example is the description of graphene [70], where a simple nearest-neighbor p_z tight-binding model already captures the essential features of the low-energy band structure. Alternatively, one may diagonalize and fit a symmetry-constrained version of the Hamiltonian directly to the band structure, employing, *e.g.* the widely used Slater–Koster parametrization [71].

The resulting tight-binding models are not only applicable to bulk systems, but can also be transferred to finite or nanostructured geometries in real space. Importantly, the reduced dimensionality and sparsity of tight-binding Hamiltonians render them attractive for both conceptual analysis and large-scale numerical simulations. For these reasons, we adopt the tight-binding approximation as the working basis throughout this thesis.

In the next section, we provide a concrete demonstration of the tight-binding fitting procedure and its ability to accurately capture optoelectronic features of interest. To this end, we consider the case of graphene, one of the most widely studied two-dimensional materials.

2.2.2. Constructing Tight-Binding Models for Graphene

Graphene consists of a single layer of carbon atoms arranged in a two-dimensional honeycomb lattice. Each carbon atom has four valence orbitals. The in-plane sp^2 hybridized orbitals form strong σ bonds (from s, p_x, p_y), while the remaining p_z orbital contributes to the delocalized π -electron system. The p_z orbital is responsible for the low-energy electronic properties [72]. The π and π^* bands formed from p_z orbitals meet at the Fermi level, giving rise to the well-known Dirac cones at the K and K' points of the Brillouin zone [73]. Since these states dominate transport and optical phenomena near the Fermi level, a minimal tight-binding model for graphene typically retains only the p_z orbitals, as in [74] [62].

The honeycomb lattice can be understood as a triangular Bravais lattice with a two-atom basis. Choosing a lattice constant $a \approx 2.46$ Å (corresponding to a carbon–carbon distance $a_{\mathrm{CC}} \approx 1.42$ Å [75]), the primitive lattice vectors can be written as

$$\boldsymbol{a}_1 = a\left(\frac{1}{2}, \frac{\sqrt{3}}{2}\right) , \tag{2.18}$$

$$\boldsymbol{a}_2 = a\left(-\frac{1}{2}, \frac{\sqrt{3}}{2}\right) . \tag{2.19}$$

The reciprocal lattice is again hexagonal, spanned by the primitive vectors

$$\boldsymbol{b}_1 = \frac{2\pi}{a}\left(1, \frac{1}{\sqrt{3}}\right) , \tag{2.20}$$

$$\boldsymbol{b}_2 = \frac{2\pi}{a}\left(-1, \frac{1}{\sqrt{3}}\right) . \tag{2.21}$$

The first Brillouin zone is hexagonal with high-symmetry points conventionally denoted Γ, K, and M.

Restricting ourselves to p_z orbitals, the tight-binding Hamiltonian depends only on the relative displacement between carbon sites. Assuming direction-independent hopping amplitudes t_i depending only on the distance $R_i = |\boldsymbol{R}_i|$, the Hamiltonian kernel in reciprocal space can be expressed as

$$h(\boldsymbol{k}) = \sum_{i=1}^{n} t_i e^{i\boldsymbol{k}\cdot\boldsymbol{R}_i} , \tag{2.22}$$

where $\boldsymbol{R}_i$ runs over the neighbor shells included in the model.

We compute the reference band structure using density-functional theory (DFT) within `Quantum ESPRESSO` [67] and fit a third-nearest-neighbor p_z tight-binding model to the π bands. To reduce the number of free parameters, we fix the on-site energy to zero, $t_0 = 0$, leaving three independent hopping amplitudes t_1, t_2, t_3. For a set of N $\boldsymbol{k}$ -points along a high-symmetry path, let $\epsilon_{\boldsymbol{k}}$ denote the DFT eigenenergies and $\tilde{\epsilon}_{\boldsymbol{k}}(p)$ the eigenvalues of Equation (2.22) parameterized by $p = (t_1, t_2, t_3)$. The quality of the fit is quantified by the mean squared error

$$e(p) = \frac{1}{N}\sum_{\boldsymbol{k}} |\epsilon_{\boldsymbol{k}} - \tilde{\epsilon}_{\boldsymbol{k}}(p)|^2 \, , . \tag{2.23}$$

We implement $\tilde{\epsilon}_{\boldsymbol{k}}(p)$ in the automatic-differentiation framework JAX [76], enabling efficient evaluation of the gradients $\partial e/\partial t_i$ and minimization of $e(p)$ *via* gradient descent. This optimization procedure is discussed in greater detail in subsection 3.5.1, where we cover the technical foundations of `GRANAD`.

The optimized hopping and overlap parameters obtained from the fit are summarized in

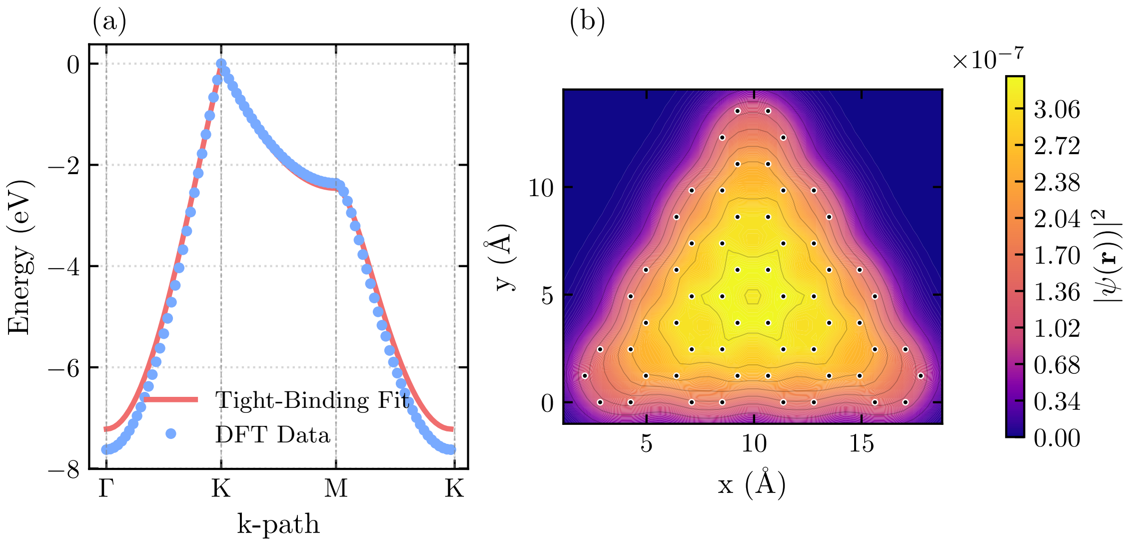

Figure 2.2.: **(a)** Tight-binding fit to the *ab initio* band structure of graphene obtained with `Quantum ESPRESSO`, constrained to p_z orbitals. The model retains hopping terms up to third-nearest neighbors in both the Hamiltonian and overlap matrix. Parameters are optimized by gradient descent using the procedure of automatic differentiation, detailed in the dedicated section of this thesis subsection 3.5.1. The Fermi level is located at $E_f = 0\,$eV. **(b)** Charge density $|\psi(\boldsymbol{r})|^2$ corresponding to the ground state Slater determinant $\psi(\boldsymbol{r})$ of an equilateral carbon nanotriangle with armchair edges and a side length of 15 Å. The calculation employs the tight-binding parameterization from (a).

Table 2.1.

Neighbor Index	Hopping (eV)	Overlap
0	0	1
1	-2.78	0.10
2	-0.36	0.003
3	-0.068	0.001

Table 2.1.: Tight-Binding Fit Parameters.

The fitted band structure is shown in Figure 2.2. The model successfully reproduces the Dirac cone at the K point and captures the essential features of the π bands, although discrepancies further away from the Fermi level remain, as expected from the truncated orbital basis. The fitted hopping parameters can then be used to investigate finite nanostructures. As an illustration, panel (b) of Figure 2.2 displays the ground-state charge density $|\psi(\boldsymbol{r})|^2$ of a triangular graphene flake with armchair edges and side length 15 Å, computed using the fitted tight-binding model.

For the majority of calculations in this thesis, we adopt an even more economical parameterization according to Tománek and Louie [70], in which only the nearest-neighbor hopping $t_1 \approx -2.66$ eV is retained. This value is close to the one extracted from our fit and suffices to reproduce the low-energy physics of graphene around the Fermi level with high fidelity.

In our model of nanostructures, we are interested in describing physical observables related to optoelectronic response in nanostructures like the graphene nanotriangle depicted in Figure 2.2. For instance, we might be interested in describing the dipole moment induced in such a nanostructure upon illumination with light. The dipole moment and many more of these physically relevant observables can be represented as *single-particle* operators, which we discuss in the next section.

2.3. Single-Particle Operators

In this section, we present single-particle operators as the foundation for describing measurable quantities in electronic systems. They share the same algebraic structure as the IP Hamiltonian considered so far, acting as matrix kernels on fermionic creation and annihilation operators. Within the tight-binding framework, these operators encode quantities such as charge polarization, current, and light–matter coupling in a compact, localized representation. After their theoretical introduction, we exemplify their use in mapping out localized edge currents in spatially finite system described by the well-known Haldane model for a Chern insulator.

2.4. Theoretical Setting

The form of the Hamiltonian Equation (2.4) is characteristic of any *single-particle operator* O, which can be written as a square matrix kernel multiplying fermionic ladder operators as follows

$$O = \sum_{ij} o_{ij} a_i^\dagger a_j \,. \tag{2.24}$$

Besides the Hamiltonian itself, other single-particle operators play a key role for the definition of phyiscally relevant observables. Of particular importance is the polarization operator

$$\boldsymbol{P} = e\boldsymbol{x} \,, \tag{2.25}$$

where e is the electronic charge. In a localized (tight-binding) basis, it takes the form

$$\boldsymbol{P}_{ij} = e \left\langle \phi_i | \boldsymbol{x} | \phi_j \right\rangle = e\delta_{ij}\boldsymbol{R}_i \,, \tag{2.26}$$

where $\boldsymbol{R}_i$ is the position of orbital i, taken to coincide with that of an atomic core. This expression is standard in many solid-state theory treatments. However, an additional contribution arises, when inter-orbital dipole matrix elements are non-negligible, such as in dipole-allowed transitions between orbitals i and j on the same atom. In this case, one must include a transition dipole moment $\boldsymbol{p}_{ij}$ [77], giving

$$\boxed{\boldsymbol{P}_{ij} = e\left(\delta_{ij}\boldsymbol{R}_i + \boldsymbol{p}_{ij}\right) \,.} \tag{2.27}$$

Closely related is the paramagnetic current operator, defined *via* the commutator [78]

$$\boxed{\boldsymbol{J} = -i[H, \boldsymbol{P}]\,.} \tag{2.28}$$

Its Cartesian components satisfy the canonical commutation relation

$$e^2\delta_{ij} = [P_i, J_j]\,. \tag{2.29}$$

These operators provide the foundation for describing physical observables such as induced currents and dipole moments. Coupling to external fields is naturally expressed in this operator language. An external classical electric field $\boldsymbol{E}(\boldsymbol{x}, t)$ couples to the polarization operator leading to a time-dependent single-particle interaction of the form [64]

$$O_{ij}(t) = \langle i|\boldsymbol{E}(\boldsymbol{x}, t)\boldsymbol{P}|j\rangle = \boldsymbol{E}(\boldsymbol{R}_i, t)\boldsymbol{P}_{ij}\,, \tag{2.30}$$

where we have again made use of maximum localization. The special case of a uniform electric field leads to the usual expression

$$O_{ij}(t) = \boldsymbol{E}(t)\boldsymbol{P}_{ij}\,, \tag{2.31}$$

A vector potential $\boldsymbol{A}$ couples to the current operator in the same way [72]. Additionally, vibrational interactions can be incorporated by allowing the Hamiltonian kernel to depend explicitly on the equilibrium nuclear positions $\boldsymbol{R}_0$ and on their deviations $\boldsymbol{d}(t)$. A Taylor expansion around the equilibrium configuration then yields

$$h(\boldsymbol{R}_0 + \boldsymbol{d}(t)) \approx h(\boldsymbol{R}_0) + \left.\frac{\partial h(\boldsymbol{R})}{\partial \boldsymbol{R}}\right|_{\boldsymbol{R}_0} \boldsymbol{d}(t) + \mathcal{O}\big(\boldsymbol{d}(t)^2\big)\,. \tag{2.32}$$

To lowest order in the displacements, the vibrational interaction is therefore represented by a single-particle operator with a matrix kernel given by

$$\boxed{O_{ij}(t) = \left.\frac{\partial h_{ij}(\boldsymbol{R})}{\partial \boldsymbol{R}}\right|_{\boldsymbol{R}_0} \boldsymbol{d}(t)\,.} \tag{2.33}$$

Couplings of the form given above provide the starting point for describing the dynamics of electrons in time-dependent or driven systems, a topic to which we turn when discussing linear response, where these operators enter as external perturbations. Building on the construction of the IP ground state in Equation (2.13), it is often convenient to express the operator kernels in the eigenbasis of the Hamiltonian. This is achieved through the transformation

$$\tilde{o} = U^\dagger o U\,. \tag{2.34}$$

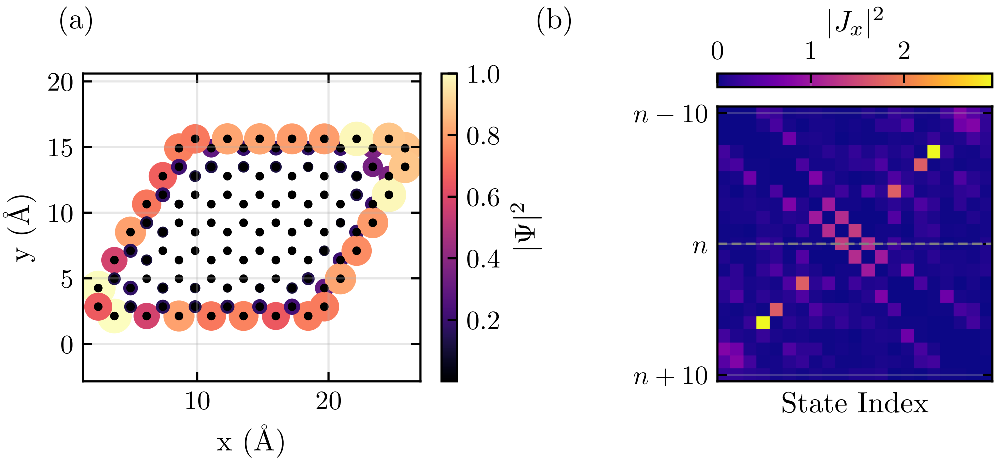

Figure 2.3.: **(a)** Example of a nanoflake described by the Haldane model with $\lambda = 0.3t$. This parameter choice yields a topological edge state, whose site-resolved probability density $|\Psi|^2$ is plotted on top of the atomic cores (black dots). Due to the maximum localization of the underlying basis set, we have omitted to indicate the explicit spatial dependence. **(b)** Transition matrix elements of the current operator J_x in the energy eigenbasis, depicted in a symmetric window around the highest occupied state at n. Large values near the Fermi level highlight transitions associated with edge states, which are analyzed in detail later.

In this representation, the matrix element $\tilde{o}_{nm}$ directly characterizes how the operator O acts on the IP transition between states n and m.

In the next subsection, we illustrate the analysis of single-particle operators in finite flakes described by the Haldane model, a *topological* variant of graphene.

2.4.1. Localized Currents in Haldane Graphene

Although topology is not the central focus of this thesis, we briefly sketch the relevant concepts in appendix B. In the following, we focus on the Haldane model [10] as a minimal and transparent realization of the most important characteristics. It modifies graphene by introducing time-reversal symmetry breaking through complex next-nearest-neighbor hoppings [19]

$$H = \delta \sum_i \chi_i a_i^\dagger a_i + t \sum_{\langle i,j \rangle} a_i^\dagger a_j + i\lambda \sum_{\langle\langle i,j \rangle\rangle} \nu_{ij} a_i^\dagger a_j \,, \tag{2.35}$$

Defining the indicator function $\chi_i = 1(-1)$ when i indices a site belonging to the A(B) sublattice, the first term represents a staggered sublattice potential δ, which opens a trivial gap by breaking inversion symmetry [79]. The second term describes nearest-neighbor hopping of strength t. The third term encodes next-nearest-neighbor hopping with amplitude λ, where the phase factor $\nu_{ij} = \pm 1$ depends on the hopping direction (clockwise or counterclockwise around a hexagon). This generates an effective local flux within each unit cell, though the total flux vanishes.

By setting $\delta = t$ and varying λ, the system undergoes a topological phase transition at $\lambda_c = \delta/(3\sqrt{3})$. For $\lambda < \lambda_c$, the insulator is topologically trivial. For $\lambda > \lambda_c$, the model enters a Chern insulating phase with Chern number $C = 1$. In this phase, the bulk–edge correspondence ensures the emergence of a topologically protected chiral edge mode. These states, which are eigenfunctions of the single-particle Hamiltonian (2.35), are spatially localized near the system's boundary and give rise to quantized anomalous Hall currents even in the absence of an external magnetic field [10].

In finite flakes, the detailed properties of the edge states depend sensitively on boundary termination. Zigzag edges typically support robust and well-localized modes, while armchair edges may hybridize or suppress them depending on the system size and symmetry [11, 12]. To capture the essential physics without additional complications, we focus on rhombic nanoflakes with zigzag edges, which emulate realistic graphene-based realizations of the Haldane model, for instance in substrate-induced spin–orbit systems [80]. The lattice constant is set to 1.42 Å, consistent with the carbon–carbon distance in graphene.

Figure 2.3 shows both a representative edge state in real space and the corresponding matrix elements of the paramagnetic current operator in the eigenbasis. The pronounced features near the Fermi level reflect transitions associated with edge states, which we will analyze in detail in 4.2.

In the next section, we turn to the central quantity for our time-domain modelling approach: the reduced density matrix.

2.5. Reduced Density Matrix Dynamics

Having established the operator framework for describing observables such as polarization and current, we now turn to the central quantity underpinning our time-domain modeling approach: the reduced density matrix. It provides a unified description of both equilibrium and nonequilibrium electronic behavior, capturing the statistical and dynamical properties of single-particle observables within a compact formalism. Through its evolution, we can efficiently model how electronic populations and coherences respond to external perturbations in real time.

2.5.1. Static Properties

A central object in the characterization of quantum systems is the density matrix. For a system in thermal and particle exchange with a reservoir characterized by chemical potential μ, this statistical operator is given by [81]

$$\rho = \frac{e^{-\beta(H-\mu N)}}{Z}\,, \tag{2.36}$$

where $N = \sum_i n_i$ denotes the total particle number operator, obtained by summing over all IP particle number operators. The inverse temperature is given by $\beta = 1/(k_B T)$, and

$Z = \text{Tr}[e^{-\beta(H-\mu N)}]$ is the grand canonical partition function ensuring normalization. Explicitly, the latter can be expressed as $Z = \sum_n e^{-\beta(E_n-\mu N)}$, with E_n denoting the eigenenergies of the Hamiltonian. Notably, the eigenenergies E_n ore *not* identical to the single-particle ones ϵ_i, even in the absence of interactions. Instead, for independent particles, they are given by the eigenvalues resulting from the application of the Hamiltonian H to single Slater-Determinants (cf. Equation (2.1) and Equation (2.13)).

In the zero-temperature limit ($\beta \to \infty$), the density matrix reduces to a projector onto the ground state,

$$\rho = |\psi\rangle \langle\psi| \ , \tag{2.37}$$

and the system is said to be in a *pure state*.

For any observable operator O, its expectation value follows from the trace over the density matrix,

$$\langle O\rangle = \text{Tr}[\rho O] \, . \tag{2.38}$$

Comparison with the independent-particle (IP) ground-state expression (cf.~Equation (2.13)) reveals that, even in the absence of interactions, ρ remains a many-body operator and cannot, in general, be reduced to a single-particle operator of the type discussed in Equation (2.24). Nonetheless, it is possible to introduce the one-particle reduced density matrix (1RDM),

$$\gamma_{ji} = \langle\psi|a_i^\dagger a_j|\psi\rangle \ , \tag{2.39}$$

which contains all the information required to evaluate expectation values of single-body operators. For instance, for a generic single-particle operator O, one obtain

$$\langle\psi|O|\psi\rangle = \sum_{ij} \gamma_{ij} o_{ji} = \text{Tr}[\gamma o] \, , \tag{2.40}$$

thus establishing γ as the relevant effective single-particle descriptor. From the definition Equation (2.39), it becomes immediately clear that the diagonal elements of γ are the expected IP occupation numbers.

$$\langle n_i\rangle = \gamma_{ii} \, . \tag{2.41}$$

In real space, γ_{ii} can thus be seen as the charge localized at the i -th site of the nanostructure. However, in the eigenbasis of the Hamiltonian, γ becomes diagonal. Inserting the expression for the Slater determinant ground state given by Equation (2.13) yields

$$\gamma_{ii} = \Theta(E_f - \epsilon_i) \, , \tag{2.42}$$

where ϵ_i denote the single-particle eigenenergies and E_f is the Fermi level. This expression can be extended to finite temperatures by replacing the step function with the Fermi–Dirac distribution [82]

$$\boxed{\gamma_{ii}(\beta) = \frac{1}{e^{\beta(\epsilon_i - \mu)} + 1}\,.} \tag{2.43}$$

The construction above implicitly considered a *spin-dependent* IP basis, with each element factorizing into a product of a single-particle orbital $|\psi_i\rangle$ and a spin function $|\chi_i\rangle$

$$|\phi_i\rangle = |\chi_i\rangle\,|\psi_i\rangle\ . \tag{2.44}$$

However, it is often not necessary to separately keep track of the spin degree of freedom. This may be the case if the underlying Hamiltonian does not include spin-resolved interactions and contains an even number of electrons, leading to the case where each orbital $|\psi_i\rangle$ can be considered doubly occupied. This is referred to as a *closed-shell* system and is aptly described by the *spin-traced* verison of the 1RDM, where the entries in Equation (2.43) are simply multiplied by a factor of two.

Next, we will investigate the dynamic behavior of the 1RDM.

2.5.2. Time-Dependent Dynamics

Many observables of interest in transport and condensed matter physics, such as electronic currents or polarizations, are fundamentally single-particle in nature. Their dynamics can, therefore, be captured by studying the time evolution of the 1RDM. Consider an independent-particle Hamiltonian subject to a possibly time-dependent perturbation,

$$H(t) = \sum_{ij} h_{ij}(t) c_i^\dagger c_j\,, \tag{2.45}$$

where the system is driven by the external field, *e.g.* an electromagnetic perturbation.

If the system is initially prepared in the ground state $|\psi\rangle$, its time evolution is governed by the unitary operator

$$|\psi(t)\rangle = U(t)\,|\psi\rangle\ , \tag{2.46}$$

$$U(t) = \mathcal{T} \exp\left[-i \int_{-\infty}^{t} \mathrm{d}t'\, H(t')\right]\,, \tag{2.47}$$

with $\mathcal{T}$ denoting the time-ordering operator. The evolution operator satisfies the equation,

$$i\,\partial_t U(t) = H(t) U(t)\,. \tag{2.48}$$

By exploiting Equation (2.48), one obtains

$$-i\,\partial_t \gamma_{ij}(t) = -i\,\partial_t \langle \psi(t)|a_i^\dagger a_j|\psi(t)\rangle = \langle \psi(t)|[\sum_{lm} h_{lm}(t) a_l^\dagger a_m, a_i^\dagger a_j]|\psi(t)\rangle \;. \tag{2.49}$$

Using

$$\begin{aligned}
\sum_{lm}[h_{lm}(t) a_l^\dagger a_m, a_i^\dagger a_j] &= \sum_{lm} h_{lm}(t) \left([a_l^\dagger, a_i^\dagger a_j] a_m + a_l^\dagger [a_m, a_i^\dagger a_j] \right) && (2.50)\\
&= \sum_{lm} h_{lm}(t) \left(-a_i^\dagger \{a_l^\dagger, a_j\} a_m + a_l^\dagger \{a_m, a_i^\dagger\} a_j \right) && (2.51)\\
&= \sum_{l} h_{li}(t) a_l^\dagger a_j - \sum_{m} h_{jm}(t) a_i^\dagger a_m \,, && (2.52)
\end{aligned}$$

finally yields the equation of motion for the 1RDM

$$-i\,\partial_t \gamma(t) = \big[h(t), \gamma(t)\big] \,, \tag{2.53}$$

which is of the same form as the von-Neumann equation governing the dynamics of the full density matrix. Thus, dynamical expectation values can be evaluated *via*

$$\boxed{\langle O \rangle\,(t) = \mathrm{Tr}[\gamma(t)\, o] \;.} \tag{2.54}$$

Equation (2.53) formally describes unitary, lossless evolution. While such an assumption is appropriate in idealized isolated systems, it is insufficient for realistic scenarios. Two main limitations arise:

1. **Environmental coupling**: physical systems interact with their surroundings, *e.g.* through electronic leads or internal relaxation channels.

2. **Spectral resolution**: purely coherent evolution results in δ-function–like features in the frequency domain, which are inconvenient both conceptually and numerically.

To address these issues, one typically introduces phenomenological broadening or dissipative terms, discussed in the next section.

2.5.3. Phenomenological and Microscopic Dissipation

A simple yet effective strategy is to include a damping factor directly in the observable [64]

$$\langle O \rangle\,(t) \;\rightarrow\; \langle O \rangle\,(t)\, e^{-\delta t} \,, \tag{2.55}$$

where $\delta > 0$ represents a broadening parameter mimicking finite lifetimes.

A more systematic approach involves modifying the dynamical equation of the 1RDM itself by adding a dissipator $\mathcal{D}$,

$$-i\,\partial_t\gamma(t) = [h(t), \gamma(t)] - \mathcal{D}[\gamma]\,. \tag{2.56}$$

This formulation naturally connects to the theory of *open quantum systems*, where such equations are known as *master equations*. Several forms of dissipators exist. A simple phenomenological variant reads [83]

$$\boxed{\mathcal{D}[\gamma(t)] = r\left(\gamma(t) - \gamma_0\right),} \tag{2.57}$$

where r is a real parameter capturing the dissipation rate in the system, and γ_0 denotes the reference 1RDM (often taken as the equilibrium state prior to the perturbation). This construction ensures relaxation towards initial configuration, described by γ_0. As discussed in section 2.6, this is a hallmark of an equilibrium process.

Alternatively, a more general and physically motivated choice is provided by the Lindblad form, widely employed in quantum optics and open-system theory [P2]

$$\boxed{\mathcal{D}[\gamma(t)] = \sum_{k=1}^{K^2-1} r_k \left(L_k\gamma(t)L_k^\dagger - \tfrac{1}{2}\{L_k^\dagger L_k, \gamma(t)\}\right),} \tag{2.58}$$

where $\{L_k\}$ are Lindblad operators representing different excitation or relaxation channels, r_k denotes the associated rate, and we have assumed a truncated single-particle basis of size K. This framework permits the incorporation of physically motivated dissipation pathways, including dephasing and relaxation, while preserving complete positivity and trace conservation of the density matrix. Its application and required modifications to fit within a single-particle framework are presented in detail in [P2]. As shown in appendix D, the phenomenological dissipator Equation (2.57) can be understood as a special case of the general Lindblad structure.

Armed with this understanding of density matrix dynamics, ranging from unitary evolution to dissipative open-system behavior, we are now prepared to develop the framework of linear response theory, which lies at the intersection of our time- and frequency-domain based analysis.

2.6. Response Theory

In this section, we turn to the framework of response theory to describe a quantum system under the influence of an external perturbations. Response theory connects microscopic Hamiltonian dynamics with measurable macroscopic quantities such as optical absorption, conductivity, and polarization. Within the independent-particle picture developed earlier, it enables us to quantify how external driving fields modify expectation values of single-particle observables in both the linear and nonlinear regimes. After discussing these theoretical fundamentals, we give an example of nonlinear response from the literature [83] and discuss sum rules, which express fundamental restrictions placed on the response functions of a structure imposed by gauge invariance.

2.6.1. Theoretical Fundamentals

We now turn to the framework of response theory, which provides a systematic description of how a quantum system reacts to external perturbations. Consider an independent-particle Hamiltonian $H = \sum_{ij} h_{ij} c_i^\dagger c_j$ subjected to a weak external field. The perturbation is taken to be of the form

$$H_{\text{int}} = F(t)A\,, \tag{2.59}$$

where $F(t)$ represents a classical time-dependent driving field, and A is a single-particle operator that couples the field to the system.

A central task is to determine how the expectation value of another observable B deviates from its equilibrium value due to the perturbation, expressed by Equation (2.59). To linear order in the driving field, one obtains the standard result of linear response theory (LRT) [63],

$$\delta b(t) \equiv \langle B \rangle (t) - \langle B \rangle = \int \mathrm{d}t'\, G_{AB}(t-t')F(t')\,, \tag{2.60}$$

where G_{AB} denotes the response function (or correlator, often referred to as the Green's function). The key assumption underlying Equation (2.60) is that the system returns to its initial (ground) state for asymptotically large times under the time evolution induced by the external perturbation [82]. Lifting this restriction enables the treatment of *non-equilibrium* processes, either by means of Master equations or within the non-equilibrium Green's function (NEGF) framework [63]. We briefly comment on this below. Physically, $G_{AB}(t-t')$ encodes the reaction of observable B to the field coupled through A, *e.g.* a polarization response leading to induced currents. In general, *causality* is ensured *via* the relation $G_{AB}(t-t') \sim \Theta(t-t')$, such that the response $\delta b(t)$ can not precede its external excitation $F(t)$. The above expression is naturally formulated in the Heisenberg picture with respect to the unperturbed Hamiltonian H. In the case where the operators A and B correspond to densities, an additional spatial integration or summation has to be performed [63].

For practical purposes, it is often advantageous to work in the frequency domain. Upon Fourier transformation, one obtains

$$\delta b(\omega) = G_{AB}(\omega)F(\omega)\,, \tag{2.61}$$

which directly expresses the frequency-resolved response of observable B to the driving field coupled *via* operator A.

The correlator admits the well-known *Lehmann representation*, expressed in the Schrödinger picture as [82]

$$\boxed{G_{AB}(\omega) = \lim_{\delta \to 0^+} \sum_{ij} \frac{\gamma_{ii} - \gamma_{jj}}{\omega + \epsilon_i - \epsilon_j + i\delta} A_{ij} B_{ji} \,,} \tag{2.62}$$

where the 1RDM γ has been expressed in the eigenbasis of h. In practice, the infinitesimal limit $\delta \to 0^+$ is never strictly taken; instead, δ is replaced by a small but finite broadening parameter to ensure numerical stability and physical line shapes. In general, singularities in $G(\omega)$ indicate *quasi-particle* excitations if they occur at $\omega \neq 0$. For instance, taking into account the direct Coulomb repulsion between electrons gives rise to singularities in the density-density correlator G_{nn} signalling the existence of *plasmons* [63], which we shall make use of in the following subsection. Singularities in the static Green's function generally signal a ground *ground-state* instability [82].

While the frequency-domain Green's function is the standard approach to linear response, it can be equivalently formulated in terms of the 1RDM. An alternative route to evaluating correlators is to solve the time-dependent 1RDM dynamics encoded in the master Equation (2.56) under the action of a weak driving field, compute the induced expectation value $\delta b(t)$, Fourier transform it, and then define [84]

$$\boxed{G_{AB}(\omega) = \frac{\delta b(\omega)}{F(\omega)} \,.} \tag{2.63}$$

It is worthwile to remark on the subtle difference between the response function computed above and the equilibrium correlator Equation (2.61): Dynamics modelled by master-equations generally go beyond the equilibrium setting as they do not assume the asymptotic final and initial states to coincide. For many practical purposes, however, an equilibrium description suffices and the linear-response functions computed from Equation (2.63) and Equation (2.61) coincide. A more in-depth detailed treatment of the technical difference between equilibrium and non-equilibrium response functions is given exhaustively in [82].

The advantage of Equation (2.63) is its straightforward generalization to the non-linear regime without the need for a systematic expansion in orders of the driving field. For instance, the generation of *higher harmonics* in the frequency domain is described by

$$\boxed{\delta b(n \cdot \omega) = G^{(n)}(\omega, \ldots, \omega) F(\omega) \ldots F(\omega) \,,} \tag{2.64}$$

where $G^{(n)}$ is a non-linear response function, given by a complicated expression involving multiple occurences of the linear-response Green's function G, which is both computationally expensive and physically intransparent. In time domain, however, the same information is captured by identifying equidistant spectral peaks in the Fourier-transform of $p(t)$.

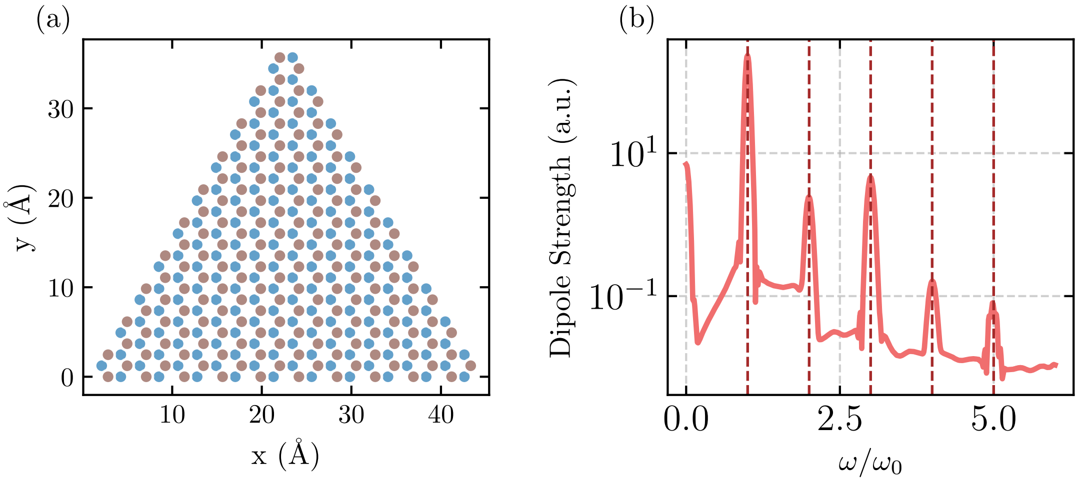

Figure 2.4.: **(a)** Geometry of a graphene nanotriangle with zigzag edges, used as the prototypical structure that sustains a nonlinear optical response. The flake is illuminated by a short x -polarized laser pulse centered at its dominant plasmon frequency of $\omega_p = 0.68\,$eV. **(b)** Corresponding higher-harmonic spectrum obtained from the Fourier transform of the induced dipole moment $p(t)$. Pronounced peaks at integer multiples $n\omega_d$ of the driving frequency $\omega_d = \omega_p$ clearly demonstrate higher-harmonic generation mediated by plasmonic excitations.

In the following subsection, we turn to an example of this nonlinear response by presenting the generation of *higher-harmonics* in triangular graphene nanostructures.

2.6.2. Higher-Harmonic Generation in Graphene Nanotriangles

Graphene nanotriangles have recently attracted attention as efficient platforms for higher-harmonic generation (HHG) [83], often outperforming conventional plasmonic nanostructures based on noble metals such as gold or silver. The enhancement arises from plasmonic excitations, collective modes of the electron gas induced by electron–electron interactions. These triangular nanostructures host well-defined plasmons that strongly mediate nonlinear light–matter interactions and are, therefore, also referred to as plasmon-polaritons [85].

To illustrate this phenomenon, we follow the setup of [83]. A graphene nanotriangle is illuminated by a short laser pulse with its central frequency ω_d chosen equal to the plasmon frequency ω_p. The time-dependent dipole moment $p(t)$ of the graphene nanotriangle is computed under propagation. A Fourier transform yields the frequency-resolved spectrum $p(\omega)$. By comparison with the nonlinear response formalism of Equation (2.64), peaks in $p(\omega)$ at integer multiples $n\omega_d$ of the driving frequency identify the generation of higher harmonics. Figure 2.4 shows both the geometry of the nanotriangle and the corresponding nonlinear spectral response.

There are physical restrictions, placed by fundamental requirements of gauge invariance and, thus, charge conservation on the response behavior of a nanostructure, encoded in the form of *sum rules*. In the next subsection, we cover these in more detail.

2.6.3. Sum Rules

Response functions are subject to important constraints in the form of *sum rules*, which reflect fundamental conservation laws and symmetries [82]. One particularly significant example is the Thomas–Reiche–Kuhn (TRK) sum rule, which appears in several closely related forms [86] [64].

Consider the general operator identity [87]

$$\langle m|[O,[O,H]]|m\rangle = 2\sum_n (E_n - E_m)|o_{nm}|^2\,, \tag{2.65}$$

valid for any Hermitian operator O. This expression can be straightforwardly verified by explicit evaluation.

When O is chosen as the position operator $\boldsymbol{x}$, Equation (2.65) yields the familiar TRK sum rule of atomic physics [86]

$$\langle m|[\boldsymbol{x},[\boldsymbol{x},H]]|m\rangle = -i\,\langle m|[\boldsymbol{x},-i\tfrac{\boldsymbol{p}}{m}]|m\rangle = -\tfrac{1}{m} = 2\sum_n (E_n - E_m)|\boldsymbol{x}_{nm}|^2\,. \tag{2.66}$$

Turning to the current response, the static paramagnetic current-current correlator can be expressed as

$$G_{JJ}(\omega = 0) = \sum_{nm} \frac{J_{mn}J_{nm}}{E_n - E_m}\,, \tag{2.67}$$

where use of the canonical commutation relation Equation (2.29) gives

$$J_{nm} = P_{nm}E_n - P_{nm}E_m\,. \tag{2.68}$$

Combining this with Equation (2.65) and Equation (2.67), one finds

$$G_{JJ}(0) = \sum_{nm} |P_{nm}|^2(E_n - E_m) = \frac{Ne^2}{2m}\,, \tag{2.69}$$

with N denoting the total number of electrons. This is the TRK sum rule as employed in condensed matter response theory.

Its fundamental importance can be clarified by considering that the *total* static current-current response $G^{\text{tot}}_{JJ}(0)$ encodes the induced current in response to a spatially uniform and static external vector potential A_0,

$$j(0) = G^{\text{tot}}_{JJ}(0)A_0\,. \tag{2.70}$$

However, a static and spatially uniform vector potential is physically unobservable, as it constitutes a pure gauge leaving Maxwell's equations invariant. Gauge invariance therefore requires the total response to vanish, which makes the sum rules stated above valid not only for independent particles, but in general. In explicit calculations, this is ensured by cancellation between the diamagnetic current (proportional to A^2) and the paramagnetic response [82].

The most convenient way to enforce gauge invariance in practice is to redefine the total correlator as

$$\boxed{G^{\text{tot}}_{JJ}(\omega) = G_{JJ}(\omega) - G_{JJ}(0)\,,} \tag{2.71}$$

so that the spurious static paramagnetic contribution cancels exactly.

Finally, the most common form of the TRK sum rule is given by the following integral identity [82]

$$\int_0^\infty \omega\,\text{Im}[G_{JJ}(\omega)]\,d\omega = \frac{Ne^2}{m}\,. \tag{2.72}$$

Having established the foundations of the theory of independent particles, we are now in a position to extend the discussion to include the effects of electron-electron interactions.

2.7. Electron–Electron Interactions

In this section we incorporate electron–electron interactions into our framework and clarify how they reshape ground states, excitations, and dynamical response. We begin with a conceptual overview of the two-body nature of the most common form of these interaction terms. After that, we introduce controlled approximations that render the problem tractable. First, we develop a mean-field treatment, which replaces the two-body interaction by self-consistent single-particle potentials. Its capabilities are illustrated on finite Hubbard flakes, where we track the interaction-driven crossover from metallic to insulating behavior and the emergence of spin order. Second, we incorporate correlations beyond mean field via the random-phase approximation (RPA), motivated and derived within the tight-binding linear-response formalism in close analogy to [20].

2.8. Theoretical Description

Up to this point, our discussion has been restricted to non-interacting (independent) electrons. In realistic systems, however, electronic interactions play a decisive role in determining ground-state properties, excitation spectra, and dynamical response. Such interactions can be incorporated at various levels of approximation: by correcting the ground state, by modifying the time-evolution equations, or by altering the frequency-dependent response functions.

The most fundamental and ubiquitous interaction between electrons is the Coulomb repulsion. In first quantization, the electron–electron interaction is represented by a two-body operator acting simultaneously on two electron coordinates, in contrast to the single-particle operators encountered in the independent-particle case. Explicitly, the Coulomb interaction reads [88]

$$V = \frac{1}{2} \sum_{i \neq j} \frac{K}{|\boldsymbol{r}_i - \boldsymbol{r}_j|} , \tag{2.73}$$

where K is a constant reflecting the dielectric background (*e.g.* static screening due to the lattice or surrounding medium).

In the formalism of second quantization, the two-body operator V takes the generic form [68]

$$V = \frac{1}{2} \sum_{ijkl} V_{ijkl} \, c_i^\dagger c_j^\dagger c_k c_l , \tag{2.74}$$

where the coefficients V_{ijkl} are two-particle matrix elements (more precisely, a rank-4 tensor) given by

$$V_{ijkl} = \langle ij|V|kl\rangle \ . \tag{2.75}$$

Equation (2.74) is generic: any two-particle operator admits this structure, independent of the explicit form of the interaction.

In direct analogy to the definition of the one-particle reduced density matrix (1RDM), expectation values of two-particle operators can be expressed in terms of the *two-particle reduced density matrix* (2RDM). For a state $|\psi\rangle$, the expectation value of V is given by

$$\begin{aligned} \langle\psi|V|\psi\rangle &= \sum_{ijkl} \langle\psi|a_i^\dagger a_j^\dagger a_k a_l|\psi\rangle \, V_{ijkl} \\ &\equiv \sum_{ijkl} \gamma_{ijkl}^{(2)} \, V_{ijkl} , \end{aligned} \tag{2.76}$$

where we have introduced the 2RDM,

$$\gamma_{ijkl}^{(2)} = \langle\psi|a_i^\dagger a_j^\dagger a_k a_l|\psi\rangle \ . \tag{2.77}$$

This representation is formally exact. However, the 2RDM contains a vastly larger amount of information than the 1RDM, and its direct computation and storage scale prohibitively with system size. Consequently, the explicit use of Equation (2.74) in interacting many-body calculations is generally impractical.

In the following subsections, we therefore turn to approximate strategies for incorporating electron–electron interactions.

2.8.1. Mean-Field Theory

The full interacting Hamiltonian including both single-particle and two-particle contributions can be written as

$$H = \sum_{ij} t_{ij}\, c_i^\dagger c_j + \frac{1}{2} \sum_{ijkl} V_{ijkl}\, c_i^\dagger c_j^\dagger c_k c_l \,, \tag{2.78}$$

where t_{ij} denotes single-particle hopping or kinetic terms, and V_{ijkl} are two-particle interaction matrix elements as defined in Equation (2.74).

A natural and widely used strategy for approximately treating the interaction is to introduce a non-interacting reference system, thereby replacing the full Hamiltonian by an effective single-particle operator H_mf, capturing the interation between electrons in terms of an effective potential, also called mean field, [89]

$$H_\text{mf} = \sum_{ij} h_{ij}\, c_i^\dagger c_j \,. \tag{2.79}$$

As discussed, the ground state of this Hamiltonian always corresponds to a single Slater determinant. Consequently, the difference between the ground state energy of the effective system, E_mf, and the energy of the interacting system, E, can be expressed as

$$\langle \psi | H_\text{mf} - H | \psi \rangle = E_\text{mf} - E = \sum_{ij} \gamma_{ij} \big(h_{ji} - t_{ji} \big) - \frac{1}{2} \gamma^{(2)}_{ijkl}\, V_{ijkl} \,, \tag{2.80}$$

For a single Slater determinant, Wick's theorem yields the factorization of the 2RDM

$$\gamma^{(2)}_{ijkl} = \gamma_{il}\gamma_{jk} - \gamma_{ik}\gamma_{jl} \,, \tag{2.81}$$

resulting in

$$E_\text{mf} - E = \sum_{ij} \gamma_{ij} \big(h_{ji} - t_{ji} \big) - \frac{1}{2} \big(\gamma_{il}\gamma_{jk} - \gamma_{ik}\gamma_{jl} \big)\, V_{ijkl} \,. \tag{2.82}$$

Thus, the figure of merit in Equation (2.80) depends only on the 1RDM of the ground state of the reference system. Minimization with respect to γ determines the effective Hamiltonian matrix elements [82]

$$\boxed{h_{ij} = t_{ij} + \sum_{kl} V_{ilkj}\, \gamma_{lk} - \sum_{kl} V_{iljk}\, \gamma_{lk} \equiv t_{ij} + C_{ij}[\gamma] + X_{ij}[\gamma] \,.} \tag{2.83}$$

Here, we have identified two distinct contributions:

- $C_{ij}[\gamma]$ — the *direct* or *Coulomb* channel, also called Hartree term, representing the electrostatic interaction between charge distributions.

- $X_{ij}[\gamma]$ — the *exchange* channel, arising from fermionic antisymmetry.

The replacement of operator-valued interaction terms by contractions of the 1RDM illustrates why this procedure is called a *mean-field* approximation: interactions are replaced by their expectation (mean) values with respect to a reference state. A note on terminology is now in order: If the involved quantities t and V are computed by expanding the single-electron Equation (2.2) and the interaction Hamiltonian Equation (2.73), the resulting mean-field theory is an *ab initio* approach, since it operates directly on the fundamental electronic interaction terms. This is referred to as the Hartree-Fock method [90]. This thesis mostly adopts a less rigorous, but computationally cheaper tight-binding approach, whereby the kernels t and V are both treated parametrically, as discussed in the following section.

The mean-field ansatz is flexible: by choosing different reference states ψ, one can extend the framework beyond Slater determinants. For instance, using appropriate trial states enables the treatment of superconductivity mediated by electron–phonon interactions in BCS–theory [91] or electron–photon cavity systems [92].

From a numerical standpoint, the mean-field equations are solved self-consistently *via* the following iterative scheme:

1. Choose an initial guess for the density matrix $\gamma^{(0)}$.
2. Construct the mean-field Hamiltonian $H_{\text{mf}}[\gamma^{(0)}]$ using Equation (2.83).
3. Diagonalize $H_{\text{mf}}[\gamma^{(0)}]$ to obtain a new density matrix $\gamma^{(1)}$.
4. Repeat steps 2 and 3 until convergence, *i.e.* until $\gamma^{(n+1)} \approx \gamma^{(n)}$ within a chosen tolerance.

Mean-field theory is often the simplest framework for detecting instabilities: parametric points where electronic interactions drive the system from one qualitative regime into another. A classic example is onsite Coulomb repulsion, which can induce insulating behavior in systems that would otherwise be metallic. In extended systems, such interaction-driven crossovers are referred to as Mott phase transitions [63]. An illustration of the finite-size analog of this phase transition is detailed in the next section, where we see these interactions to open a gap in the spectrum of a finite cut of a metallic nanoflake described by the Hubbard model.

At the same time, mean-field theory is limited by its reliance on a single Slater determinant and the corresponding factorization of the two-particle reduced density matrix. This approximation can be too restrictive in materials where strong correlations dominate, such as transition-metal oxides and perovskites, which are labeled *strongly correlated* precisely because they lie beyond the reach of mean-field descriptions [93]. Despite these shortcomings, mean-field theory remains an indispensable first step: it provides a tractable and often qualitatively correct starting point for analyzing interacting electronic systems.

In the following subsection, we illustrate its use studying the insulating crossover in nanoflakes described by the Hubbard model.

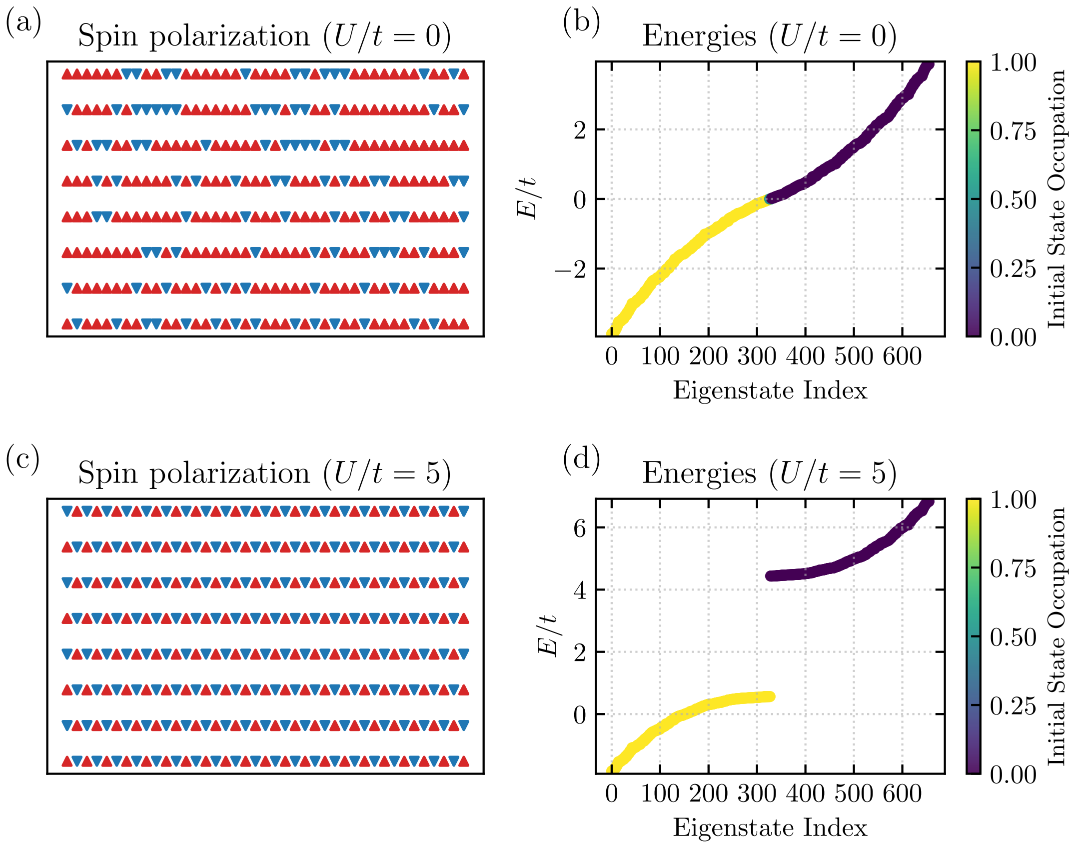

Figure 2.5.: **(a)** Spin polarization of a square-lattice Hubbard flake at $U/t = 0$, showing no local magnetization. **(b)** Spin polarization at $U/t = 5$, exhibiting alternating ferromagnetic order. **(c)** Energy spectrum corresponding to panel (a), with no spectral gap. **(d)** Energy spectrum corresponding to panel (b), displaying an interaction-induced insulating gap.

2.8.2. Insulating Crossover in Hubbard Flakes

A paradigmatic model for interaction-driven phase transitions is the Hubbard Hamiltonian on a square lattice [94],

$$H = t \sum_{\sigma,\langle i,j\rangle} c^{\dagger}_{\sigma,i} c_{\sigma,j} + U \sum_{i} n_{i,\uparrow} n_{i,\downarrow}, , \tag{2.84}$$

where the first term describes nearest-neighbor hopping with amplitude t, and the second introduces an on-site repulsion U between electrons of opposite spin. Without loss of generality, we set $t = 1\,\mathrm{eV}$. Despite its simplicity, this model captures the essential physics of magnetism and interaction-driven insulating behavior.

Local magnetic order can be characterized by the spin polarization at each site,

$$s_i = \langle n_{i,\uparrow} \rangle - \langle n_{i,\downarrow} \rangle \ , \tag{2.85}$$

while the total magnetic moment follows from summing over all sites.

For $U = 0$, the system reduces to a non-interacting tight-binding model. The electronic states are delocalized across the entire flake, and no spin polarization is present, corresponding to metallic behavior. As U is increased, Coulomb repulsion penalizes double occupancy, driving electrons to localize on lattice sites. Within mean-field theory, this localization manifests as a spin-dependent potential that stabilizes alternating spin configurations. The system then acquires a gap in its energy spectrum and becomes an interaction-driven insulator with ferromagnetic ordering [95].

Finite flakes cut from the square lattice display the same crossover as extended systems. Within the mean-field approximation, the Hubbard Hamiltonian can be decoupled according to Equation (2.83), leading to an effective single-particle problem with site- and spin-dependent mean fields,

$$H_{\text{mf}} = t \sum_{\sigma,\langle i,j \rangle} c^{\dagger}_{\sigma,i} c_{\sigma,j} + U \sum_{i} \Big(\langle n_{i,\uparrow} \rangle \, n_{i,\downarrow} + \langle n_{i,\downarrow} \rangle \, n_{i,\uparrow} - \langle n_{i,\uparrow} \rangle \, \langle n_{i,\downarrow} \rangle \Big). \tag{2.86}$$

Figure 2.5 illustrates this crossover for a finite rectangular Hubbard flake. At $U = 0$, no local magnetization is observed and the spectrum is gapless [panels (a,c)]. At $U = 5t$, local spin polarization emerges in an alternating pattern, and a gap opens in the spectrum [panels (b,d)], signaling the transition to an insulating regime.

2.8.3. Time Evolution with Mean-Field Terms

The usefulness of mean-field theory extends beyond the description of ground states: it also provides a tractable framework for time-dependent dynamics. In general, the equation of motion (EOM) for the 1RDM couples to the two-particle 2RDM, which in turn depends on the three-particle reduced density matrix, and so on. This recursive structure is known as the BBGKY hierarchy [65], and it renders the exact description of dynamics in interacting systems intractable.

A key advantage of the mean-field approximation is that it effectively closes this hierarchy. Because the interacting Hamiltonian is replaced by a single-particle operator with self-consistent potentials, one can derive an equation for the 1RDM in complete analogy to the independent-particle case, given by Equation (2.53) [84]

$$-i \, \partial_t \gamma(t) = \big[h(t) + v[\gamma(t)], \, \gamma(t) \big] \,, \tag{2.87}$$

where the interaction-induced potential

$$v[\gamma(t)] = C[\gamma(t)] + X[\gamma(t)] \tag{2.88}$$

collects the Coulomb (C) and exchange (X) contributions introduced in Equation (2.83).

The inclusion of dissipation proceeds exactly as in the independent-particle case, yielding the mean-field master equation,

$$\boxed{-i \, \partial_t \gamma(t) = \big[h(t) + v[\gamma(t)], \, \gamma(t) \big] + \mathcal{D}[\gamma(t)] \,,} \tag{2.89}$$

where $\mathcal{D}$ denotes a dissipator of the type discussed previously in subsection 2.5.3.

In practice, the interaction kernel $v[\gamma]$ is a large-rank tensor, and its explicit evaluation is prohibitively expensive for realistic systems. Throughout this thesis, we therefore adopt a simplified approximation scheme that drastically reduces its complexity. Specifically, we neglect the exchange channel entirely and approximate the Coulomb term by retaining only diagonal-like elements of the form V_{ijji}, denoted [74]

$$C_{ij} \equiv V_{ijji}\,, \tag{2.90}$$

while setting all other components of V_{ijkl} to zero. This approximation transforms the Coulomb contribution into a square matrix acting directly in the single-particle basis, making the time-evolution equations computationally manageable while still retaining the essential physics of direct electron–electron repulsion. Often, it is not desirable to run a mean-field calculation prior to time propagation. As discussed in section 2.2, when working with tight-binding models fitted to *ab initio* data, we may wish the kinetic term in Equation (2.78) to yield the "true" ground state 1RDM γ_0 of the system. Electronic interactions should only be induced once the system is driven out of this state, which can be ensured by performing the replacement

$$v[\gamma] \rightarrow v[\gamma - \gamma_0]\,. \tag{2.91}$$

This is the standard route adopted in this thesis and corresponds to the treatment of "induced potentials" discussed in [84]. Having laid out the time-domain response, we are now in a position to develop the random-phase approximation (RPA), which incorporates interaction effects directly in the frequency domain.

2.8.4. Random Phase Approximation

A standard approach that goes beyond mean-field theory is the *random-phase approximation* (RPA). Originally introduced in the context of the jellium model of an idealized electron gas [63], RPA can be rigorously derived as a summation of bubble diagrams in a many-body perturbation theory. Here, however, we follow the more intuitive linear-response formulation given in Refs. [82] [20]. In the linear-response framework, the induced electronic density at frequency ω can be expressed as in Equation (2.61)

$$\delta n(\boldsymbol{r},\omega) = \int \mathrm{d}\boldsymbol{r}'\, G_{nn}(\boldsymbol{r},\boldsymbol{r}',\omega)\,\phi(\boldsymbol{r}',\omega)\,, \tag{2.92}$$

where G_{nn} is the *proper* density–density correlator and ϕ denotes the *total* potential acting on the electrons. Importantly, this total potential consists of both the externally applied field and the induced internal Hartree contribution. Consequently, G_{nn} is not itself a linear response function in the strict sense and does not necessarily fulfill the requirement of causality [82].

Adopting the tight-binding basis introduced earlier, the spatial integral can be replaced by a discrete sum over lattice sites,

$$\delta \langle n \rangle_i (\omega) = \sum_j \left[G_{nn}(\omega)\right]_{ij} \phi(\boldsymbol{R}_j, \omega) \,, \tag{2.93}$$

with $\boldsymbol{R}_i$ denoting the position of site i.

The total potential is the sum of the external and the internal contributions,

$$\phi(\boldsymbol{R}_i, \omega) = \phi_{\text{ext}}(\boldsymbol{R}_i, \omega) + \sum_j C_{ij}\, \delta n_j(\omega) \,, \tag{2.94}$$

where C_{ij} represents the electrostatic Coulomb interaction matrix, defined in Equation (2.90).

Combining these relations yields

$$\delta n_i(\omega) = \sum_j M_{ij}(\omega)\, \phi_{\text{ext}}(\boldsymbol{R}_j, \omega) \,, \tag{2.95}$$

$$M(\omega) = \left[1 - G_{nn}(\omega) C\right]^{-1} G_{nn}(\omega) \,, \tag{2.96}$$

where $M(\omega)$ is the RPA density response function.

Within the RPA, the proper density–density correlator G_{nn} is approximated by its non-interacting form, *i.e.* the independent-particle expression given earlier in Equation (2.62). Finally, assuming the absence of intra-atomic dipole moments, the induced dipole moment can be computed as $\boldsymbol{p}_i = \delta n_i \boldsymbol{R}_i$ on site i and we obtain for the dipole-dipole correlator, also referred to as *polarizability*

$$\boxed{G_{P_i P_j}(\omega) = \sum_{ab} R_{ia}\, M_{ab}(\omega)\, R_{jb} \,,} \tag{2.97}$$

which encodes the linear optical response of the interacting system within the RPA framework.

The discussion of the RPA completes the review of the theoretical approach taken in this thesis. In the next chapter, we turn to its practical implementation in form of the simulation program `GRANAD`.

3. GRANAD: Tight-Binding Simulations

In this chapter, we detail the software implementation of the theoretical tools laid out in the previous chapter: the simulation program `GRANAD` (GRAphene NANoflakes with ADatoms).

The development of this software was carried out within a broad collaborative framework involving the Institute of Theoretical Solid State Physics at the Karlsruhe Institute of Technology, the Institute of Physics at Nicolaus Copernicus University in Toruń, the Donostia International Physics Center, and the Nanoscale Device Characterization Division at the National Institute of Standards and Technology. Originating from earlier efforts undertaken by Marvin Müller at KIT and Miriam Kosik at UMK, described in [96, 97], the core of `GRANAD` predates the present work and has already served as the foundation for several published studies [P2, 62, 74]. Over the course of this thesis, the codebase has undergone substantial expansion and modernization; most notably through its migration to the JAX [76] ecosystem. These efforts have transformed `GRANAD` into a fully differentiable, high-performance simulation package. Originally conceived as a specialized tool for modeling one- and two-dimensional carbon-based nanosystems, it has since evolved into a versatile and broadly applicable framework for simulating optoelectronic phenomena in nanostructures, while retaining a particular strength in handling systems with hexagonal microscopic lattice symmetry [P4].

As discussed in the introduction, a variety of tight-binding frameworks have been developed to address complementary aspects of quantum and transport simulations. Packages such as `Kwant` [27] and `KITE` [28] provide robust solvers for electronic transport and large sparse systems, often emphasizing steady-state scattering or spectral methods like the kernel polynomial approach. Tools such as `pythtb` [29] and `pybinding` [30] focus on model construction, band-structure analysis, and topological diagnostics in periodic or finite systems, offering efficient interfaces within the Python ecosystem. In contrast, `GRANAD` extends this landscape toward fully differentiable optoelectronic simulations of finite nanostructures. The unique combination of efficient material simulation with the differentiable philosophy distinguishes `GRANAD` as a high-performance platform for exploring light–matter interactions.

The core functionality of `GRANAD` includes intuitive specification of nanostructure geometries and their electronic interactions. It supports simulations in both the time- and frequency domain. The time-domain engine is equivalent to a time-dependent mean-field theory, relying on the 1RDM of the nanostructure, solving the master equation Equation (2.89). It can be flexibly extended with custom specifications for Hermitian, non-Hermitian, and non-linear interactions, enabling tailored investigations of open quantum systems across a wide variety of external potentials (*e.g.*, vibrational), internal electron–electron interactions at the mean-field level, and user-defined dissipation channels. While the default models are tight-binding based, this extensibility also makes it suitable for use in *ab initio* settings.

In the time-domain, `GRANAD` enables computing the dynamical expectation value of arbitrary one-particle operators, such as current, polarization, magnetization, or charge and offers access to the dynamical 1RDM. In the frequency domain, `GRANAD` enables the computation of optoelectronic response functions, both in the independent-particle approach given in Equation (2.62) and the RPA, detailed in Equation (2.97).

On the technical side, the code is built on JAX, which provides differentiability, just-in-time (JIT) compilation, and GPU acceleration, making it well-suited for integration with machine learning workflows. `GRANAD` is accompanied by comprehensive documentation and tutorials, available at `https://granadlauncher.github.io/granad/`, to support new users and developers.

The `GRANAD` simulation software as described here has undergone peer review and has been published in [P4].

3.1. Overview

The core architecture of `GRANAD` is structured around two complementary components: a numerical engine responsible for the actual simulations, and a high-level interface designed for flexibility and the interactive specification of nanostructures down to individual orbitals.

A typical simulation proceeds in two main stages. First, the user defines the nanomaterial at the orbital level. This process prioritizes interactivity and flexibility over raw computational performance. Orbitals can be freely positioned, deleted, or displaced; interactions between them are represented by Hamiltonian, Coulomb, or exchange terms and can be defined as arbitrary functions or imported from external *ab initio* calculations. This allows for the incorporation of realistic physical perturbations such as strain, doping, or point defects. Internally, the nanostructure is represented as a plain Python list, chosen deliberately for its simplicity and familiarity. Importantly, simulations can already be run at any intermediate stage of the construction process, encouraging an exploratory workflow.

A particularly powerful feature of the structural definition stage is the ability to generate larger orbital clusters by "cutting" geometrical shapes from predefined bulk materials, where we shall to infinitely extended materials as bulk, regardless of their dimensionality. This allows rapid prototyping of complex nanoscale devices. While the computational complexity of this operation scales quadratically with the number of orbitals involved, it is confined to the structure-building phase and thus typically not a bottleneck during the simulation runs themselves.

In the second stage, the defined structure is simulated. `GRANAD` supports various forms of analysis, including mean-field ground-state calculations, as well as simulations in either the time or frequency domain. Results such as energy spectra, optical absorption profiles, or eigenstates can be visualized using a suite of built-in plotting tools, which are highly customizable. The computational cost for these simulations scales cubically with the system size, as is typical for matrix-based methods.

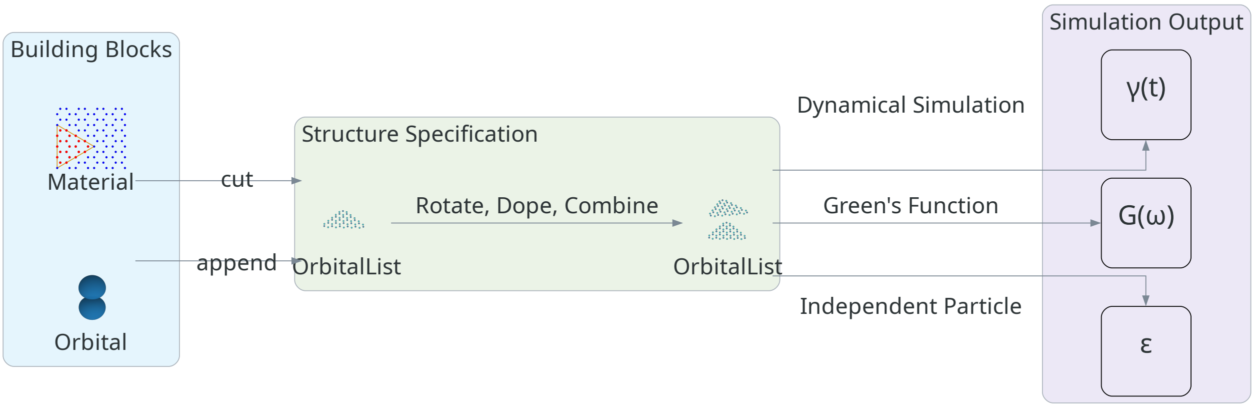

Figure 3.1.: Schematic of the simulation workflow implemented in `GRANAD`, as described in the main text. Starting from basic building blocks, single orbitals or finite flakes cut into polygonal shapes, a nanoflake can be constructed and represented by an `OrbitalList` object. Such objects may be modified geometrically or electronically, or combined into larger systems such as bilayers or clusters. At any stage of this interactive structure definition, different simulation routes can be pursued: dynamical simulations yield the time-dependent density matrix $\gamma(t)$, whereas frequency-domain simulations provide the Green's function $G(\omega)$, highlighting the dual simulation strategy illustrated in Figure 2.1. In addition, static simulations can be performed to access independent-particle quantities such as the energies ϵ. The blue and green box constitute the *high-level* Pythonic layer, while the *low-level* simulation layer, relying on JIT compilation, is represented by the violet box. `GRANAD` promotes an iterative investigation process: After running simulations for a given nanostructure, its specification can be altered and the simulations rerun.

To mirror this two-step workflow, `GRANAD` is organized into two principal layers that follow distinct design philosophies: a high-level interface written entirely in Python carrying out the nanostructure specification process, and a low-level numerical backend built on top of JAX with JIT compilation.

The high-level interface is designed to be intuitive, readable, and adaptable. Users can construct nanostructures incrementally, either by adding individual orbitals manually or by cutting out larger blocks of orbitals from bulk material specifications. `GRANAD` ships with built-in specifications of common two-dimensional materials such as graphene, hexagonal boron nitride (hBN), and molybdenum disulfide (MoS_2). User can also supply custom bulk models, possibly derived from *ab initio* calculations following Wannierization. Interaction terms can be specified between either individual orbitals or types of orbitals, enabling the integration of typical quantum optical model systems, such as two-level emitters. The nanostructure, once assembled, continues to behave like a mutable Python list, albeit enriched with physical attributes such as temperature or doping levels that can be set externally. This design philosophy aligns closely with Python's core principles, often described as Pythonic, emphasizing clarity, modularity, and object-oriented organization consistent with the conventions of the scientific computing community.

In contrast, the low-level numerical backend adopts a functional programming paradigm aligned with the philosophy of JAX. Here, the orbital list is converted on demand into dense numerical arrays representing Hamiltonians, density matrices, interaction tensors, and other operators of physical interest. These matrices are then passed to highly optimized routines that are compiled just-in-time: the first invocation of any such routine incurs a compilation cost, but subsequent calls are executed with high efficiency thanks to JAX's execution model, provided the shape of the arrays remains unchanged. This architecture ensures that once a structure of fixed size is defined, it can be simulated more efficiently when rapid iteration over external parameters like the number of doping electrons is required.

After this broad overview, the following section covers the core capabilities of both layers in detail. As a guide through the following sections, a typical `GRANAD` workflow has been summarized graphically in Figure 3.1. Unless mentioned otherwise, code for a full reproduction of all figures in this thesis is provided in [R1].

In addition to the high-level specification and low-level simulation layer, `GRANAD` offers an extensive suite of visualization functions to plot, *e.g.*, induced charges or electric fields. To focus on the physically relevant numerics, this functionality is not discussed here.

3.2. Nanostructure Specification

In the following subsections, we discuss the structural setup required to simulate nanostructures in `GRANAD`. This process consists of the definition of the geometry of the nanostructure and its microscopic interactions. First, we detail the approach to geometry specification. Then, we cover the definition of the interaction matrix elements, most prominently the IP Hamiltonian and the Coulomb matrix.

3.2.1. Geometry Design

GRANAD enables simulations down to the level of individual orbitals. At the core of its structural interface is a `Orbital` object, a lightweight data container that holds essential attributes. These attributes include its spatial position and an optional user-defined tag represented by a string, as well as internal identifiers pertaining to its chemical characteristics, *e.g.* to differentiate orbitals of different spins. By default, `GRANAD` assumes spinless orbitals, reducing storage and runtime demands, but this setting can be changed. Importantly, this object is behavior-free and designed for transparency and simplicity. Nanostructures can be assembled manually by specifying orbitals individually and combining them into a larger structure.

More realistically, a nanostructure is often created by extracting a finite region from a predefined bulk material, which we term "cutting" in the following. A bulk material in `GRANAD` is described by a dedicated class, which defines the lattice geometry, available

Table 3.1.: Overview of common methods to specify nanomaterials in `GRANAD` for a hypothetical `OrbitalList` object `flake` and a hypothetical material class `material`. The shape used to cut a material takes extra arguments for the lattice termination type (zigzag or armchair) in hexagonal lattices, reflecting `GRANAD`'s original focus on graphene-like materials. Any polygonal shape can be cut, with some shapes predefined. The design of `OrbitalList` mirrors standard list operations.

Operation	**Program**
Definition of an orbital at a position	`orbital = Orbital(position = position)`
Initialization of a model two-level system	`tls = OrbitalList([orbital1, orbital2])`
Definition of an equilateral triangular polygon with base length 10 Å with zigzag termination	`shape = Triangle(10, armchair = False)`
Cutting a nanoflake from a material	`flake = material.cut_flake(shape)`
Combining nanoflakes into a stack	`stack = flake1 + flake2`
Electronic doping	`flake.set_electrons(electron_number)`
Addition of orbitals	`flake.append(orbital)`
Removal of an orbital at a specific list position	`del flake[index]`
Rotation in a coordinate system centered at a point around the x -axis with an angle ϕ	`flake.rotate(point, phi, "x")`
Translation by a vector	`flake.shift_by_vector(vector)`
Lifting spin degeneracy	`flake.set_open_shell()`

orbital species, and their positions within the periodically arranged unit cell. In `GRANAD`, materials are described using a concise domain-specific language (DSL) that is embedded within Python. This DSL provides a structured syntax for defining the geometry and interactions of the bulk system and is specified in appendix A.

The method for cutting finite flakes from bulk materials depends on the lattice dimensionality. In two dimensions, the process is particularly flexible, reflecting `GRANAD`'s original focus on the 2D material graphene: arbitrary polygons can be used to define the region of interest. `GRANAD` supplies built-in constructor functions to ease the creation of commonly used polygons, including equilateral triangles, rectangles, and general regular polygons, allowing the approximation of circles. A hexagonal lattice like graphene allows for two different edge types characterizing the resulting flakes, either armchair or zigzag. The latter is chosen by default in `GRANAD`, but can be changed straightforwardly by supplying an additional argument to the default shape constructors.

This cutting operation returns an `OrbitalList`, which behaves similarly to a Python list but is extended with domain-specific features. These include plotting utilities, annotations (*e.g.*, orbital indices), and support for common list operations such as insertion and deletion, enabling the modelling of defects and dopant atoms. Beyond geometry, users can set global physical parameters for the structure, such as its electron count or temper-

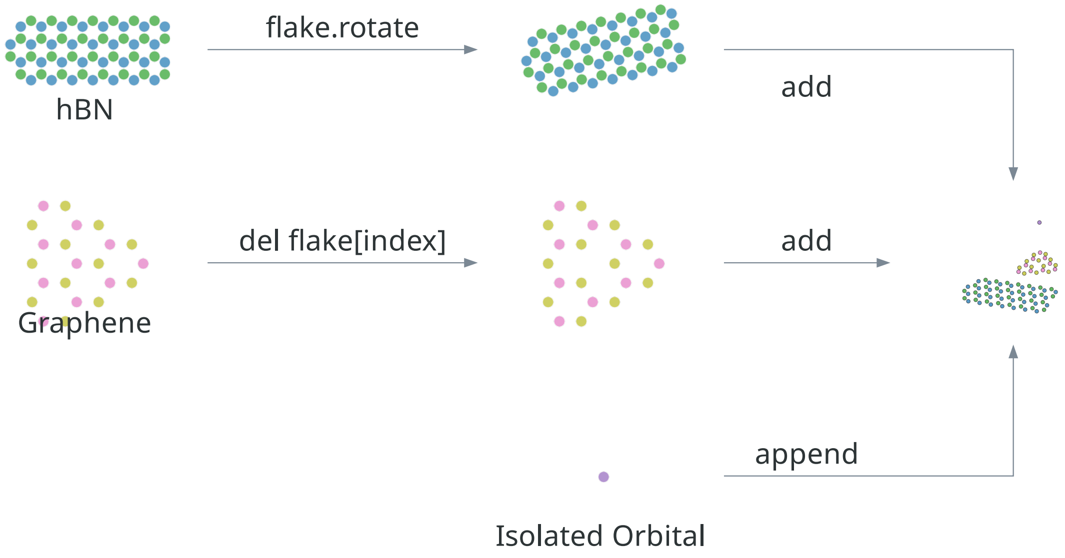

Figure 3.2.: Illustration of the geometry specification process of a heterostructure consisting of a microscopic rectangular layer of hBN, a triangular graphene nanoflake, and an isolated orbital, useful for modelling an optically active dopant, which might represent a gold adatom in realistic applications. The hBN layer is rotated, while the center atom in the graphene triangle is deleted, illustrating some of the versatile functions in Table 3.1.

ature. An overview of the most common operations is given in Table 3.1 and a graphical example showcasing their application is provided in Figure 3.2.

3.2.2. Defining Interactions

`GRANAD` models electronic interactions in terms of tight-binding matrix elements. As detailed in subsection 2.8.3, the prime quantities of interest are the IP Hamiltonian in Equation (2.4) and the Coulomb matrix, defined in Equation (2.90). These interactions can be specified by the user for each `OrbitalList` by coupling either individual orbitals or groups of orbitals in the list. To this end, orbitals can be grouped and identified based on a variety of different internal flags: All chemically identical orbitals in a bulk cut (*e.g.*, all p_z orbitals in a single layer of graphene) share a common and unique `group_id`, while they can be differentiated among each other by an internal `layer_index`. Additionally, orbitals can be identified by their optional properties of spin, orbital kind (*e.g.*, p_z), atom type, and a user-defined tag.

There are two ways to specify couplings: The user can couple groups of orbitals by a function taking one or arguments two that depends either on the relative distance vector between two orbitals or on the absolute position of the two orbitals. Alternatively, the user can couple individual orbitals by directly specifying the matrix element, which is useful

Table 3.2.: Examples of common interaction matrix defitions for a hypothetical `OrbitalList` object `flake` representing a bilayer structure, detailed in the main text.

Definition	**`Program`**
IP Hamiltonian element connecting two isolated orbitals	`flake.set_hamiltonian_element(a, b, value)`
IP Hamiltonian elements connecting an isolated to all orbitals of the upper layer	`flake.set_hamiltonian_groups(a, upper_layer, function)`
Coulomb interaction matrix elements connecting all elements referenced by tags identifying p_z and s orbitals	`flake.set_coulomb_groups("pz", "s", function)`

in the modelling of hybrid quantum-optical and solid state system where individual two-level systems are coupled to one or only a few orbitals in the bulk. The `OrbitalList` datatype internally keeps track of these couplings and implements methods to update these couplings once list operations are performed, *e.g.*, it merges the couplings upon addition of two orbital lists. Examples of common coupling operations are given in Table 3.2.

This table shows how to set the coupling for a hypothetical system consisting of two layers, each hosting a collection of orbitals, referenced by `lower_layer` and `upper_layer`, respectively. The layers are assumed to be instances of `OrbitalList`, resulting from a cutting operation out of a bulk material. Additionally, the structure is assumed to host two additional orbitals named `a, b`, possibly in an optically active two-level system adsorbed onto the upper layer. The variable `value` is assumed to be numeric, *i.e.* an integer, float, or complex number. The function `coupling` is assumed to depend on the inter-orbital displacement vector only and returns another value of numeric type. Internally, `GRANAD` ensures that the resulting interaction matrices are Hermitian to avoid the need for the specification of redundant combinations. By default, the matrices are filled with double-precision complex numbers. The examples make use of `GRANAD`'s internal mechanism of tracking orbitals either by direct reference or a user-defined tag.

The built-in material classes shipping with `GRANAD` provide parametric specifications of the Coulomb and Hamiltonian matrices from literature, which are applied to the resulting `OrbitalList` objects after cutting and can be altered in the material DSL. An overview of available materials and their parameterization sources is given in appendix C.

Having covered the structural definition workflow, corresponding to the two leftmost boxes in Figure 3.1, we now turn to `GRANAD`'s numerical engine, represented by the rightmost box in Figure 3.1.

3.3. Nanostructure Simulation

In the following subsections, we discuss the numerical simulation capabilities of `GRANAD` once a nanostructure is specified. For the sake of readability, a separate section is dedicated to each of the three independent capabilities provided by `GRANAD`: extraction of static IP quantities such as energy spectra, time-domain simulations to unlock the 1RDM as well as expectation values, and frequency-domain simulations based on the Green's function. We remark that this entire process is iterative. A numerical simulation run can be followed up by an additional round of structure manipulation.

3.3.1. Independent-Particle Quantities

Once the structure is defined as detailed in the previous sections, independent-particle quantities can be extracted. This is the simplest simulation in `GRANAD`. IP quantities are provided by attributes of the `OrbitalList` object and are recomputed on demand if physical aspects of the structure have been changed, such as its electron count or orbital composition. In addition, these quantities can be corrected by running self-consistency procedures, based on the mean field approach discussed in subsection 2.8.1 and a charge self consistency procedure devised and detailed in [62]. These procedures result in a new set of IP energies, eigenvectors, and a self-consistent Hamiltonian. An overview of the most important IP quantities is given in Table 3.3.

Table 3.3.: Examples of IP quantities exposed by a hypothetical `OrbitalList` object `flake` consisting of N orbitals.

Quantity	**`Access`**
Hamiltonian	`flake.hamiltonian`
Energies	`flake.energies`
Eigenstates, stored as $N \times N$ array	`flake.eigenvectors`
Coulomb matrix	`flake.coulomb`
Ground state 1RDM	`flake.stationary_density_matrix`
Polarization Operator, stored as $3 \times N \times N$ array	`flake.dipole_operator`
Quadrupole Operator, stored as $3 \times 3 \times N \times N$ array	`flake.quadrupole_operator`
(Paramagnetic) Current Operator, stored as $3 \times N \times N$ array	`flake.velocity_operator`

Note that, as discussed in the theoretical part, the quantities exposed by `GRANAD` are actually the matrix kernels of the associated operators. As such, there exist two common bases in which to represent these matrices: the basis in which the generally non-diagonal IP Hamiltonian is expressed is referred to as the *site basis*, while the eigenbasis of the IP Hamiltonian is called the *energy basis*. `GRANAD` expresses any matrix kernel in site basis by default and enables access to the corresponding energy-basis kernel *via* a call to a dedicated transformation function or simply appending an `_e` to the attribute name. For example, the dipole transition rates for a hypothetical `OrbitalList` object can be accessed as `flake.dipole_operator_e`.

3.3.2. Time-Domain Simulations

Time-domain simulations of the master equation, given by Equation (2.89) are the core capability of `GRANAD`'s numerical engine, which can be operated in different modes.

Table 3.4.: External illuminations offered by `GRANAD`. Note that the design of `GRANAD` reflects the linearity of single-particle interaction terms, enabling the simultaneous illumination of the nanostructure with multiple external fields. This makes it possble, *e.g.*, to consider multiple dipolar sources of potentially detuned frequencies at once.

Illumination	**`Description`**
Plane Wave	`A plane wave with adjustable frequency`
Pulsed Plane Wave	`A Gaussian-pulse modulated plane wave with adjustable pulse parameters`
Dipole Illumination	`A dipolar illumination with adjustable position, orientation and frequency`

The most common scenario and `GRANAD`'s original purpose is the simulation of the response of the nanomaterial to an external time-dependent illumination. Electronic interactions are included *via* the nonlinear potential parameterized by the Coulomb matrix Equation (2.90), while dissipative dynamics encoded in a phenomenological term Equation (2.57) lead to a broadening of the resulting resonances.

To this end, `GRANAD` offers a variety of external electromagnetic illuminations, each suitable for different simulation settings. For instance, an electromagnetic field parameterized by a narrow Gaussian pulse is suitable for the computation of linear response spectra. The computation of quantities characterizing quasiparticle excitations occurring at well-defined frequencies, such as the Energy-Based Plasmonicity index [98], require uniform, undamped plane wave illumination. Finally, nanooptical quantities useful for the characterization of systems at the intersection of quantum optics and solid states such as the local density of optical states (LDOS) require dipolar illumination. An overview of illuminations offered by `GRANAD` is given in Table 3.4.

To track the time-dependent dynamics, the `OrbitalList` class offers a single method `master_equation` that solves the dynamics given by Equation (2.89) in a user-defined time interval and allows to sample the 1RDM on a temporal grid. As already explained, the 1RDM contains all information needed to compute single particle expectation vaues, while many-particle expectation values factorize according to equations like Equation (2.81).

Beyond this default mode of operation, `GRANAD` offers a way to customize the internal Hermitian dynamics by scaling the electronic interaction matrix by a scalar factor, which is often required in investigations of plasmonicity. The non-Hermitian part of the evolution equation can be customized by changing the relaxation time or switching from the phenomenological description to a Lindblad-based one by supplying a matrix containing the energy transfer rates r_k in Equation (2.58).

Furthermore, the evolution equation may be augmented by custom terms or even completely overridden by accessing the internal representation of the equation offered by

Table 3.5.: Simulation modes offered by `GRANAD`. Each mode defines a different level of user control over the Hermitian and non-Hermitian parts of the master equation dynamics.

Simulation Mode	**Description / Typical Use**
Default	Standard electromagnetic simulations of nanomaterials under external fields with phenomenological dissipation.
Customized	Controlled modification of the master equation, enabling rescaling of the Coulomb interaction matrix and replacement of the default phenomenological dissipator with a Lindblad-based description.
Free	Provides full access to the internal representation of the evolution equation, enabling both performance optimizations and tailored simulations beyond the standard electromagnetic ones.

the `OrbitalList` class. This representation captures the functions required to compute the right-hand side of the master equation and includes the array representations of the physical quantities required to run the simulation (such as the Coulomb matrix or the dipole operator). The representation can be modified in a transparent way detailed extensively in the online documentation. This mode of operation allows the simulation of additional potential terms representing electromagnetic couplings beyond the ones provided by default, electron-phonon interactions, or nonlinear electron-electron interactions beyond the direct channel term approximated by the Coulomb matrix.

Additionally, one may use this mode to further optimize the simulation performance, *e.g.*, by discarding redundant matrices otherwise captured in the internal representation. For instance, as detailed in Table 3.3, `GRANAD` represents the dipole operator Equation (2.26) of an N -orbital system as a $3 \times N \times N$ array to include possible inter-orbital dipolar transitions, as discussed in section 2.3. In the absence of inter-orbital dipole transitions, storage demand can be reduced to scale with $3N$ by discarding the off-diagonal elements of the dipole operator array representation.

An overview of the different simulation capabilities, such as electromagnetic simulations, dissipator customization and the specification of custom interaction terms, is given in Table 3.5.

`GRANAD` operates on double-precision complex numbers by default. Sampling the 1RDM of a system consisting of thousand active orbitals over a thousand time steps would thus incur a memory cost of 16 GB, which pushes the limits of most consumer-grade hardware. Additionally, access to the full 1RDM is rarely required for practical computations. Typically, one is interested in the evolution of physically relevant quantities with reduced storage demands.

To accomodate this requirement, `GRANAD` offers functionality to extract only these quantities of interest from the time evolution. Additional arguments to `master_equation` allow to extract the expectation values of an ensemble of single-particle operators as well as changes in the occupation of the IP energy landscape and the dynamics of orbital populations, given by the diagonal elements of the 1RDM. Further customization is possible by supplying an arbitrary function of the density matrix.

The result of the time evolution is stored in a separate `TDResult` object, which also contains quantities necessary to resume or reproduce the simulation and conduct a transform to Fourier space for comparison with the frequency-dependent approach, which we detail next.

3.4. Frequency-Domain Simulations

In the frequency-domain, `GRANAD` computes the IP Green's function according to Equation (2.62) for two arbitrary single-particle operators. The polarizability can be computed in the RPA according to Equation (2.97), which allows the scaling of the Coulomb interaction matrix by a scalar factor, akin to the time-domain simulations, enabling a comparison of the two approaches. Additionally, the site-resolved density-density correlator $[G_{nn}]_{ij}(\omega)$ can be computed. The numerical scheme to speed up the computation of the latter from the naive $\mathcal{O}(N^4)$ scaling to a more favourable cubic one is the same as detailed in the original paper [20], adapted to JAX's functional style, aimed at compatibility with JIT compilation. As a result, an additional considerable improvement in performance of these computations can be achieved by running the associated functions on a GPU.

Table 3.6.: Examples of frequency-domain simulation functions exposed by a hypothetical `OrbitalList` object `flake` of N orbitals

Quantity	**`Access`**
Scalar Correlator between two operators in energy space according to Equation (2.62)	`flake.get_ip_green_function`
Scalar RPA polarizability according to Equation (2.97)	`flake.get_polarizability_rpa`
Site-resolved density-density correlator $[G_{nn}]_{ij}(\omega)$ in Equation (2.97) as an $N \times N$ - matrix	`flake.get_susceptibility_rpa`

Any frequency-domain simulation can be performed on a frequency grid represented by a JAX array for increased efficiency.

The corresponding methods are members of the `OrbitalList` class, which facilitates all simulations and is the only interface to the numerical simulation routines. They are listed in Table 3.6.

3.5. Technical Aspects

In the following, we detail the most important technical considerations entering the design of `GRANAD`. We first cover the aspect that most dominantly sets it apart from other highly capable and optimized tight-binding simulation software such as `Kwant` [27], `KITE` [28], `pythtb` [29] and `pybinding` [30]: its reliance of the JAX library providing not only highly optimized JIT compilation, but also automatic differentiation. We dedicate a separate subsection to illustrate the basic concept of automatic differentiation and its application to a real physical problem, demonstrating the utility of this as of now relatively underexploited technique in the simulation of condensed matter systems. After that, we cover some of the tests that `GRANAD` underwent to ensure the soundness of the implementation, its technical maintenance, and sketch some future developments that have already found their way into the developmental version on GitHub.

3.5.1. Differentiable Programming and Automatic Differentiation

A key feature underlying `GRANAD`'s more advanced capabilities is its integration with differentiable programming, a paradigm central to the JAX library upon which the backend of `GRANAD` is built. In broad terms, differentiable programming refers to the idea of constructing computational routines as compositions of functions whose derivatives are known. By applying the chain rule, the derivative of a complex program can then be automatically computed. This process is known as *automatic differentiation* (AD).

To illustrate its utility in a physical context, consider the static polarizability tensor $G_{P_iP_j}(\omega = 0)$. We can of course compute it using frequency-domain linear response theory at $\omega = 0$ given by Equation (2.62). Alternatively, the static polarizability can be expressed as the Hessian of the ground-state energy E with respect to an external electric field $\boldsymbol{E}$ [99]

$$G_{P_iP_j}(\omega = 0) = \frac{\partial^2 E}{\partial E_i \partial E_j}\,. \tag{3.1}$$

For an independent-particle system, the ground-state energy as a function of electric field can be expressed *via* a chain of computational steps:

$$H(\boldsymbol{E}) = H_0 - \boldsymbol{E} \cdot \boldsymbol{P}\,, \tag{3.2}$$

$$\boldsymbol{\epsilon}(H) = \text{diagonalize}(H)\,, \tag{3.3}$$

$$E(\boldsymbol{\epsilon}) = \sum_{i<E_f} \epsilon_i\,, \tag{3.4}$$

where H_0 is the field-free Hamiltonian, $\boldsymbol{P}$ is the dipole operator, and $\boldsymbol{\epsilon}$ is the vector of single-particle energy levels, sorted in ascending order. The complete energy function can thus be seen as a composition:

$$E = E(\boldsymbol{\epsilon}(H(\boldsymbol{E})))\,. \tag{3.5}$$

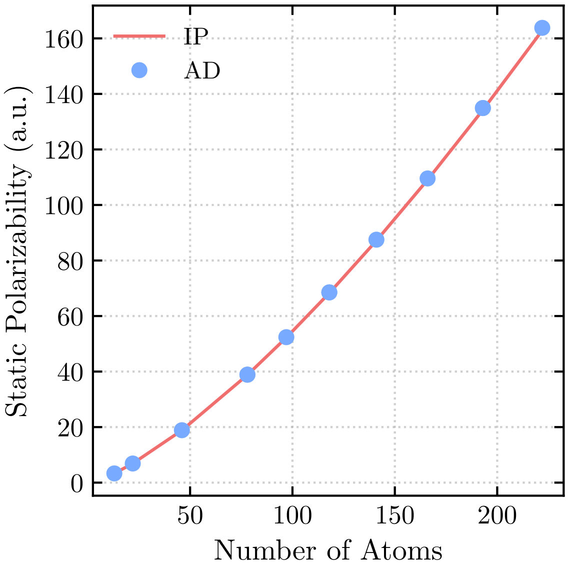

Figure 3.3.: Comparison of the xx -component of static polarizability (real part) computed using automatic differentiation (AD) and Lehmann expansion for triangular graphene flakes of varying size.

Each function in this composition (*e.g.* matrix subtraction, diagonalization and summation) consists of elementary operations such as matrix multiplication, eigenvalue decomposition (assuming non-defective matrices and the absence of degeneracies), or scalar addition. As long as these operations are at least twice differentiable, their derivatives can be composed using the chain rule to yield higher-order derivatives of the entire computational graph.

This is where JAX becomes essential. It provides derivative rules for a wide range of numerical operations and allows these to be composed arbitrarily, enabling physicists to compute gradients, Hessians, and even higher-order derivatives of physical observables without having to implement these manually.

Figure 3.3 shows a concrete example of this approach. The xx -component of the static polarizability for triangular graphene flakes of varying size is computed using two independent methods: first *via* automatic differentiation as described above, and second *via* the Lehmann representation of the linear response function. The results show excellent agreement.

The computational cost of automatic differentiation depends on both the mathematical structure of the problem and the specific AD mode used. To illustrate, consider computing the partial derivative $\partial_{E_i} E$ of the ground-state energy with respect to a single electric field component. Applying the chain rule yields:

$$\frac{\partial E}{\partial E_i} = \frac{\partial E}{\partial \epsilon} \cdot \frac{\partial \epsilon}{\partial H} \cdot \frac{\partial H}{\partial E_i} \,. \tag{3.6}$$

This expression can be evaluated in two distinct ways, known as *forward-mode* and *reverse-*

mode differentiation.

In *forward-mode*, the chain rule is evaluated by computing the terms in the expression given by Equation (3.6) from right to left. One starts by substituting a numerical value for E_i to obtain the perturbed Hamiltonian H, then computes its derivative, followed by the derivative of the eigenvalue function, and so on. This approach is efficient when the number of input parameters (*i.e.*, components of $\boldsymbol{E}$) is small but must be repeated for each component, leading to increased computational cost in higher-dimensional parameter spaces.

In contrast, *reverse-mode* differentiation evaluates the terms in the expression given by Equation (3.6) from left to right. It computes and stores intermediate quantities such as H, ϵ, and their derivatives during a forward pass, and then reuses this information during the backward pass to compute all required gradients. With that, all partial derivatives can be obtained in a single pass with increased memory usage due to the need to retain intermediate states.

Although `GRANAD` is primarily designed for finite systems, preliminary work has been done over the course of this thesis to extend its functionality towards the construction of bulk Hamiltonians and the corresponding band structures. A concrete example has already been provided in subsection 2.2.2, where the AD feature provided by `GRANAD` is used to construct a tight-binding Hamiltonian for graphene from *ab initio* data obtained with the `Quantum ESPRESSO` program [67]. This example highlights how differentiable programming not only facilitates the calculation of physical response functions but also enables efficient parameter inference. The underlying feature of `GRANAD` as a simulation utility for infinite systems is still considered experimental and will be briefly covered in the following subsection.

One of the more forward-looking and exciting capabilities unlocked by automatic differentiation is the seamless integration between solid-state physics and modern machine learning, particularly deep learning. In this context, differentiable programming provides a unified interface: parameters for physical models and neural networks can be combined and jointly optimized within the same computational graph. While preliminary applications of `GRANAD` in this context have already been explored, this avenue is considered experimental and beyond the scope of this thesis.

3.5.2. Testing, Performance and Maintenance

In this subsection, we briefly outline the testing procedures and performance characteristics of `GRANAD`, focusing on internal consistency checks, comparisons to experimental data, and large-scale simulation benchmarks. We also briefly comment on features to be integrated into the productively released code, which are partially already available *via* `GRANAD`'s development version.

As a first validation step, we verify the agreement between simulations carried out in the frequency- and time-domain. In particular, the absorption spectrum of a small triangular hBN nanoflake containing 46 atoms is computed using both the random phase

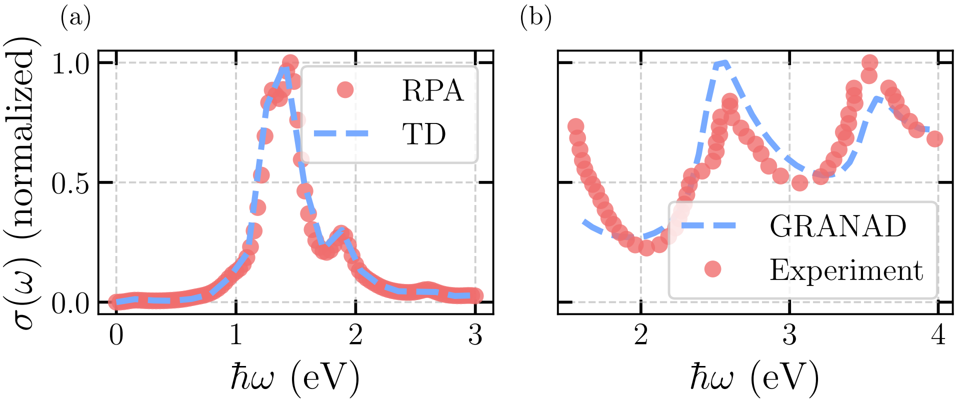

Figure 3.4.: **(a)** Absorption spectrum of a triangular armchair hBN nanoflake containing 46 atoms computed *via* time-domain propagation (blue dashed line) with a duration of $40\,\hbar/\mathrm{eV}$ and frequency-domain RPA (red dots). Excellent agreement confirms internal consistency. **(b)** Absorption spectrum of a graphene nanoribbon (blue dashed line) compared to experimental data (red dots), taken from [100]. The nanoribbon under consideration was 9 atoms wide, armchair-edged with a length of 180 nm, yielding 1090 atoms in the `GRANAD` time-domain simulation with a duration of $100\,\hbar/\mathrm{eV}$. The single graphene nearest-neighbor hopping parameter was -2.2 eV. Non-Hermitian time propagation was conducted with a phenomenological dissipation rate of $r = 0.1\,\mathrm{eV}$. No further adjustments to the default parameters were performed.

approximation (RPA) and real-time propagation *via* the master equation formalism using default parameters in each case. The results, shown in Figure 3.4 (a), demonstrate excellent agreement between the two methods, providing strong evidence for the internal consistency of `GRANAD`'s simulation backend.

We also validate the physical realism of `GRANAD`'s results by comparing them to experimental data. Figure 3.4 (b) displays the optical absorption spectra of a graphene nanoribbon (geometrical details specified in the figure caption), simulated using a tight-binding model with a hopping parameter -2.2 eV. Despite the absence of automatic parameter fitting or gradient-based optimization in this case, the simulated response reproduces the two high-frequency peaks featured in the experimental spectra, taken from [100], indicating the model's descriptive power even in its simplest form.

Lastly, we examine the performance of `GRANAD` on large-scale systems. Figure 3.5 (a) shows the wall-clock time for time-domain simulations as a function of system size for graphene nanoflakes composed of 270 up to 13266 atoms, considering a single p_z orbital per atom. These benchmarks were performed on the Hyperion and Atlas high-performance computing clusters using the unoptimized default mode of `GRANAD`. Despite this, sizable systems remain tractable due to JAX-based JIT compilation and the use of efficient linear algebra backends. In Figure 3.5 (b), we display the runtime advantage gained by executing the simulation for the same setup for system sizes of up to 1000 atoms.

Performance is strongly dependent on the number and type of orbitals. For systems with

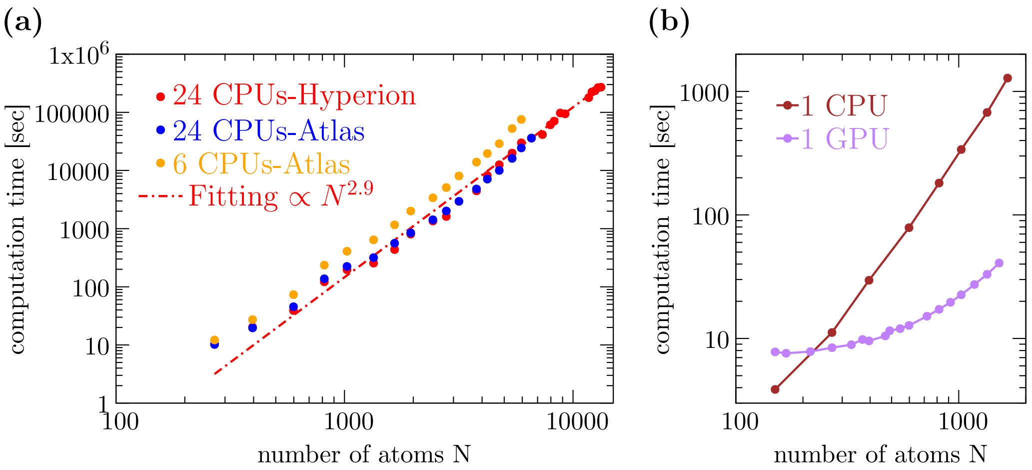

Figure 3.5.: **(a)** Scaling of simulation runtime with system size for triangular armchair-edged graphene flakes, where a single p_z orbital is considered per atom. Simulations were run on the HPC clusters Hyperion and Atlas using an unoptimized build of `GRANAD` with a simulation time of $40\,\hbar/\mathrm{eV}$. The fit shows the expected approximate cubic runtime scaling for both computing clusters. Both x- and y- axes are logarithmic. **(b)** The same setup is simulated for up to 1000 atoms on a single GPU vs CPU to illustrate the performance gained on GPU. Both x- and y- axes are logarithmic. Reproduced from: D. Dams, M. Kosik, M. M. Müller, A. Ghosh, A. Babaze, J. Szczuczko, G. W. Bryant, A. Ayuela, C. Rockstuhl, M. Pelc K. Słowik, GRANAD — Simulating GRAphene nanoflakes with ADatoms, Computer Physics Communications 317 (2025) 109818. DOI: 10.1016/j.cpc.2025.109818. Licensed under CC BY.

multiple orbital species, performance degrades more rapidly due to the increase in the number of cubically scaling operations. Examples of these systems include transition metal dichalcogenides (TMDCs) such as MoS_2, which is included as a built-in material in `GRANAD`. However, as already mentioned, `GRANAD` offers a dedicated simulation mode to mitigate this by tailoring the simulation setup to aggressively optimize for performance by potentially discarding redundant matrix elements as detailed in the previous section and displayed in Table 3.6.

`GRANAD` is hosted on GitHub with a documentation built from runnable code examples in a development version (hosted on the dev branch) and stable version (hosted on the main branch). This thesis focusses mostly on the published stable version. New features in the experimental stage to be integrated into the stable version include the use of non-orthonormalized basis orbitals and the construction of tight-binding Hamiltonians from Slater-Koster parameterizations of the DFTB+ project [25]. Various other features are in a preliminary stage, hosted on the more experimental `granad-scripts` repository, which also hosts the reproduction code for this thesis [R1], which include (semi-)infinite structures and integration with machine learning and sparse-matrix workflows, in particular the prediction of Chebyshev moments from a machine learning setup.

Overall, `GRANAD` combines physical accuracy with a flexible programming interface, offering a platform that is both user-accessible and computationally efficient, while still leaving room for performance tuning and model-specific optimization.

4. Selected Applications

This chapter demonstrates the application of `GRANAD` to a selection of physical problems to illustrate the core capabilities outlined conceptually in the previous chapter.

The first section serves a pedagogical purpose and demonstrates some standard calculations covering ground state and linear response.

The second section presents original results, published in [P3], in higher detail: the application of `GRANAD` to explore the advantageous optical selectivity properties of Haldane graphene, enabled by its topological properties.

4.1. Ground State and Linear Response of Microscopic Systems

In this section, we exemplify `GRANAD`'s application to typical problems encountered in the atomistic study of nanoflakes: First, we investigate the magnetic ground state properties of correlated graphene nanoflakes, emphasizing the impact of geometrical details on the resulting net magnetic moment. We then utilize `GRANAD`'s time domain simulation backend to verify charge conservation in the linear response of a small hBN nanoflake. Finally, we leave the purely electromagnetic sector by simulating the vibronic dipolar response of a graphene nanoflake.

4.1.1. Magnetic Properties of Graphene Nanoflakes

We begin by demonstrating the capabilities of `GRANAD` by studying the magnetic properties of the self-consistently calculated electronic ground state of graphene nanoflakes, obtained from mean field calculations. Graphene nanoflakes with spinful electrons can exhibit intriguing magnetic behavior that directly reflects their geometric and sublattice structure [89]. As discussed in the theoretical section, the Hubbard model serves as a minimal framework to faithfully represent such effects. In this subsection, we will focus on the local and net magnetic moments exhibited by graphene nanoflakes, described by a nearest-neighbor tight-binding model, augmented by the onsite Hubbard term, as discussed in subsection 2.8.1. Our model and the results closely align with those reported in the seminal work on the subject [101] with a nearest-neighbor hopping rate of $t = 2.55$ eV and an onsite Hubbard term with a strength of $U = 4$ eV.

According to Lieb's theorem [102], the total spin S of the ground state in a bipartite lattice is given by

$$S = \frac{1}{2}|N_A - N_B|\,, \tag{4.1}$$

where N_A and N_B are the number of sites assigned to the respective sublattice. Since the total spin is related to the net magnetization by a constant, any sublattice imbalance in a charge-neutral system leads to spontaneous magnetization, and we refer to S and

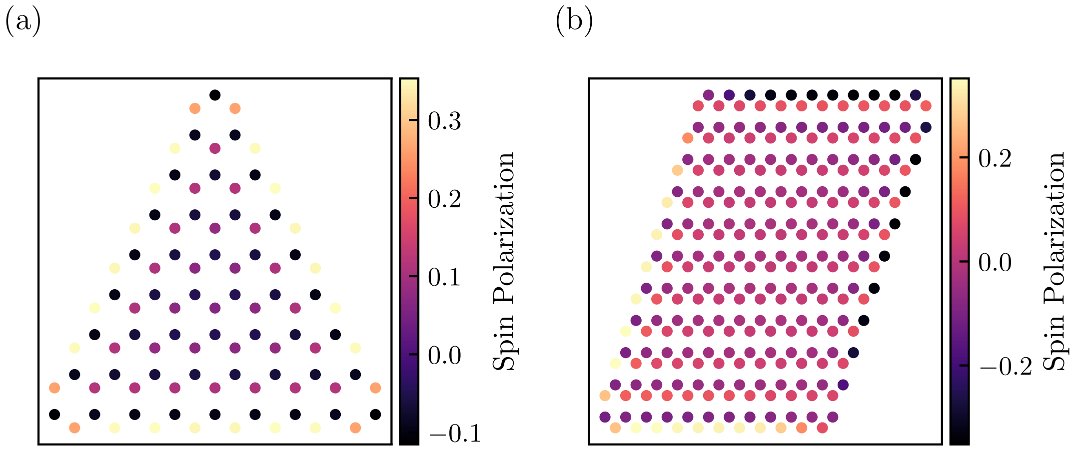

Figure 4.1.: Site-resolved spin polarization for graphene nanoflakes described by a Hubbard-like model. **(a)** Local magnetic moment distribution in a triangular graphene nanoflake hosting 194 atoms. This geometry is characterized by a sublattice imbalance, hosting an excess of 7 sites of the "A" type over the "B" type. According to Lieb's theorem, the resulting net spin amounts to $S = 3.5$, which we confirmed numerically. **(b)** Local magnetic moment distribution in a rhomboid graphene nanoflake hosting 594 atoms. Consistent with Lieb's theorem, we observe the absence of a net magnetic moment because of a balance of sublattices.

its local counterpart as global and local magnetic moments, respectively. To explore this phenomenon in the context of finite graphene systems, we consider two representative nanoflake geometries: a triangular flake with zigzag edges (sublattice-imbalanced), and a rhomboid flake (sublattice-balanced). Both systems are treated within the self-consistent mean-field approximation of the Hubbard model and the results are displayed in Figure 4.1. We compute the site-resolved spin polarization (magnetic moment), given by the expected difference between up and down electrons in the ground state, also referred to as local magnetic moment distribution in zigzag-terminated graphene nanoislands. The ground state is determined by a mean-field calculation according to the discussion in subsection 2.8.1.

Consistent with Lieb's theorem, we find that the rhomboid flake exhibits no net magnetization, while the triangular flake develops a finite magnetic moment due to its sublattice asymmetry. The magnetization is localized at the flake's edges and exhibits ferromagnetic alignment within sublattices and antiferromagnetic coupling between them. These results are consistent with previous findings [89]. The spatial magnetization profiles for both systems are displayed in Figure 4.1.

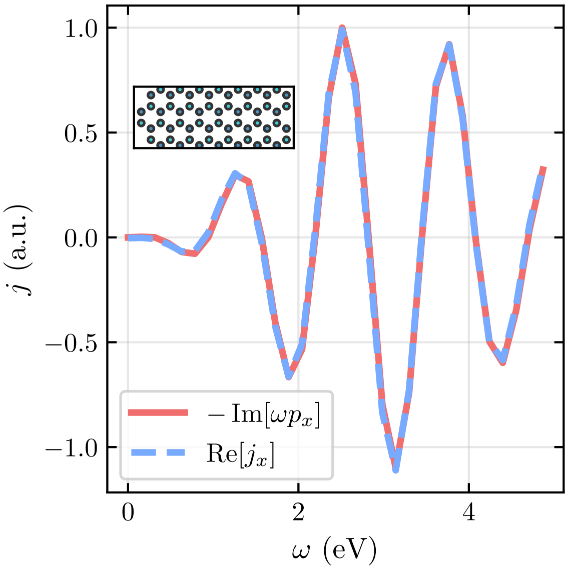

Figure 4.2.: Induced current (details of the pulsed illumination in the main text) in a rectangular hexagonal hBN flake hosting 62 atoms, depicted artistically in the inset with light blue representing Boron, dark blue representing Nitrogen atoms. The current is computed in two ways to explore the validity of the continuity equation. The total dipole moment multiplied by $-i\omega$ and total current are shown to coincide after Fourier transform of a time-domain simulation. Non-Hermitian time propagation was conducted with a phenomenological dissipation rate of $r = 0.1$ eV. No further adjustments to the default parameters were performed.

4.1.2. Charge Conservation in hBN Nanoflakes

We now explore the validity of the continuity equation in a finite hBN flake. This equation implies charge conservation and thus relates intricately to the TRK sum rule discussed in subsection 2.6.3. Starting from the classical continuity equation for the local time-dependent charge density $\rho_{\text{loc}}(\boldsymbol{r}, t)$, current density $\boldsymbol{j}_{\text{loc}}(\boldsymbol{r}, t)$, and dipole moment density $\boldsymbol{p}_{\text{loc}}(\boldsymbol{r}, t)$, we have

$$\frac{\partial \rho_{\text{loc}}(\boldsymbol{r}, t)}{\partial t} = -\nabla \cdot \boldsymbol{j}_{\text{loc}}(\boldsymbol{r}, t) = \nabla \cdot \frac{\partial \boldsymbol{p}_{\text{loc}}(\boldsymbol{r}, t)}{\partial t} \quad \Rightarrow \quad \frac{\partial \boldsymbol{p}_{\text{loc}}(\boldsymbol{r}, t)}{\partial t} = \boldsymbol{j}_{\text{loc}}(\boldsymbol{r}, t)\,. \tag{4.2}$$

Taking the Fourier transform with respect to time yields the frequency-domain relation

$$-i\omega \boldsymbol{p}_{\text{loc}}(\boldsymbol{r}, \omega) = \boldsymbol{j}_{\text{loc}}(\boldsymbol{r}, \omega)\,. \tag{4.3}$$

This relation extends to the total dipole moment $\boldsymbol{p}(\omega)$ and current $\boldsymbol{j}(\omega)$ by integration. As discussed in section 2.2, employing a discretized spatial basis, the integral reduces to a sum over all localized orbital positions $\boldsymbol{r}_i$

$$-i\omega \sum_i \boldsymbol{p}_{\text{loc}}(\boldsymbol{r}_i, t) = -i\omega \boldsymbol{p}(\omega) = \sum_i \boldsymbol{j}_{\text{loc}}(\boldsymbol{r}_i, \omega) = \boldsymbol{j}(\omega)\,. \tag{4.4}$$

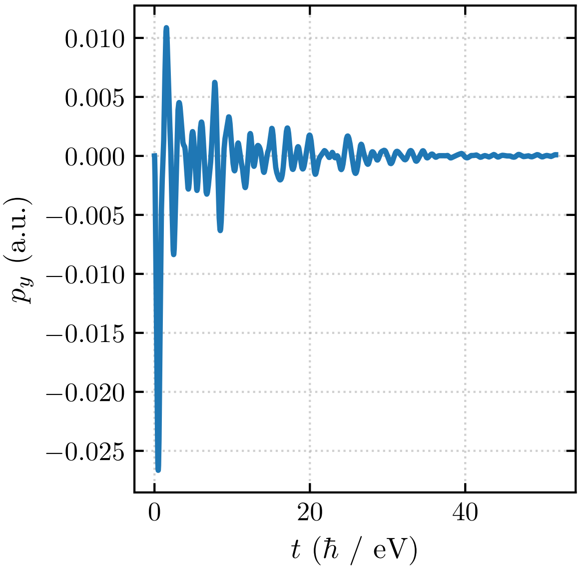

Figure 4.3.: Vibronic polarization (y -component) of a 110-atom rhomboid graphene nanoflake for the damped TA vibration mode described in the main text.

Within GRANAD, both $\boldsymbol{p}(\omega)$ and $\boldsymbol{j}(\omega)$ can be extracted from the output of a time-domain simulation after Fourier transform, as detailed in the previous section.

To verify Equation (4.4) numerically, we simulate the dynamical response of an hBN nanoflake under external illumination for a total duration of $40\,\hbar/\mathrm{eV}$. The nanoflake is chosen to be of rectangular shape and contains 62 atoms in total, while the electric drive takes the form of a pulse peaking at $5\,\hbar/\mathrm{eV}$ with a full width at half maximum of $2\,\hbar/\mathrm{eV}$ at a carrier frequency of $2.3\,\hbar/\mathrm{eV}$. These characterics of the illumination have proven practical to obtain broad-band response spectra of the structures under consideration and thus a satisfactory differentiable approximation of a delta-pulsed excitation.

The expectation values of dipole and current operators are tracked during the evolution, and the Fourier transform is performed numerically after convergence and the resulting spectra are compared. The result, shown in Figure 4.2 for the x -component of the induced current $j_x(\omega)$ and the corresponding dipolar quantity $-i\omega p_x(\omega)$, confirms visually that the continuity equation is satisfied within numerical precision.

Aside from a basic demonstration of correctness, we point out that the numerical verification of Equation (4.4) provides a convenient means to check the convergence of a GRANAD time-domain simulation, provided that the form of the non-Hermitian dissipators is charge conserving. In practice, we recommend checking the correctness of equilibrium dynamics in time domain via the continuity equation, while the TRK sum rule is the preferred option for frequency-domain calculations.

4.1.3. Vibronic Polarization in Graphene Nanoflakes

As a last pedagogical example, we demonstrate GRANAD's capabilities beyond the simulation of external electromagnetic perturbations. We consider a zigzag-edged rhomboid graphene nanoflake to be described by `GRANAD`'s standard graphene tight-binding model in the absence of perturbations, hosting 110 atoms in total. The atomic cores at equilibrium positions $\boldsymbol{R}_i$ are considered to be perturbed by a transverse acoustic (TA) vibration, modelled as a time-dependent displacement out of these equilibrium positions of the generic form

$$\boldsymbol{d}(\boldsymbol{R}_i, t) = \boldsymbol{d}_0 \cdot \sin(\boldsymbol{k}\boldsymbol{R}_i) \cdot \cos(\omega_{\text{ph}} t)\,, \tag{4.5}$$

where we chose the displacement vector $\boldsymbol{d}_0$ to be purely along the y -axis, inducing a maximum strain of 5% of the equilibrium positions. The perturbation is considered to propagate in x -direction only with a spatial frequency of $|\boldsymbol{k}| = \frac{n\pi}{L_x}$, where L_x is the length of the structure in x -direction. With the sound velocity of graphene's TA modes of $v_{\text{TA}} = 13.6\text{km/s}$ [103], the temporal oscillation frequency is thus fixed to $\omega_{\text{ph}} = v_{\text{TA}} \cdot |\boldsymbol{k}|$. We introduce 2 dopant electrons to the structure.

The perturbation is introduced by modulating the hopping rates t_{ij} between orbitals localized at atomic positions $\boldsymbol{R}_i$ and $\boldsymbol{R}_j$ as a function of the out-of equilibrium displacement $\boldsymbol{d}$ according to [104]

$$t_{ij}(\boldsymbol{d}) = t_{ij} \cdot \exp\left[-\beta\left(\frac{|\boldsymbol{R}_i - \boldsymbol{R}_j + \boldsymbol{d}|}{d_0} - 1\right)\right]\,, \tag{4.6}$$

where $d_0 = 1.42$ is the typical equilibrium interatomic distance in graphene and we fix the dimensionless decay constant to $\beta = 3$ in accordance with typical values found in literature [104]. Linearization of this equation in $\boldsymbol{d}$ leads to an independent particle (IP) perturbation term of the form given by Equation (2.33) and thus enables time-domain simulations in `GRANAD`'s framework by implementing a custom interaction term as described in table 3.5. The resulting time-dependent polarization of the nanoflake is displayed in Figure 4.3 for a simulation duration of $52\,\hbar/\text{eV}$. To accelerate convergence and ensure numerical stability, the vibration is modelled to decay exponentially at a rate of $10\,\text{eV}/\hbar$ and we remark that a broad-band linear response calculation would require the modulation of the vibration by a sufficiently narrow pulse. All other parameters correspond to `GRANAD`'s default.

This discussion concludes the demonstration of `GRANAD`'s general purpose capabilities from self-consistent ground state calculations to dynamical simulations under electromagnetic and custom time-dependent perturbation terms. In the next section, we present the application of `GRANAD`'s frequency-domain response engine to conduct research on an exotic material model: Haldane nanoflakes, published in [P3].

4.2. Spin-Selective Response in Topological Nanoflakes

In this section, we discuss nanoflakes described by the Haldane model as a platform for enhanced optical selectivity, supported by electronically topological features [P3]. After a general introductory motivation leading to the topic, we characterize optical selectivity as a differential electromagnetic response to light of different circular polarization and draw the conceptual connection to topologically induced chiral edge states in finite Haldane nanoflakes, which we reason to be of prime importance in amplifying optical selectivity based on an intuitive physical argument. This argument is solidified by concrete linear response calculations conducted via `GRANAD`'s frequency-domain engine, and the topologically enhanced stability of the resulting features against perturbations realized by electronic interactions and random defects is demonstrated. Reproduction code for all figures in this section is freely available [R2].

4.2.1. Motivation

The ability to control and enhance light–matter interactions in ways that depend sensitively on intrinsic properties of the electromagnetic radiation, such as its helicity, or angular momentum, remains a central driver of technological innovation. Applications range from high-efficiency energy harvesting [105] and pharmaceutical processing [106] to the precise transfer of angular momentum from light to matter [107]. Among the various light properties exploited for these purposes, the optical spin angular momentum (SAM) has proven particularly promising for enabling selective copling between electromagnetic fields and tailored material systems [108, 109].

Recent advances in material science have broadened the available platforms for SAM-selective light–matter interactions. In addition to artificial photonic structures [110] and hybrid quantum optical–condensed matter systems [111, 112], topological phases of matter have emerged as an especially intriguing area [113]. Topological condensed matter systems exhibit unconventional scattering, plasmonic [114] and transport behavior [115] that can, in principle, be harnessed for novel photonic functionalities. However, much of the existing work has focused on extended systems, leaving the optical response of finite topological structures, particularly in the context of SAM sensitivity, relatively unexplored. This knowledge gap not only limits our fundamental understanding but also constrains the design space for future photonic devices based on topological principles.

In this section, `GRANAD` is applied to address this gap. Specifically, we investigate nanoflakes described by the prototypical Haldane model, a two-dimensional Chern insulator on a hexagonal lattice featuring broken time-reversal symmetry (TRS) and sublattice symmetry, discussed in subsection 2.4.1. The Haldane model remains a focal point of research across condensed matter and photonics [17, 79, 116, 117], with realizations spanning ultracold fermionic lattices [13], ferromagnetic monolayers [14], Moiré heterostructures [15], and localized spin arrays [16]. Its defining feature,TRS breaking parametrized by an effective pseudo-magnetic field, induces a topological phase transition beyond a critical threshold, marked by the emergence of robust chiral edge states [118, 119].

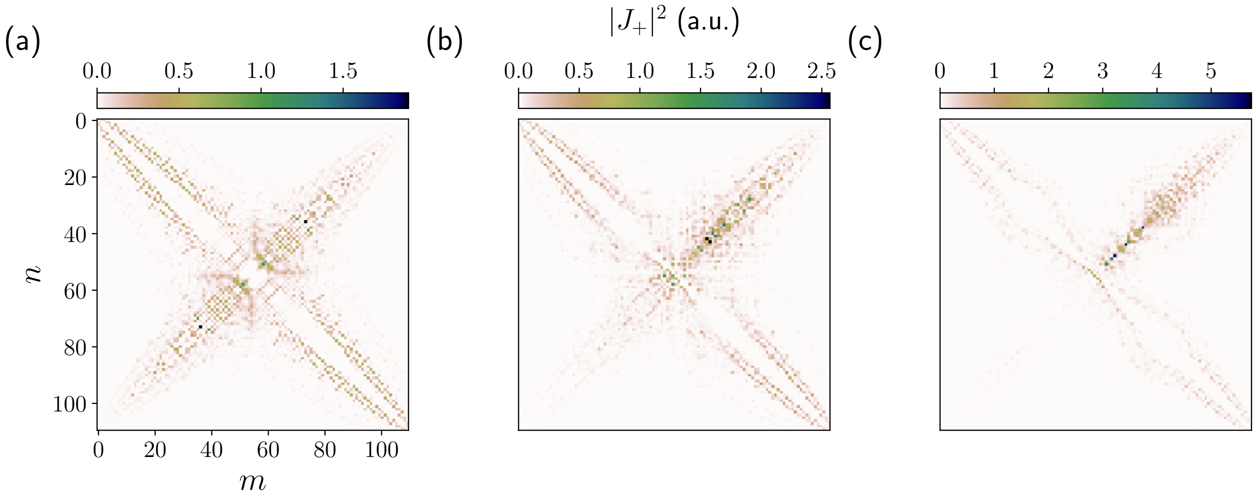

Figure 4.4.: (a)-(c) Absolute value squared of the transition matrix elements corresponding to J_+, evaluated between different energy eigenstates n and m. The underlying system is a rhomboid zigzag-edged nanoflake containing 110 atoms for varying values of λ. (a) Topologically trivial system at $\lambda = 0$. Edge states are absent, TRS is left intact, resulting in a symmetric transition matrix. (b) Topologically trivial system at λ to $0.1t$, but with broken TRS, leading to an asymmetric transition matrix element distribution. (c) Topological system at $\lambda = 0.2t$. The absolute value of the transition matrix elements is increased considerably.

Using `GRANAD`, we demonstrate that finite Haldane nanoflakes exhibit strongly differential coupling to the SAM of normally incident plane waves. This differential response positions them as candidate platforms for SAM-sensitive optical functionalities, including selective absorption, polarization filtering, and phase control. The simulations enable a systematic exploration of how TRS breaking, topological properties, and finite-size effects collectively determine the strength and robustness of SAM selectivity. These results illustrate not only a concrete photonic application of topological nanostructures but also the power of `GRANAD` to probe regimes inaccessible to purely analytical approaches.

4.2.2. Optical Selectivity

In this subsection, we provide a generic argument to the emergence of SAM-selectivity in finite Haldane nanoflakes based on an intuitive analysis of the transition matrix elements associated with SAM-projected components of the current operator.

As discussed in subsection 2.4.1, finite two-dimensional Chern insulators, such as nanoflakes described by the Haldane model, possess edge states whose transport properties are inherently chiral. In these systems, edge currents follow a fixed circulation path around the sample: clockwise or counterclockwise depending on the sign of the time-reversal-symmetry (TRS) breaking parameter λ entering the Hamiltonian in Equation (2.35). Within the convention adopted here, $\lambda > 0$ corresponds to clockwise edge current flow. These edge state are discussed in more detail along with a visualization of an example edge state in subsection 2.4.1. The inherent directionality of the edge states renders topological nanoflakes natural candidates for differential coupling to the two SAM-components of light, which in a normally incident plane wave correspond to opposite in-plane rotational field patterns [120].

To quantify this coupling, we expand the incident field into its SAM components E_σ via the projection

$$E_\sigma = \langle \boldsymbol{e}_\sigma, \boldsymbol{E} \rangle \,, \quad \sigma = \pm 1 \,, \tag{4.7}$$

where the circular polarization basis vectors $\boldsymbol{e}_\sigma$ are

$$\boldsymbol{e}_\sigma = \frac{1}{\sqrt{2}}(\boldsymbol{e}_x + i\sigma \boldsymbol{e}_y) \,. \tag{4.8}$$

In the paraxial regime of a normally incident plane wave, SAM coincides with the total angular momentum of light [121], simplifying the separation between spin and orbital contributions. The incident vector potential couples to the paramagnetic current operator $\boldsymbol{J}$, determined according to Equation (2.28).

Utilizing the projection in Equation (4.7), we extract the SAM-sensitive components of the current operator J_σ as follows

$$J_\sigma = \langle \boldsymbol{e}_\sigma, \boldsymbol{J} \rangle \,, \quad \sigma = \pm 1 \,. \tag{4.9}$$

This definition implies that the operators $J_+(J_-)$ encode coupling to the purely positive (negative) SAM component of the incident light. In the material itself, we generally expect cross-coupling to occur in form of, *e.g.*, non-zero components of the associated response function, such as $G_{J_+J_-}(\omega)$. The non-Hermitian nature of Equation (4.9) makes clear that transitions favored for one SAM component are necessarily suppressed for the other. The bias of one SAM-component over the other is encoded in the TRS breaking parameter λ, and we anticipate λ to be the primary driver of SAM-selective optical response in Haldane nanoflakes.

An illustration of this argument is provided in Figure 4.4, where we display $|J_+|^2$ for varying values of λ in different topological regimes. In the topologically trivial regime displayed in Figure 4.4 (a), the system characterized by $\lambda = 0$. The transition matrix elements are symmetrical. As a result, we expect no differential optical SAM-selectivity. In Figure 4.4 (b), TRS is broken at $\lambda = 0.1t$, which results in an asymmetric distribution, and, consequently, a SAM-selective response. We expect, however, that this SAM-selective response is sensitive to external perturbations, as it lacks topological protection. In Figure 4.4 (c), the system is in its topological phase with $\lambda = 0.2t$ and exhibits strong asymmetry in its transition matrix elements, indicating a strongly selective response. In contrast to the topologically trivial, TRS-broken phase, we expect this response to be a robust effect, largely independent of geometric and electronic interaction details, making it independent of the concrete experimental realization of the Haldane model.

As the physical consequence of TRS breaking in finite nanoflakes, we expect the chiral edge states to be crucial in determining the SAM-selective optical response. In the next

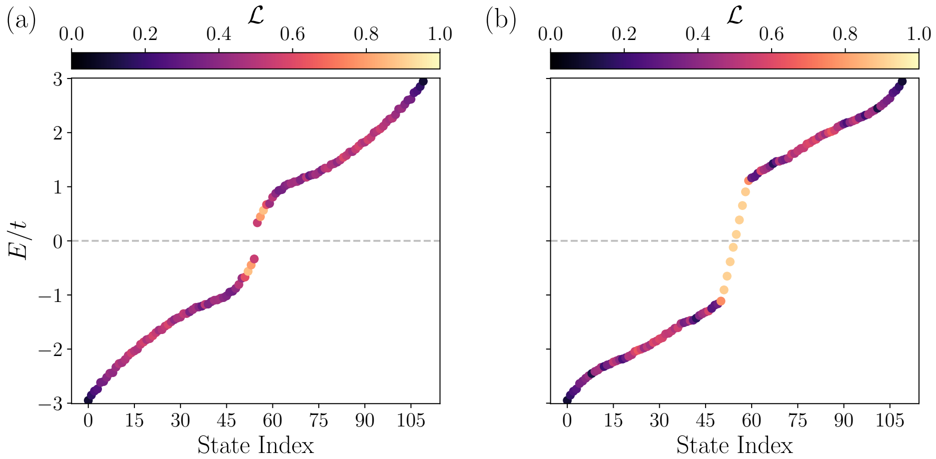

Figure 4.5.: (a) Energy spectrum of a topologically trivial nanoflake at $\lambda = 0.05t$. The rhomboidal structure has a width and height of 53 Å and 30.5 Å, respectively, containing 478 atoms in total. The color coding indicates the localization metric defined in Equation (4.10). The absence of states near the Fermi level prevents low-frequency optical transitions. (b) Same as (a), but for the topologically non-trivial case $\lambda = 0.3\ t$. Strongly localized edge states appear around the Fermi level, enabling low-frequency transitions and making the optical response predominantly topological.

subsection, we turn to a characterization of these edge states before we provide concrete numerical evidence for the SAM-selective response in Haldane nanoflakes.

4.2.3. Edge State Characteristics

In this subsection, we investigate the role of topological edge states in determining the SAM-selective optical response of finite Haldane nanoflakes.

In finite nanoflakes, the continuum of bulk bands collapses into discrete molecular-like energy spectra, as illustrated in Figure 4.5. In the trivial regime, displayed in Figure 4.5 (a), the HOMO–LUMO energy spacing reflects the bulk band gap in infinite systems [17]. For topological flakes as shown in Figure 4.5 (b), however, a family of highly localized states emerges within the bulk gap. These states can be interpreted as a discrete “spectral subsample” of the metallic one-dimensional topological bands found in semi-infinite systems [122]. The presence of such mid-gap edge states enables optical transitions at energies significantly lower than the bulk gap.

Because these transitions occur between edge states, their optical coupling inherits the SAM-sensitivity observed in the bulk case [17], but now manifests at much lower photon energies. In the normally incident plane-wave geometry considered here, the SAM components correspond to left- and right-circular polarizations [123]. The low-energy nature of edge-to-edge transitions thus differentiates them sharply from the predominantly interband-driven transitions in the bulk.

The SAM-preference of a specific transition between eigenstates n and m can be inferred from the SAM-sensitive current matrix elements: As discussed in the previous section, a preference for positive SAM implies $|J^+_{nm}| > |J^-_{nm}|$. This link connects the qualitative edge-state picture to the asymmetric transition matrices shown in Figure 4.4.

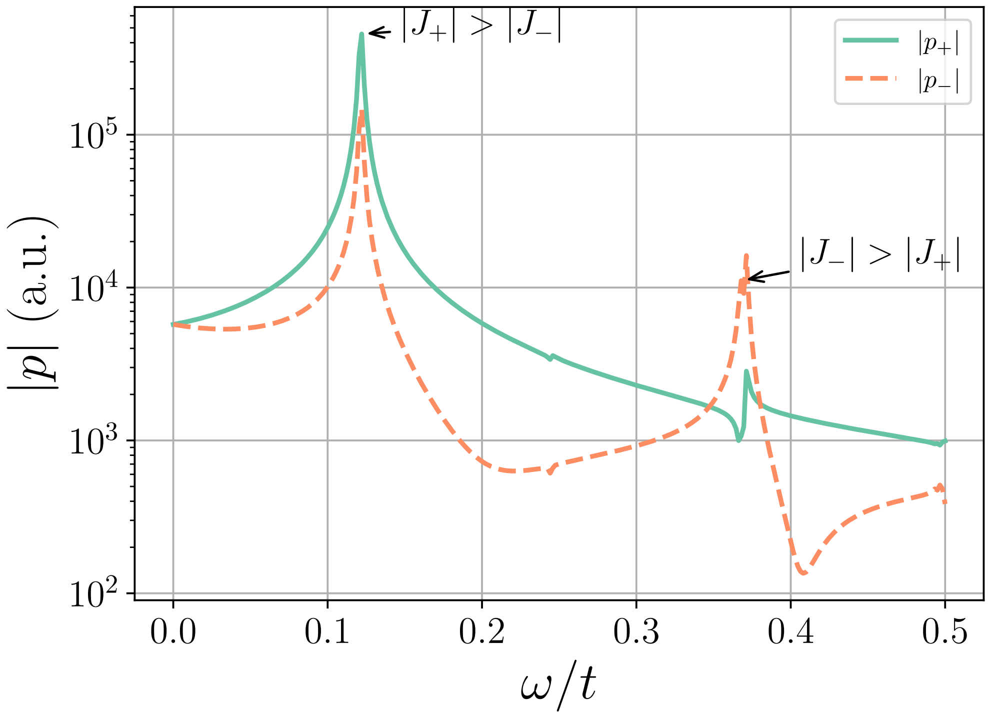

Figure 4.6.: Dipolar response of a rhomboid nanoflake with a width and height of 53 Å and 30.5 Å, respectively, in the topological regime ($\lambda = 0.4t$) under unpolarized illumination. The induced dipole moment is decomposed into its SAM-positive and SAM-negative components, revealing strong differential coupling. The dominant SAM sign changes with frequency: positive SAM dominates at the lower-frequency (HOMO–LUMO) resonance, while negative SAM dominates at the higher-frequency resonance corresponding to the next-lowest excitation.

To quantify the edge localization in our numerical analysis, we introduce the metric

$$\mathcal{L} = \frac{\sum_{j \in \text{edge index}} |\phi_j|^2}{\sum_i |\phi_i|^2}, \tag{4.10}$$

where ϕ_i is the amplitude of the eigenstate on site i, and the numerator sums only over atoms identified as belonging to the flake's outermost edge. Figure 4.5 compares the trivial and topological regimes for a rhomboid flake with 478 atoms. In the trivial case, the HOMO–LUMO gap of $\sim 0.7t$ agrees with the expected bulk gap of $\sim 0.5t$ in the large-size limit. In the topological case, mid-gap edge states collapse the HOMO–LUMO gap, producing a low-frequency optical response dominated by SAM-selective transitions. The combination of TRS-broken current operators and mid-gap edge states explains the strong SAM discrimination observed in the following linear-response calculations.

4.2.4. Dipolar Response Spectra

In this subsection, we investigate the implications of SAM-selectivity in topological nanoflakes described by the Haldane model by performing a linear-response analysis of the induced

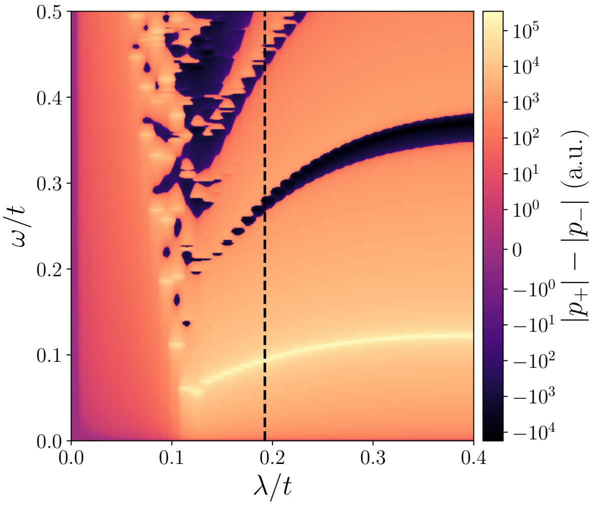

Figure 4.7.: Differential SAM selection, $|p_+| - |p_-|$, for varying λ in the same geometry as Figure 4.6. The vertical dashed line marks the bulk phase transition. For small λ, selectivity is weak and shifted to higher frequencies. Near the bulk transition, selectivity is strongly enhanced, with two main resonances dominated by positive and negative SAM, respectively. A symmetric log scale is used: values in the range $[-1, 1]$ are mapped linearly, larger magnitudes logarithmically.

dipole moment. This approach reveals SAM-selective resonances that are stabilized and amplified by transitions involving edge currents in a parameter range of λ closely matching the bulk topological phase.

The nanoflakes studied here are of molecular-scale dimensions, while the wavelength of the incident light is much larger than the system size. Consequently, the electromagnetic response to an external field $\mathbf{E}(\omega)$ of frequency ω is well described by an induced electric dipole moment $\mathbf{p}(\omega)$ computed according to the IP dipole–dipole correlator in the Lehmann representation Equation (2.62). We specialize to the case of zero temperature and chose the numerical broadening parameter γ as 0.001 eV, similar to [124, 125]

Following Equation (4.7), we decompose the dipolar response $\boldsymbol{p}(\omega)$ for an unpolarized external field into SAM-positive (p_+) and SAM-negative (p_-) components to probe the polarizing behavior of the nanoflakes. Deep in the topological regime ($\lambda = 0.4t$), Figure 4.6 shows the induced dipole moment in the low-frequency range ($0 < \omega/t < 0.5$). A clear asymmetry emerges: at lower frequencies, the induced dipole moment is dominated by the SAM-positive component, whereas at the upper end of the frequency range, a resonance dominated by the SAM-negative component appears. As discussed in subsection 4.2.2 and subsection 4.2.3, this behavior reflects the dominance of one microscopic current operator over the other at a given frequency. The low-frequency SAM-positive resonance corresponds to the HOMO–LUMO transition, where J_+ dominates over J_-. Conversely, the SAM-negative resonance corresponds to the next higher-energy transition, where J_- dominates. The peaks observable in the figure are spectrally degenerate in the sense that both the SAM-positive and the SAM-negative response attain their local maxima at the same frequency values. We later trace back this effect to the presence of

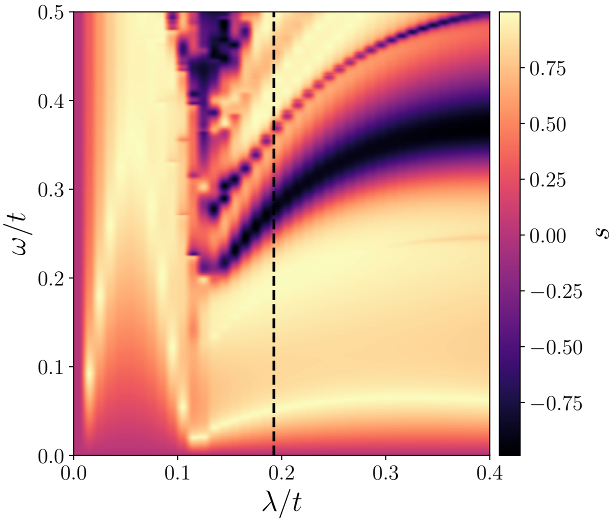

Figure 4.8.: SAM-selectivity s, as defined in Equation (4.11). Distinct behavior across different parameter regimes can be observed. Below the region approximately corresponding to the bulk phase transition, similar to the regime shown in Figure 4.7, a selectivity is present but exhibits distorted patterns, consistent with the lower intensity response observed in that figure. In contrast, the patterns become more stable beyond this regime, and resonances are more clearly defined, aligning with the increased yield seen in other figures. The geometry remains unchanged, and the dashed line marks the bulk phase transition.

inversion symmetry in the rhomboid structure under investigation.

The emergence of SAM-selective resonances in the topological regime can thus be understood as a competition between clockwise and counterclockwise microscopic current channels. The HOMO–LUMO resonance appears at the lowest frequency as a strong SAM-positive feature. While the background response generally favors positive SAM, the higher-frequency resonance reverses the dominant current directionality.

Further insight is gained by examining the dependence of the SAM selection difference $|p_+| - |p_-|$ on λ, displayed in Figure 4.7. For small λ, selectivity is weak and located at higher frequencies. As λ approaches the value necessary for the bulk topological transition, selectivity strengthens significantly. After having laid out the fundamental physical effects of SAM-selectivity depending on the TRS-breaking parameter, we now turn to a quantitative analysis of the optical selectivity.

4.2.5. Assessing Optical Selectivity

To quantify the SAM selectivity, which we denote by s in the following, we employ the following definition, analogous to commonly used measures for quantifying differential bulk responses to polarized light [126]

$$s = \frac{I_+ - I_-}{I_+ + I_-}, \tag{4.11}$$

where I_σ denotes the absorbed intensity for incident light with SAM polarization σ, computed from the dipolar response $\boldsymbol{p}(\omega)$. This dimensionless ratio directly quantifies the relative strength of the nanoflake's interaction with each SAM component.

The results in Figure 4.8 show a clear evolution of s across different λ values. Below the approximate bulk topological transition threshold,corresponding to the parameter range in Figure 4.7,selectivity remains but appears irregular and distorted. So, while still present, the observed features trace back more likely to microscopic system details and are thus less likely to persist in actual experimental realizations. Beyond this threshold, patterns become more stable, resonances sharpen, and the selectivity magnitude increases, in agreement with the enhanced optical yield observed for unpolarized incidence. This demonstrates that the phase transition plays a central role in shaping SAM-dependent absorption.

With TRS-breaking now conclusively identified as key driver of SAM-selectivity as well as preliminary evidence pointing towards topological feature stabilization, we next investigate the stability of the presented results against finite-size and geometrical effects, electronic interactions and local perturbations. This analysis confirms our introductory argument of SAM-selectivity being a protected and, thus, robust feature in the topological regime.

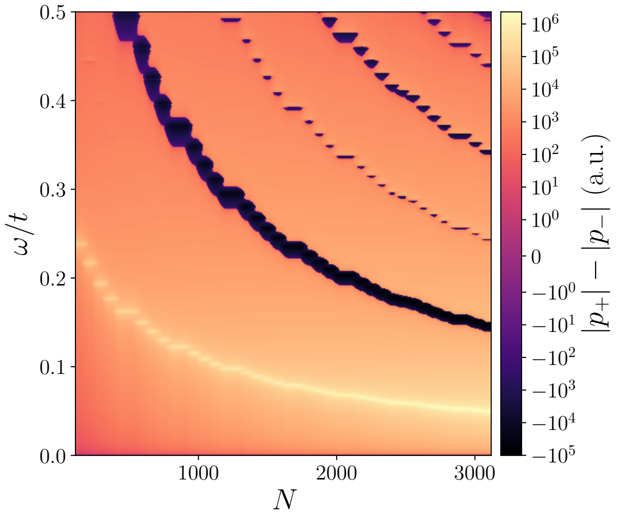

Figure 4.9.: Differential response $|p_+| - |p_-|$ for Haldane nanoflakes of varying sizes, with $\lambda = 0.5t$ fixed deep in the topological regime. Increasing system size results in a redshift and enhanced resonance amplitudes, explained in the main text as a consequence of an increased density of states near the Fermi level. A symmetric log scale is applied as in Figure 4.7.

4.2.6. Finite-size Dipolar Scaling

Up to this point, our analysis focused on a prototypical flake containing ~ 500 atoms. To test the robustness of SAM-selectivity and assess finite-size effects, we evaluate structures from a few hundred atoms up to $\sim 3{,}200$ atoms, with results shown in Figure 4.9.

A systematic trend emerges: larger flakes exhibit a pronounced redshift and an overall enhancement of the resonance amplitudes in $|p_+| - |p_-|$. This is attributable to the increasing density of states near the Fermi level: as the discrete spectrum becomes denser, the optical transitions near the relevant energies approach a quasi-continuum, leading to stronger absorption and enhanced selectivity at slightly lower frequencies. These findings indicate that the observed SAM-selectivity is not only preserved but amplified with increasing size, suggesting similar effects in mesoscopic-scale realizations.

4.2.7. Effects of Spatial Symmetry Breaking

The spectra shown in Figure 4.6 exhibit spectral degeneracy between SAM-positive and SAM-negative resonances. This is due to inversion symmetry in the prototypical rhomboid nanoflake.

To explore the effects of symmetry breaking, we study equilateral triangular nanoflakes with zigzag edges, which lack inversion symmetry. This geometric change removes the symmetry constraint, allowing the spectral positions of SAM-positive and SAM-negative resonances to separate. Figure 4.10 shows the dipolar response for a triangular flake at $\lambda = 0.4t$, where the lifting of the degeneracy is evident. These results highlight that, despite the concrete spectral location of enhanced SAM-selectivity to be determined by symmetry properties of the underlying flake, the feature of SAM-preference is left intact regardless of the geometrical symmetry properties of the underlying Haldane nanoflake.

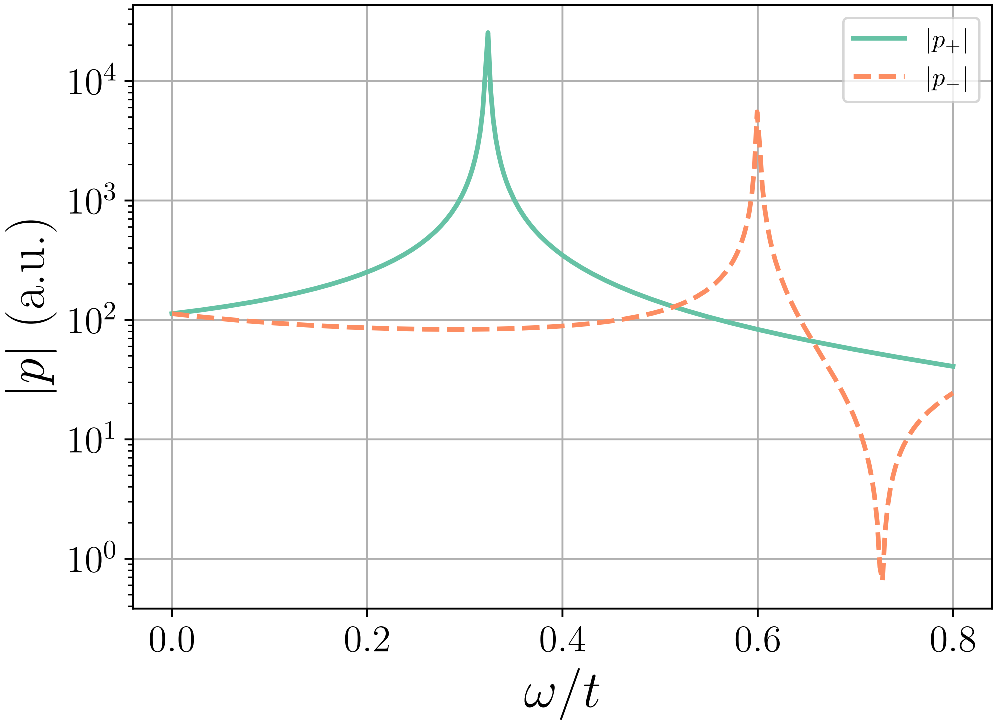

Figure 4.10.: Dipolar response of an equilateral triangular nanoflake with zigzag edges containing 46 atoms, for $\lambda = 0.4t$ under unpolarized illumination. In contrast to the inversion-symmetric rhomboid case, the degeneracy between SAM-positive and SAM-negative resonances is lifted, resulting in a clear spectral separation.

4.2.8. RPA Analysis

Up to this point, our investigation has been carried out within an effective single-particle framework, neglecting explicit electron–electron correlations. Prior studies have shown that such an approach provides adequate qualitative insight for semi-infinite geometries [127]. To further test the robustness of our findings, we extend the analysis by including Coulomb interactions within the random phase approximation (RPA).

Optical features rooted in microscopic topology are expected to be robust against perturbations, including electron–electron interactions. To assess this, we conduct an RPA analysis as discussed in subsection 2.8.4. We introduce a dimensionless scaling factor $c \in [0, 1]$ to the Coulomb matrix controlling the interaction strength, and compute the RPA-corrected dipole–dipole correlator from which $|p_+| - |p_-|$ is obtained. Figure 4.11 shows that interactions mainly cause a blueshift of resonances, leaving the qualitative $|p_+| - |p_-|$ structure intact. This confirms that SAM-selectivity is resilient to moderate many-body effects, reinforcing its potential experimental relevance.

4.2.9. Disordered Potential Analysis

Having confirmed our initial argument of the stability of SAM-selectivity in the topological regime, we now test the resilience of optical selectivity to structural disorder. Disorder

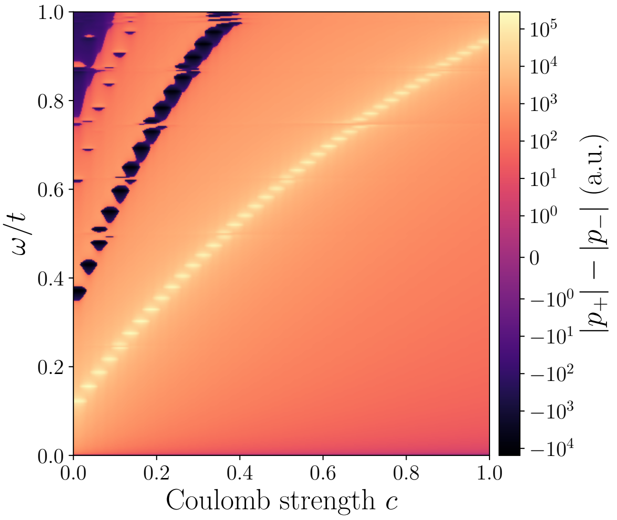

Figure 4.11.: Impact of electron–electron interactions on the dipolar response of a rhombic nanoflake, analyzed within the RPA framework. The system corresponds to Figure 4.6, now including direct-channel Coulomb interactions parameterized by a dimensionless interaction strength c. The primary effect is a blueshift of resonance features, while the qualitative structure of the electromagnetic dipolar selection $|p_+| - |p_-|$ remains intact, indicating robustness of SAM-selectivity against interactions. A symmetric log scale is applied as in Figure 4.7.

is introduced as a random local potential perturbing the onsite hopping term δ in Equation (2.35), following [128]:

$$\delta \rightarrow \delta + r\,, \tag{4.12}$$

where r is drawn from a Gaussian distribution $\mathcal{N}(0, t)$.

Figure 4.12 presents results for the same system as in Figure 4.7, now including this stochastic modification. In the trivial phase, disorder strongly disrupts the optical response, erasing well-defined resonances. This reflects the high sensitivity of non-topological states to geometric and symmetry perturbations, consistent with previous findings for plasmonic responses in graphene nanostructures [129].

In contrast, in the topological phase, selective resonances remain clearly visible and especially the fundamental HOMO–LUMO feature discussed in subsection 4.2.4 is conserved. This persistence is characteristic of topological protection: chiral edge states driving SAM-selectivity are insensitive to moderate local perturbations, depending instead on global invariants rather than fine-tuned microscopic details.

4.2.10. Current–Current Correlator Analysis

As a last validation of the robustness of the numerical results presented so far, we now compare the response theory studied so far, which was based on the dipole–dipole correlator, to its equivalent formulation in terms of the current–current correlator. For a

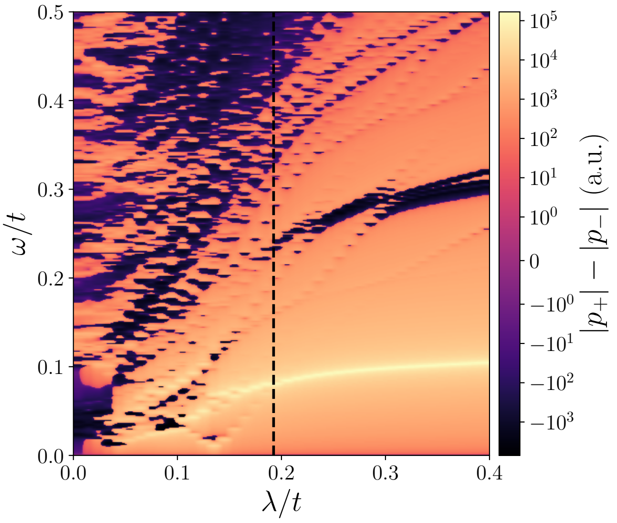

Figure 4.12.: Impact of disorder on the optical selectivity of the Haldane model. In the topological regime, selective resonances remain intact, demonstrating robustness against perturbations.

point-like response at molecular scales, the two are related by

$$G_{PP} = \frac{1}{\omega^2} G_{JJ}\,, \tag{4.13}$$

where G_{PP} denotes the dipole–dipole correlator and G_{JJ} the current–current correlator, where we enforce the TRK sum rule according to the procedure outlined in subsection 2.6.3. Using Equation (4.13), we compute the dipolar selection $|p_+| - |p_-|$ from both G_{PP} and G_{JJ}. As shown in Figure 4.13, the results coincide, confirming the validity of `GRANAD` and demonstrating that SAM-selective properties are independent of the chosen formulation.

4.2.11. Summary

We have investigated the optical properties of Haldane-model nanoflakes and demonstrated their potential for selective light–matter interactions. Our dipolar-response analysis revealed pronounced SAM-selectivity directly linked to chiral edge states, with the effect strongly enhanced in the topological regime near and beyond the bulk phase transition.

Key mechanisms were identified: transitions involving topological edge currents produce strong polarization-dependent absorption, shaped by the interplay of time-reversal symmetry breaking and spatial confinement. The resulting resonance features are robust against moderate parameter variations and disorder, making such nanoflakes promising candidates for tunable optical filters, polarization control devices, and light-based information processing elements.

Finite-size scaling analysis showed that larger flakes yield redshifted and stronger resonances due to an increased density of states near the Fermi level. This suggests the persistence and possible enhancement of SAM-selectivity in larger, experimentally relevant

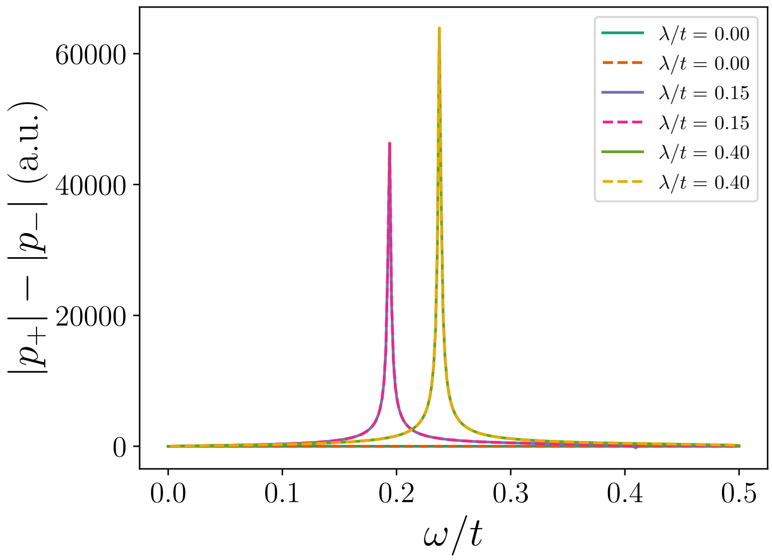

Figure 4.13.: Comparison of dipolar selection computed from the dipole–dipole (G_{PP}, solid lines) and current–current (G_{JJ}, dashed lines) correlators for a rhomboid nanoflake containing 478 atoms, for different values of the topological control parameter λ. The excellent agreement confirms the consistency of both approaches.

structures, bridging the gap from molecular-scale to mesoscopic devices.

While our study centered on the prototypical Haldane model, analogous effects are expected in experimentally realizable platforms. Buckled Xene monolayers (silicene, germanene, stanene, plumbene) offer tunable staggered potentials via external electric fields [17], potentially enabling control over spin-split resonance structures in nanoflakes. Monolayer TMDs such as $\mathrm{MoS_2}$ or $\mathrm{WS_2}$ exhibit larger in-plane photonic spin Hall shifts [17], which may enhance resonance strengths at the cost of reduced tunability.

In summary, our results position topological nanoflakes as versatile building blocks for SAM-sensitive photonic and optoelectronic applications. Future extensions may explore dynamical and nonlinear regimes, alternative edge terminations, and coupled-flake architectures to engineer complex optical responses tailored for next-generation light-based technologies.

5. Quantum Description of Light-Matter Interactions

In this chapter, we review the key theoretical aspects necessary for a fully quantum description of interacting light-matter systems in a cavity. First, we discuss the quantization of cavity light and its interaction with electronic matter. We then detail the construction of an effective Hamiltonian describing the interaction of light with collective matter excitations. This effective Hamiltonian forms the basis of the theoretical analysis we present in the next chapter on our study of chiral cavities.

5.1. Hamiltonians for Quantum Light and Matter

Focussing on the matter sector of the Hamiltonian first, we restate the general quantum Hamiltonian for a system of N electrons, already given in Equation (2.2)

$$H_{\text{el}} = \frac{1}{2m}\sum_{i=1}^{N} \boldsymbol{p}_i^2 + \sum_{i=1}^{N} V(\boldsymbol{R}_i)\,. \tag{5.1}$$

In accordance with the approximations already discussed in the motivation of `GRANAD`'s theoretical framework, we implicitly operate within an independent particle picture where electronic interactions give rise to a nonlinear contribution to $V(\boldsymbol{R}_i)$. We consider the electronic system embedded in a cavity. Interaction with light is modelled by the minimal coupling substitution

$$\boldsymbol{p}_i \to \boldsymbol{p}_i - \boldsymbol{A}(\boldsymbol{R}_i)\,, \tag{5.2}$$

where $\boldsymbol{A}(\boldsymbol{R}_i)$ is the vector potential and we adopt a system of units such that the electronic charge is set to unity. The purely electromagnetic sector of the model is described by the classical Hamiltonian

$$H_{\text{light}} = \frac{1}{2}\int \mathrm{d}\boldsymbol{r}\left[\frac{1}{\epsilon_0\epsilon}\boldsymbol{\Pi}^2(\boldsymbol{r}) + \frac{1}{\mu_0}(\nabla \times \boldsymbol{A}(\boldsymbol{r}))^2\right] \tag{5.3}$$

where $\boldsymbol{\Pi}(\boldsymbol{r})$ denotes the conjugate variable corresponding to $\boldsymbol{A}(\boldsymbol{r})$, and we consider the case of a time-harmonic vector potential.

Turning to quantization, we consider the vector potential to describe electromagnetic modes in a cavity of volume V, filled with a homogeneous, lossless dielectric modelled by ϵ. Closely following the procedure detailed in [130], the light modes can be expanded in a set of basis functions $\boldsymbol{v}_l$, such that $\boldsymbol{A}(\boldsymbol{r})$ and $\boldsymbol{\Pi}(\boldsymbol{r})$ take the form

$$\boldsymbol{A}(r) = \sum_l \boldsymbol{v}_l(\boldsymbol{r})A_l \tag{5.4}$$

$$\boldsymbol{\Pi}(\boldsymbol{r}) = \sum_l \boldsymbol{v}_l^*(\boldsymbol{r})\epsilon B_l\,, \tag{5.5}$$

The functions $\boldsymbol{v}_l$ form an orthogonal basis in the following sense

$$\int \mathrm{d}\boldsymbol{r} \epsilon \boldsymbol{v}_l^*(\boldsymbol{r}) \boldsymbol{v}_k(\boldsymbol{r}) = \delta_{lk} \,. \tag{5.6}$$

Additionally, they obey the Helmholtz equation for the cavity with resonance frequencies ω_i

$$\omega_l^2 \mu_0 \epsilon_0 \epsilon \boldsymbol{v}_l(\boldsymbol{r}) = \nabla \times \nabla \times \boldsymbol{v}_l(\boldsymbol{r}) \,. \tag{5.7}$$

To quantize the light modes, we adopt the usual prescription by replacing the canonical variables A_l and B_l by operators fullfilling

$$[A_l, B_k] = i\delta_{lk} \,. \tag{5.8}$$

These operators, akin to position and momentum, can be expressed according to the bosonic creators $a_l^\dagger$ and annihilators a_l of an ensemble of harmonic oscillators as follows

$$A_l = \frac{1}{\sqrt{2}} \left(a_l + a_l^\dagger \right) \tag{5.9}$$

$$B_l = i\frac{1}{\sqrt{2}} \left(-a_l + a_l^\dagger \right) \,. \tag{5.10}$$

Working in the Coulomb gauge given by

$$\nabla \cdot \boldsymbol{A}(\boldsymbol{r}) = 0 \,, \tag{5.11}$$

we arrive at

$$H = \frac{1}{2m} \sum_{i=1}^{N} \boldsymbol{p}_i^2 + \sum_{i=1}^{N} V(\boldsymbol{R}_i) + \frac{1}{m} \sum_{i=1}^{N} \boldsymbol{A}(\boldsymbol{R}_i) \cdot \boldsymbol{p}_i + \sum_{i=1}^{N} \frac{1}{2m} \boldsymbol{A}(\boldsymbol{R}_i)^2 + \sum_l \omega_l a_l^\dagger a_l \,. \tag{5.12}$$

Proceeding with second quantization with reference to a suitable basis of electronic single particle states $|\phi_i\rangle$ associated with the fermionic ladder operators $c_i^\dagger, c_i$ yields a Hamiltonian of the form

$$H = \sum_{a,b} h_{ab} c_a^\dagger c_b + \sum_{a,b,l} K_{ab}^l c_a^\dagger c_b (a_l^\dagger + a_l) + \sum_{l,a,b} L_{ab}^l c_a^\dagger c_b (a_l^\dagger + a_l)^2 + \sum_l \omega_l a_l^\dagger a_l \,, \tag{5.13}$$

where the diamagnetic (paramagnetic) coupling constants K_{ab}^l, L_{ab}^l are given by

$$K_{ab}^l = \langle \phi_a | \frac{1}{m} \sum_j \boldsymbol{p}_j \cdot \boldsymbol{v}_l(\boldsymbol{R}_j) | \phi_b \rangle \tag{5.14}$$

$$L_{ab}^l = \langle \phi_a | \frac{1}{2m} \sum_j \boldsymbol{v}_l^2(\boldsymbol{R}_j) | \phi_b \rangle \,. \tag{5.15}$$

The Hamiltonian in Equation (5.13) is of a well-known form [131]. We remark that this procedure of obtaining effective light-matter quantum Hamiltonians is more subtle in general. The fundamental issue is the choice of the single-particle basis $|\phi_i\rangle$. As discussed in section 2.2, a low-energy approximation to the electronic sector, such as the single p_z -band picture of graphene fitted in Figure 2.2, is desirable for a multitude of reasons ranging from enhanced physical transparancy to more efficient numerical implementation. The reduction of the basis set to its low-energy elements, however, incurs the cost of incompleteness. For semiclassical treatments involved in the calculation of material response properties, the implicit *projection* onto this low-energy manifold of electronic states is often sufficient to yield accurate results [92]. In this case, comparatively minor adjustments, such as the correction of the current-current correlator to obey the TRK sum rule, presented in subsection 2.6.3, suffice to guarantee physically consistent results [64].

However, when the quantum nature of light becomes prominent, such as in the parametric regime of light-matter interactions termed the *ultrastrong* coupling limit, this approximation may result in a violation of gauge invariance leading to inconsistent results between different models [132]. A widely used alternative to the Coulomb gauge picture presented above, for instance, is given by the dipolar gauge, marked by the absence of the quadratic photon-photon interaction in Equation (5.13), at the cost of introducing additional electron-electron interactions closely related to the classical multipole expansion [133]. The dipolar gauge is typically derived from the Coulomb gauge by a Power-Zienau-Wooley transformation [134], originally formulated within a framework more tailored towards atomic physics [133]. When not treated carefully within a low-energy projection as used in many applications of condensed matter, these two gauges are *not* related by a unitary transformation anymore, implying they can yield different results [135]. This may lead, *e.g.*, to the erroneous prediction of equilibrium superradiance - a phenomenon of collective radiation marked by the presence of electronic ground state currents. This phase has been proven to be impossible to reach at equilibrium a fair number of times [136] [131] [86] [137].

Recent works have developed elaborate techniques to construct gauge-invariant low-energy Hamiltonians incorporating the quantum nature of light within a consistent description across different gauges. They rely, *e.g.*, on a set of controllable parameters such as the number of electronic bands involved in the construction of the low-energy electronic manifold [130] or projected PZW transformations [132].

In this thesis, our primary intent is to explore the interaction of chiral matter systems with cavity light in coupling regimes characterized by a photonic system spectrally tuned to closely match the resonant frequencies of electronic *excitations*. In this case, the fundamental interaction dominating the physical behavior of the matter system is best described not in terms of electrons, but in terms of quasiparticles of matter excitations that behave as bosons. Examples of these quasiparticles are excitons coupling to cavity light to form exciton-polaritons [138]. In this setting, physically realistic and gauge invariant effective Hamiltonians involving boson-boson interactions only without explicit reliance on an underlying low-energy model of matter have already been established in the literature [60], which allows us to largely sidestep the delicate issue of constructing gauge invariant Hamiltonians incorporating a low-energy electronic sector. For a detailed discussion of the intricacies involved in this procedure, the interested reader is therefore referred to the relevant literature [132] [130]. In the next section, we illustrate the construction of effective bosonic models for interacting light-matter systems and motivate the form of the Hopfield-type model employed in our theoretical investigations.

5.2. Effective Bosonic Models

In this section, we provide a heuristic derivation of the purely bosonic, Hopfield-type Hamiltonian which will be the main subject of our theoretical investigation of chiral interactions between matter excitations and cavity light. To this end, consider the Coulomb-gauged matter system in Equation (5.13) to be characterized completely by two types of orthogonal and highly localized orbitals at lattice sites numbered by i. We describe annihilation of electrons in these orbitals using the operators $c_{1,i}$ and $c_{2,i}$. The onsite orbital energy difference we denote by Δ and restrict hopping to nearest neighbors with rate $t_{12} = t_{21}$ for electron transfer between orbitals of different type only, such that transfer between identical orbitals is considered forbidden or suppressed by the underlying crystal symmetry. In addition, we consider the cavity fields well described by the long-wavelength approximation, such that a microscopic desciption of the matter system is not required as the photonic mode functions probe it uniformly. This chain of approxmations is justified since our theoretical investigation is centered on systems of molecular extent. Denoting the uniform value of the l -th light mode function across the matter system by the constant vector $\boldsymbol{v}_l$, the light-matter couplings simplify to

$$K^l_{ab} = \boldsymbol{v}_l \boldsymbol{j}_{ab}\,, \tag{5.16}$$

$$L^l_{ab} = \frac{1}{2m}\boldsymbol{v}_l^2\,, \tag{5.17}$$

where $\boldsymbol{j}_{ab}$ denotes the paramagnetic current operator matrix element between orbitals indexed by a and b and the diamagnetic term L^l_{ab} is independent of the orbital degree of freedom. Due to Equation (2.28) and the absence of intrasite currents, the only non-zero elements of this matrix are the translationally invariant amplitudes between neighboring orbitals, denoted by $\boldsymbol{j}_{1,2}$. The Hamiltonian can then be written as (with $\langle i,j\rangle$ denoting nearest neighbors)

$$H = \frac{\Delta}{2}\sum_i \left(c^\dagger_{2,i}c_{2,i} - c^\dagger_{1,i}c_{1,i}\right) + t_{12}\sum_{\langle i,j\rangle}\left(c^\dagger_{1,i}c_{2,j} + \text{h.c.}\right) \tag{5.18}$$

$$+ \sum_l (a^\dagger_l + a_l)\boldsymbol{v}_l \sum_{\langle i,j\rangle} \boldsymbol{j}_{1,2}\left(c^\dagger_{1,i}c_{2,j} + \text{h.c.}\right) \tag{5.19}$$

$$+ \sum_l \frac{\boldsymbol{v}_l^2}{2m}(a^\dagger_l + a_l)^2 \sum_i (c^\dagger_{1,i}c_{1,i} + c^\dagger_{2,i}c_{2,i}) \tag{5.20}$$

$$+ \sum_l \omega_l a^\dagger_l a_l\,. \tag{5.21}$$

Going to Fourier space and disregarding microscopic details of the matter system by focussing on the k -space sector of uniform modes with $k = 0$ yields the (truncated) Hamiltonian

$$H_{\text{truncated}} = -\frac{\Delta}{2}s_3 + \left(t_{12}\sum_l (a_l^\dagger + a_l)\boldsymbol{v}_l\boldsymbol{j}_{1,2}\right)s_1 \tag{5.22}$$

$$+\sum_l \frac{\boldsymbol{v}_l^2}{2m}(a_l^\dagger + a_l)^2 s_0 \tag{5.23}$$

$$+\sum_l \omega_l a_l^\dagger a_l \tag{5.24}$$

where the composite operators s_i are related to the usual Pauli matrices σ_i by

$$s_i = \Psi^\dagger \sigma_i \Psi\,, \tag{5.25}$$

$$\Psi = \begin{pmatrix} c_{1,k=0} \\ c_{2,k=0} \end{pmatrix}. \tag{5.26}$$

They represent the degrees of freedom associated to the matter excitations. To map these operators to bosonic creators and annihilators $b^\dagger, b$, we perform a Holstein-Primakoff transformation [132]

$$s_1 = \sqrt{N}(b + b^\dagger), \tag{5.27}$$

$$s_2 = -i\sqrt{N}(b - b^\dagger), \tag{5.28}$$

$$s_3 = N - 2b^\dagger b\,, \tag{5.29}$$

where $[s_1, s_2] = 2iN$ and $[s_1, s_3] = -2is_2$ and we have additionally set $s_0 = N$. We introduce the coupling constants

$$L^l = \sqrt{N}\boldsymbol{v}_l\boldsymbol{j}_{1,2}\,, \tag{5.30}$$

$$D^l = \frac{N}{2m}\boldsymbol{v}_l^2\,. \tag{5.31}$$

After dropping a scalar constant, we obtain the effective Hamiltonian

$$H_{\text{eff}} = \Delta b^\dagger b + \sum_l L^l(a_l^\dagger + a_l)(b^\dagger + b) + \sum_l D^l(a_l^\dagger + a_l)^2 + \sum_l \omega_l a_l^\dagger a_l\,. \tag{5.32}$$

We have thus arrived at a theoretical description in terms of interacting bosons that is largely analogous to the well-known Hopfield model [60].

The heuristic derivation given above implicitly assumes the description of the matter system immersed in the cavity as an effective two-band system to be complete. As discussed, this assumption is not valid in general. Instead, the coupling parameters need to be obtained from a careful low-energy projection most easily performed in the dipolar gauge [113] or can even be constructed from *ab initio* calculations [40].

Following [60], however, we will forego a concrete microscopic model and consider the relevant model parameters to be essentially free. A straightforward generalization of Equation (5.32) to the case of multiple matter modes, which we consider spectrally degenerate for simplicity, is given by

$$H = \Delta \sum_{n} b_n^\dagger b_n + \sum_{m,n} L_{nm}(a_m^\dagger + a_m)(b_n^\dagger + b_n) + \sum_{m,n} D_{nm}(b_m^\dagger + b_m)(b_n^\dagger + b_n) + \sum_{m} \omega_m a_m^\dagger a_m \, . \tag{5.33}$$

Gauge invariance can then be ensured by relating the couplings L_{nm} and D_{nm} according to the TRK sum rule. A generalization of the expression given in [60] to the multimode case yields

$$D_{ij} = \sum_{nm} \frac{L_{ni} L_{mj}}{\Delta} \, . \tag{5.34}$$

The Hamiltonian given by Equation (5.33) with parameters restricted by the expression above will constitute the basis of investigation of the next chapter, where we present results pertaining to the case of a chiral cavity loaded with enantiomeric molecules.

6. Enantiomer Selectivity and Energy Transfer in Imperfect Chiral Cavities

In this chapter, we turn to the specific case of chiral light–matter coupling in a bosonic setting, following the general theoretical framework laid out previously. To this end, we specialize the general bosonic framework to a two-mode chiral cavity and develop what we refer to as the *chiral Hopfield model*. This model enables a compact yet fully quantum description of light–matter coupling in enantiomeric mixtures immersed in a cavity supporting two modes of opposite chirality, naturally incorporating diamagnetic corrections required for gauge invariance. Its quadratic structure in both light and matter operators allows for diagonalization *via* a Hopfield–Bogoliubov transformation. This yields a new set of quasiparticles, called polaritons, that embody hybridized light–matter excitations.

The remainder of this chapter is structured as follows. In section 6.1, we introduce the chiral Hopfield Hamiltonian and discuss the physical meaning of its parameters. We then analyze the resulting polaritonic spectrum in section 6.2, emphasizing the dependence of mode composition on cavity imperfections and enantiomeric ratios. In section 6.3, we examine the energy transfer characteristics of the cavity under external driving using an S -matrix approach analogous to standard input–output theory. Finally, we summarize the implications of our findings in **??**, with a brief outlook toward dissipative and open-cavity extensions of the model.

The simulation code to reproduce the results of this chapter is available at [R3].

6.1. Model Hamiltonian

To investigate the quantum properties of chiral light–matter coupling, we consider a cavity supporting two chiral photonic modes of opposite handedness. The cavity contains enantiomeric molecules that can interact selectively with the corresponding circular polarization states of light. The coupled light–matter system is described by a bosonic Hopfield-type Hamiltonian of the form derived in Equation (5.33), specialized to the case of two photonic modes. For clarity, we write this Hamiltonian as a sum of the following contributions

$$H = H_0 + H_{\text{light–matter}} + H_{\text{light–light}} \,, \tag{6.1}$$

where the three terms respectively describe the uncoupled subsystems, the light–matter interaction, and the diamagnetic photon–photon coupling.

6.1.1. Uncoupled light and matter excitations

The free Hamiltonian of the cavity and molecular excitations corresponds to the free harmonic oscillator terms in Equation (5.33). It reads

$$H_0 = \sum_{i \in \{+,-\}} \omega_i^0 \, a_i^\dagger a_i + \omega_b \sum_{i \in \{+,-\}} b_i^\dagger b_i \, . \tag{6.2}$$

Here, $a_\pm$ denote annihilation operators for right- and left-handed cavity photons with bare frequencies $\omega_\pm^0$, and $b_\pm$ represent bosonic annihilators for collective matter excitations (*e.g.*, excitons or molecular transitions) of opposite handedness, both assumed to have the same eigenfrequency ω_b. As discussed previously [138], the bosonic approximation for these matter modes is valid in the low-excitation, collective limit.

6.1.2. Light–matter coupling

The interaction between the photonic and matter components corresponds to the term mixing bosonic operator species in Equation (5.33) and is given by

$$H_{\text{light–matter}} = \sum_{m,n \in \{+,-\}} l_{mn} \left(a_m^\dagger + a_m \right) \left(b_n^\dagger + b_n \right) \, , \tag{6.3}$$

where the coupling constants l_{mn} capture both the overall interaction strength and the chiral selectivity of the coupling. Following [38, 139], we parameterize them as

$$l_{mn} = \gamma_n \left(1 + g \, \cdot m \cdot n \right) \, , \tag{6.4}$$

with the identification $+ \equiv +1$ and $- \equiv -1$, such that, *e.g.*, $l_{+-} = \gamma_n(1-g)$. The amplitude $\gamma_n \propto \sqrt{N_n}$ represents the effective collective coupling strength for the n -th enantiomeric species, scaling with the square root of the number of molecules N_n contributing to that species. Similar to the closely related model given in [139], γ_n may be related to cavity and molecular parameters *via*

$$\gamma_n = \sqrt{N_n \frac{\omega}{2\epsilon_0 V}} \, , \tag{6.5}$$

where V is the cavity volume, ϵ_0 the vacuum permittivity, and ω the mode frequency. The independence on N_n stems from the fact

The chirality parameter g can be expressed in terms of the molecular transition dipole moments [139]

$$g = \frac{\mathrm{Im}[\boldsymbol{d} \cdot \boldsymbol{m}]}{|\boldsymbol{d}|^2} \, , \tag{6.6}$$

where $\boldsymbol{d}$ and $\boldsymbol{m}$ denote the electric and magnetic transition dipole moments, respectively. Perfectly chiral molecules couple exclusively to one helicity, corresponding to $|g| = 1$, but realistic molecular systems typically exhibit much smaller values ($|g| \ll 1$). Unless otherwise stated, we consider a representative value $g = 0.01$ in the numerical analyses.

6.1.3. Diamagnetic photon–photon interaction

The self-interaction of the cavity photon modes is accounted for by a diamagnetic term of the form

$$H_{\text{light–light}} = \sum_{i,j\in\{+,-\}} D_{ij} \left(a_i^\dagger + a_i\right) \left(a_j^\dagger + a_j\right) , \tag{6.7}$$

where the coupling constants D_{ij} ensure gauge invariance and prevent the appearance of unphysical ground-state currents. As discussed, they are determined by the TRK sum rule [132, 140], which in this context yields

$$D_{ij} = \sum_{m,n\in\{+,-\}} \frac{l_{ni}\,\bar{l}_{mj}}{\omega_b} . \tag{6.8}$$

Neglecting $H_{\text{light–light}}$ is typically acceptable in the weak-coupling regime. However, in the ultrastrong and deep-strong coupling limits, this term is essential to recover correct physical behavior [60, 141].

6.1.4. Diagonalization and coupling regimes

Because the Hamiltonian in Equation (6.1) is quadratic in both light and matter operators, it can be diagonalized exactly using a Hopfield–Bogoliubov transformation [132]. This yields a set of polariton modes with frequencies ω_i and corresponding operators β_i satisfying

$$H = \sum_i \omega_i\, \beta_i^\dagger \beta_i . \tag{6.9}$$

Collecting the bare operators in the vector

$$\boldsymbol{c} = \begin{pmatrix} a_+ \\ a_- \\ b_+ \\ b_- \end{pmatrix} , \tag{6.10}$$

the polaritonic operators can be written as

$$\boldsymbol{\beta} = \begin{pmatrix} \boldsymbol{p} \\ \boldsymbol{p}^\dagger \end{pmatrix} = T \begin{pmatrix} \boldsymbol{p} \\ \boldsymbol{p}^\dagger \end{pmatrix} , \tag{6.11}$$

where T is a paraunitary matrix encoding the admixture of photonic and matter components in each polaritonic mode [132] and we apply Hermitian conjugation to each entry in a vector separately instead of transposing the vector.

Depending on the coupling strength γ_n relative to the matter excitation frequency ω_b, several regimes can be distinguished [60]. For $\gamma_n \ll 0.1\,\omega_b$, the rotating wave approximation (RWA) holds, the system reduces to a Jaynes–Cummings-type model. Beyond this limit, counter-rotating terms become significant, defining the *ultrastrong coupling* (USC) regime. When $\gamma_n \sim \omega_b$, perturbative approaches fail altogether, and the system enters the *deep strong coupling* (DSC) regime, where the concept of distinct light and matter excitations loses meaning, the true eigenmodes are intrinsically hybrid polaritons.

In the following sections, we exploit this formalism to analyze the polaritonic dispersion, mode composition, and energy transfer characteristics of imperfect chiral cavities. We begin by investigating the spectral properties of the closed cavity and the role of chiral asymmetry in determining the polariton content.

6.2. Polariton Dispersion

In this section, we analyze the dispersion and composition of polaritonic modes generated by the chiral Hopfield Hamiltonian introduced in section 6.1. Beyond the eigenfrequencies alone, we will make systematic use of the *mode content* to quantify how strongly a polariton resembles each bare (uncoupled) mode.

For the i -th polariton, the contribution from the j -th bare mode is defined as [60]

$$C_j^i = \frac{|T_{ij}|^2}{\sum_k |T_{ik}|^2}, \tag{6.12}$$

where T_{ik} parameterizes the paraunitary Hopfield–Bogoliubov transformation introduced in Equation (6.11). By construction, $C_j^i \to 1$ if the i -th polariton coincides with the j -th bare mode, which makes C_j^i a convenient indicator of (de)coupling and light-matter mixing. While C_j^i is primarily a diagnostic of the underlying physics, it correlates qualitatively with observables such as spontaneous emission rates [60]. We will denote the positive- and negative-handed *matter* content of mode i by C_+^i and C_-^i, respectively.

6.2.1. Perfectly Chiral Cavity with a Single-Handed Ensemble

We begin with the canonical case often discussed in the literature [38]: a perfectly chiral cavity supporting only one helicity and containing a single enantiomeric species of matching handedness. In our notation, this amounts to setting $\gamma_- = 0$ and discarding the opposite-helicity cavity mode, so that the light-matter matrix in Equation (6.4) reduces to a single nonzero entry l_{++}.

Figure 6.1 shows the resulting polariton branches for an illustrative parameter set. As the coupling γ_+ increases from the RWA-applicable regime into strong coupling, the familiar level repulsion between the lower and upper branches emerges [142]. At weak coupling, the lower polariton is dominantly matter-like while the upper is dominantly photonic, consistent with the bare picture. With increasing γ_+, the two branches mix more strongly. Importantly, this trend is non-monotonic: once ultrastrong and deep-strong coupling are approached, the diamagnetic term in Equation (6.7) reduces the *effective* coupling, driving the lower (upper) branch back toward matter-like (light-like) character. This mirrors the established non-chiral scenario, already discussed in [60], but sets the stage for our discussion of effects pertaining to chiral selectivity in more complex settings.

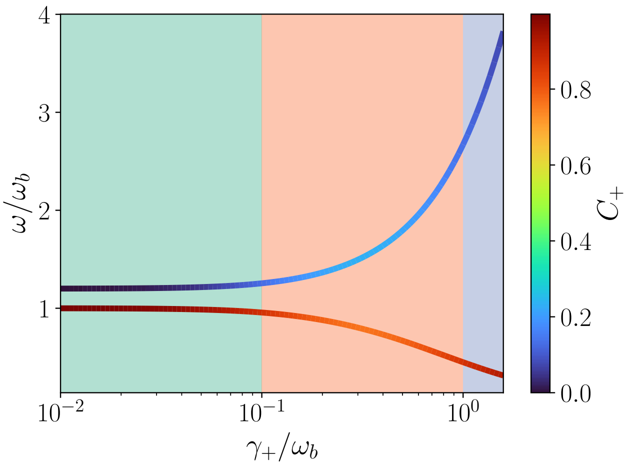

Figure 6.1.: Polaritonic eigenfrequencies ω normalized by ω_b, annotated by the positive-handed matter content C_+. Background shading indicates coupling regimes: RWA-applicable (green), USC (red), and DSC (gray). The cavity hosts a single enantiomer ($g = 0.01$) and a single $+$-helicity mode at $\omega_+^0 = 1.2\,\omega_b$. At small γ_+ the lower (upper) polariton is matter- (light-) dominated; mixing increases with γ_+ but becomes non-monotonic as diamagnetism reduces effective coupling in the DSC regime.

6.2.2. Perfectly Chiral Cavity with a Mixed-Handed Ensemble

We now introduce a second enantiomeric species of opposite handedness while keeping the cavity perfectly chiral (only the $+$ helicity is present). In this case, l_{++} and l_{+-} are both nonzero. To quantify chiral discrimination in the polaritons, we define the *excess* positive-handed matter content,

$$\Delta^i = C_+^i - C_-^i\,, \tag{6.13}$$

so that large $|\Delta^i|$ indicates strong handedness selectivity.

Figure 6.2 shows the evolution at resonance ($\omega_+^0 = \omega_b$) for fixed $\gamma_+/\omega_b = 0.1$ as γ_- is increased. A third branch, pinned near ω_b at $\gamma_- \to 0$, appears in addition to the familiar upper and lower polaritons; it is continuously connected to the uncoupled negative-handed matter mode. As γ_- grows, matter components of opposite handedness mix across all branches and Δ decreases for the upper and lower polaritons, signaling reduced chiral selectivity. In the racemic limit $\gamma_- = \gamma_+$, the excess positive-handed content in those polaritons is strongly suppressed, demonstrating that molecular composition alone can substantially degrade selectivity even in a perfectly chiral cavity.

Given that most natural molecules are only weakly chiral [123], one may ask whether stronger *intrinsic* chirality can preserve selectivity. Figure 6.3 confirms this expectation: for larger g (typically $g \gtrsim 0.5$), the upper and lower polaritons maintain a sizable excess of positive-handed matter across a wide range of γ_-/γ_+. In the idealized limit $g = 1$, negative-handed matter decouples from the $+$ -helicity cavity mode, rendering variations in γ_- irrelevant for the dynamics.

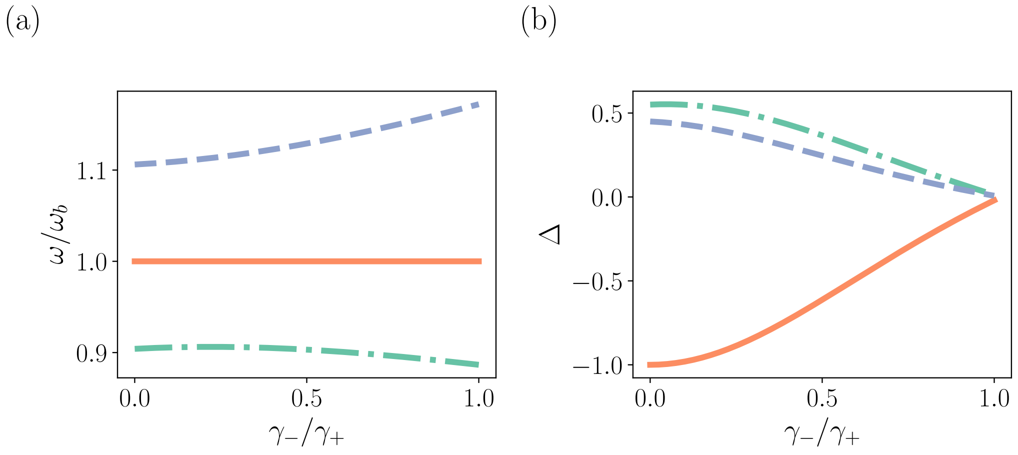

Figure 6.2.: (a) Polaritonic eigenfrequencies at resonance $\omega_+^0 = \omega_b$ for $g = 0.01$ and fixed $\gamma_+/\omega_b = 0.1$. Two branches (dashed/dotted) correspond to the lower/upper polaritons from Figure 6.1; a third branch (solid) emerges near ω_b. (b) Excess positive-handed matter content Δ. Increasing γ_- mixes opposite-handed matter, slightly enlarges the polariton splitting, and reduces Δ in the polaritons, indicating diminished chiral selectivity.

6.2.3. Imperfect Cavity with a Mixed-Handed Ensemble

We next relax the assumption of a perfectly chiral photonic environment by introducing a controlled admixture of the opposite-helicity cavity mode. Following [139], we scale the couplings of the $-$ -helicity mode by a dimensionless imperfection parameter $d \in [0, 1]$,

$$l_{-n} \;\rightarrow\; d\left(1 - g \cdot n\right), \tag{6.14}$$

so that $d = 0$ is perfectly chiral and $d = 1$ is fully achiral. Figure 6.4 shows the case of a racemic mixture, $\gamma_+ = \gamma_-$, at resonance. The four bare modes (two photonic, two matter) yield four polaritons: the highest and lowest are identifiable as the upper and lower polaritons and undergo additional splitting; the remaining two stay localized near ω_b. The excess positive-handed matter content Δ diminishes as $d \rightarrow 1$, approaching zero in the achiral limit.

Interestingly, the reduction of Δ is highly nonlinear in d and remains modest for moderate imperfections, indicating a degree of robustness of chiral selectivity to photonic asymmetry breaking. Only when d becomes large (approaching full achirality) does the selectivity drop sharply.

To disentangle molecular and photonic effects, Figure 6.5 maps the adiabatically continued upper and lower polariton branches versus both γ_-/γ_+ and d. Both parameters increase the energetic splitting while reducing Δ, but the dominant degradation of selectivity originates from the enantiomeric mixture (controlled by γ_-); photonic imperfections (d) play a secondary role except near the fully achiral limit.

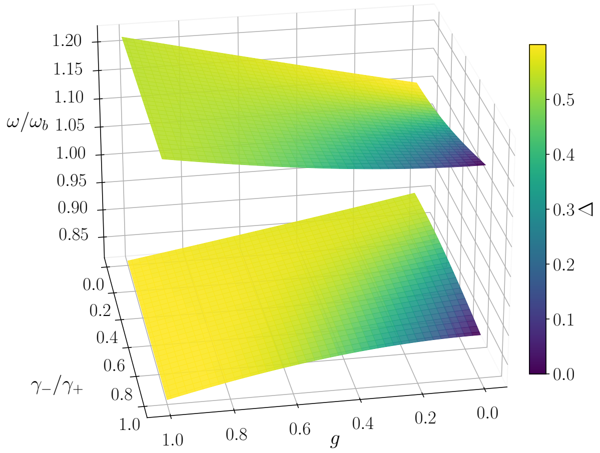

Figure 6.3.: Polaritonic eigenfrequencies, annotated by Δ, versus γ_-/γ_+ and intrinsic matter chirality g (other parameters as in Figure 6.2). Stronger g protects the excess positive-handed matter content in the polaritons. At $g = 1$, the opposite-handed matter fully decouples from the $+$ cavity mode.

6.2.4. Summary and Implications

We have shown that increasing the coupling initially enhances light-matter mixing but becomes non-monotonic in the USC/DSC regimes due to diamagnetic renormalization, akin to the well-established achiral scenario [60]. Adding opposite-handed enantiomers reduces the excess handedness content Δ even in a perfectly chiral cavity, unless intrinsic chirality is strong (large g), in which case the undesired species effectively decouples. Cavity imperfections introduce a nonlinear erosion of Δ that remains modest for intermediate d and becomes significant only near the achiral limit. Finally, enantiomeric mixture and photonic imperfection act jointly to reduce chiral selectivity, with molecular composition typically playing the dominant role. These trends might inform practical strategies for maximizing chiral discrimination in realistic devices, emphasizing control over molecular composition as the dominant optimization choice over cavity engineering.

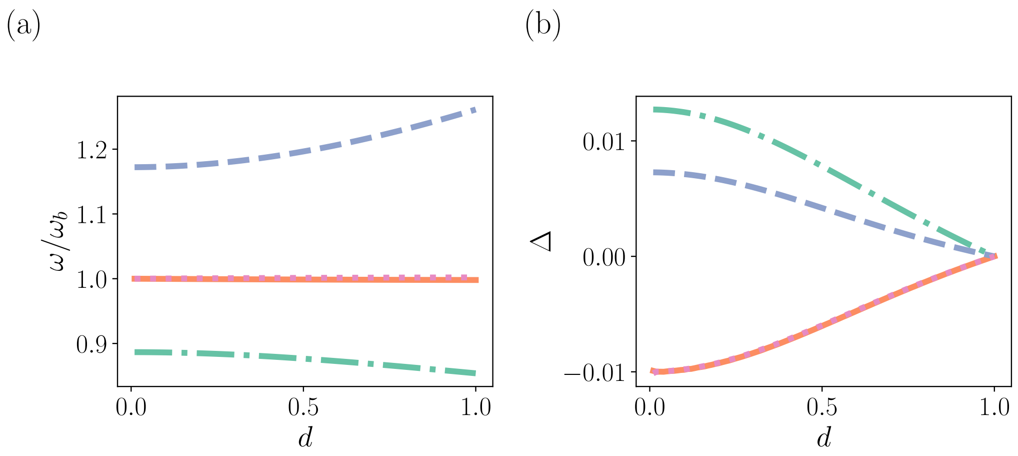

Figure 6.4.: (a) Polaritonic eigenfrequencies versus cavity imperfection d for a resonant, racemic system ($\omega_+^0 = \omega_-^0$, $\gamma_+ = \gamma_-$; other parameters as in Figure 6.2). Four polaritons emerge; the upper/lower branches split further while two modes remain near ω_b. (b) Excess positive-handed matter content Δ for the same branches. Δ decays nonlinearly with d and vanishes near the achiral limit $d = 1$.

6.3. Energy Transfer Efficiency

In the preceding section, we analyzed how enantiomeric mixtures and cavity imperfections shape polaritonic dispersion and composition, in particular the chiral selectivity $\Delta^i = C_+^i - C_-^i$ defined in Equation (6.13). We now validate and complement those insights by studying the response of the system to an external excitation and by deriving a closed, analytic expression for the energy transferred into matter modes. Our treatment uses a unitary S -matrix for a driven but otherwise closed quadratic Hamiltonian, conceptually related to input–output theory yet remaining fully Hermitian.

6.3.1. Setup and definition of efficiency

We model an external, classical field that acts as a normalized, pulsed excitation at $t = 0$

$$\phi(t) = \delta(t)\,, \tag{6.15}$$

and couples selectively to the two chiral cavity modes *via*

$$H_{\text{int}}(t) \;=\; \phi(t)\,\big(C_-\,a_- + C_+\,a_+\big) + \text{h.c.}\,, \tag{6.16}$$

where $C_\pm \in \mathbb{R}$ parameterize the electromagnetic selectivity of the excitation channel, in accordance with previous frequency-independent [138] and real coupling models [60]. In particular, $C_- = 0$ corresponds to an illumination of pure (positive) helicity (as in chiral-cavity proposals [42]). The total Hamiltonian is

$$H(t) = H_0 + H_{\text{int}}(t)\,, \tag{6.17}$$

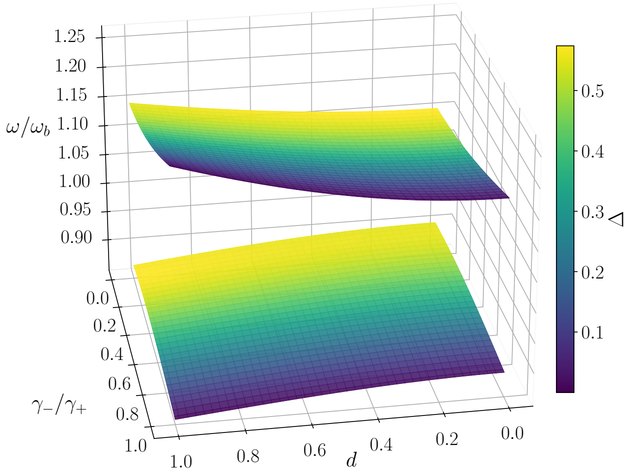

Figure 6.5.: Upper/lower polariton branches versus enantiomeric mixing (γ_-/γ_+) and cavity imperfection (d). Parameters as in Figure 6.2. Increasing either parameter enhances splitting and reduces Δ, with enantiomeric mixing exerting the dominant effect on selectivity.

with H_0 from section 6.1. We consider the incoming state to be the joint polaritonic vacuum, defined *via*

$$p_i\,|0\rangle = 0 \tag{6.18}$$

for all i. Let b_i denote the bare matter operators ($i \in \{+,-\}$ for the two handedness sectors). The energy transferred into the i -th matter mode at $t = \infty$ is

$$\Delta E_i \;=\; \omega_b\, \langle\psi_{\text{out}}|\big(b_i^I\big)^\dagger b_i^I|\psi_{\text{out}}\rangle\ , \tag{6.19}$$

where the superscript I denotes the interaction picture and

$$|\psi_{\text{out}}\rangle = S\,|0\rangle \tag{6.20}$$

is the out-state obtained by applying S. We define the *energy transfer efficiency* into mode i as the fraction of total injected energy it receives

$$\eta_i \;=\; \frac{\Delta E_i}{\sum_j \Delta E_j}\ . \tag{6.21}$$

As we will see below, η_i mirrors the qualitative content measure C_j^i in Equation (6.12): when polaritons become purely photonic or purely matter-like, the pathway for light–matter exchange narrows and η_i declines.

6.3.2. S -matrix formulation and analytic result

For a compact derivation, we write the quadratic Hamiltonian given by Equation (6.17) in Nambu form for bare bosons annihilated by c_i. We collect both light and matter operators into the vector defined in Equation (6.10) and arrive at

$$H(t) = \begin{pmatrix} \boldsymbol{c}^{\dagger,T} & \boldsymbol{c}^T \end{pmatrix} \begin{pmatrix} A & B \\ \overline{B} & \overline{A} \end{pmatrix} \begin{pmatrix} \boldsymbol{c} \\ \boldsymbol{c}^\dagger \end{pmatrix} + \begin{pmatrix} \boldsymbol{f}(t) & \overline{\boldsymbol{f}}(t) \end{pmatrix} \begin{pmatrix} \boldsymbol{c} \\ \boldsymbol{c}^\dagger \end{pmatrix}, \tag{6.22}$$

where we let Hermitian conjugation act separately on vector entries, necessetating explicit transposition in the first term, and the vector-valued classical source $\boldsymbol{f}(t)$ encodes the external potential $\phi(t)$ according to

$$\boldsymbol{f}(t) = \phi(t)\boldsymbol{C}, \tag{6.23}$$

in terms of the vector $\boldsymbol{C}$ containing the coupling coefficients defined in Equation (6.16) as follows

$$\boldsymbol{C} = \begin{pmatrix} C_+ \\ C_- \\ 0 \\ 0 \end{pmatrix}. \tag{6.24}$$

Let

$$G = \begin{pmatrix} 1_N & 0 \\ 0 & -1_N \end{pmatrix}, \quad T = \begin{pmatrix} X^\dagger & -Y^\dagger \\ -Y^T & X^T \end{pmatrix}, \quad T^{-1} = \begin{pmatrix} X & \overline{Y} \\ Y & \overline{X} \end{pmatrix}, \tag{6.25}$$

be the paraunitary transformation that diagonalizes the kernel of the unperturbed Hamiltonian H_0, which we denote by D. The matrices X and Y can then be obtained from the eigenvectors of GD [143]. In terms of polaritons p_i, the Hamiltonian is

$$H = \sum_i 2\omega_i \, p_i^\dagger p_i - i \sum_i \Big(F_i(t) p_i - \overline{F}_i(t) p_i^\dagger \Big), \tag{6.26}$$

with transformed drive $\boldsymbol{F}(t) = i\,(\boldsymbol{f}X + \overline{\boldsymbol{f}}\,Y)$. Going to the interaction picture *via* the unitary transformation

$$U(t, t_0) = e^{-iH_0(t-t_0)}, \tag{6.27}$$

yields

$$p_i^I = U^\dagger(t, t_0) p_i U(t, t_0) = p_i e^{-i2\omega_i t} \tag{6.28}$$

$$|n_i\rangle^I = |n_i\rangle \tag{6.29}$$

$$H^I_{\text{int}}(t) = -i \sum_i F_i(t)\, e^{-i2\omega_i t}\, p_i + i \sum_i \overline{F}_i(t)\, e^{i2\omega_i t}\, p_i^\dagger. \tag{6.30}$$

Denoting time ordering by $\mathcal{T}$, the S -matrix is given by

$$S \;=\; \mathcal{T}\exp\left[-i\int_{-\infty}^{\infty}\mathrm{d}t\, H^{I}_{\text{int}}(t)\right]\,. \tag{6.31}$$

An equivalent representation of the S -matrix is given by its Magnus expansion [144], for which we provide the first two terms

$$S = \exp\left[\Omega(\infty,-\infty)\right] \tag{6.32}$$

$$\Omega(t,t') = \sum_{i=1}^{\infty}\Omega_i(t,t') \tag{6.33}$$

$$\Omega_1(t,t') = -i\int_{t'}^{t}\mathrm{d}\tau H_{\text{int}}(\tau) \tag{6.34}$$

$$\Omega_2(t,t') = -\int_{t'}^{t}\mathrm{d}s\int_{t'}^{s}\mathrm{d}\tau[H_{\text{int}}(s),H_{\text{int}}(\tau))]\,. \tag{6.35}$$

The Magnus expansion closes after the second term, yielding a product of displacement operators and a phase without influence on expectation values. Suppressing this phase and using the pulsed nature of the excitation, we define

$$\phi_i \;\equiv\; \int_{-\infty}^{\infty}\mathrm{d}t\,\overline{F}_i(t)\,e^{-i2\omega_i t} = -i\sum_{\ell}C_\ell\left(\overline{X}_{\ell i}+\overline{Y}_{\ell i}\right).\,, \tag{6.36}$$

and thus arrive at $S=\prod_i D(\phi_i)$ with $D(\phi_i)=\exp(\phi_i p_i^\dagger-\overline{\phi}_i p_i)$. The out-state can thus be written as a direct product of coherent states

$$|\psi_{\text{out}}\rangle \;=\; \prod_i D(\phi_i)\,|0\rangle \;=\; \bigotimes_i|\phi_i\rangle\,. \tag{6.37}$$

According to Equation (6.19), the energy transferred into a bare mode at frequency $\tilde{\omega}_i$ is given by

$$\Delta E_i = \tilde{\omega}_i\,\langle\Psi_{\text{out}}|\left(c_i^I\right)^\dagger(t)c_i^I(t)|\Psi_{\text{out}}\rangle\;, \tag{6.38}$$

at $t=\infty$. Inserting the out-state into this expression and employing Equation (6.11) to express the bare modes in terms of polariton modes, we apply the usual causal prescription $\omega_i\to\omega_i+i0^+$ to obtain

$$\frac{\Delta E_i}{\tilde{\omega}_i} \;=\; |z_i|^2 \;+\; \sum_j Y_{ij}\,\overline{Y}_{ij}, \tag{6.39}$$

with

$$z_i \;=\; \sum_j\overline{X}_{ij}\,\phi_j \;+\; \sum_j Y_{ij}\,\overline{\phi}_j, \tag{6.40}$$

Equations (6.39)–(6.40) provide the sought analytic link between the drive selectivity $C_\pm$, the polaritonic structure (X and Y), and the energy distribution across bare mat-

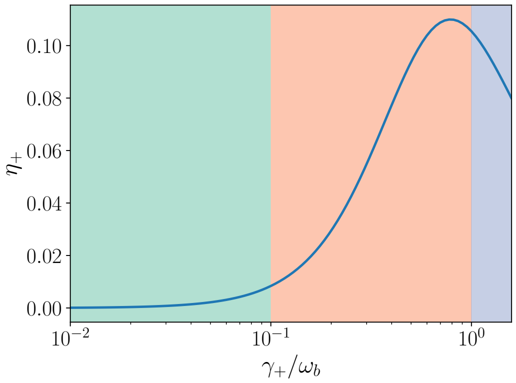

Figure 6.6.: Energy-transfer efficiency η_+ in a perfectly chiral cavity with a single $+$ helicity mode and only $+$ enantiomers (drive selectivity $C_+ = 1$, $C_- = 0$). The efficiency rises from weak to ultrastrong coupling and then decreases in the DSC regime due to diamagnetic reduction of effective coupling. Shading for RWA/USC/DSC matches Figure 6.1.

ter modes. Intuitively, ϕ_j is the drive-weighted light–matter amplitude of polariton j, z_i projects those amplitudes back onto the bare channel i.

Equation (6.21) makes explicit the qualitative link to the content measure in Equation (6.12): polaritons that are either nearly pure light or pure matter are inefficient channels for transferring energy from the optical drive into the matter sector. Maximal η_i typically occurs when the relevant polariton has a balanced admixture of the driven photonic component and the target matter component, precisely the regime where C_j^i indicates strong hybridization.

In appendix E, we extend the above discussion to a Gaussian drive.

Having completed the theoretical derivation, we now apply the expression given in Equation (6.21) to the setting of chiral cavities.

6.3.3. Energy Transfer in a Perfectly Chiral Cavity

We first revisit the single-handed setting of subsection 6.2.1 and evaluate the energy-transfer efficiency under an pulsed drive, using the S -matrix result in subsection 6.3.2. For a perfectly chiral cavity (only the $+$ helicity photonic mode present) and a single $+$ -handed enantiomeric ensemble, the energy-transfer efficiency into the $+$ matter mode,

$$\eta_+ = \frac{\Delta E_+}{\sum_j \Delta E_j},$$

is computed from Equation (6.39)–Equation (6.40). As shown in Figure 6.6, η_+ increases through the strong- and ultrastrong-coupling regimes as light–matter hybridization grows, but then *decreases* upon entering the deep-strong-coupling (DSC) regime. The decline is a direct manifestation of diamagnetic renormalization diminishing the *effective* coupling, thereby driving the relevant polariton back toward a nearly pure (photonic or matter-like) character, which is inefficient for channeling energy into the matter sector, akin to Equation (6.21) and the mode-content discussion in Equation (6.12).

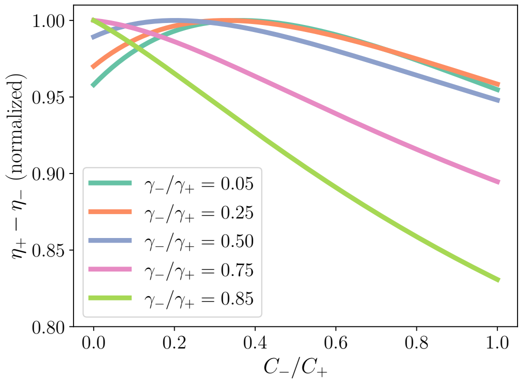

Figure 6.7.: Differential efficiency $\eta_+ - \eta_-$ vs. external coupling ratio C_-/C_+ for various enantiomer ratios γ_-/γ_+. For small γ_-/γ_+, an intermediate C_-/C_+ maximizes $\eta_+ - \eta_-$ by enabling beneficial indirect pathways; near racemization, the dependence is monotonic and decreasing.

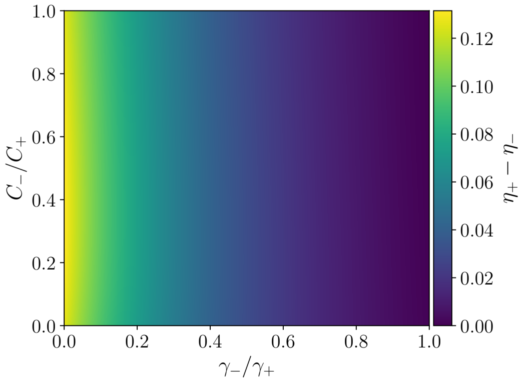

Figure 6.8.: Differential efficiency $\eta_+ - \eta_-$ over external coupling c_-/c_+ and enantiomer ratio γ_-/γ_+. A non-monotonic ridge at small γ_-/γ_+ identifies an optimal, finite C_-/C_+ that enhances selectivity in imperfect cavities; near racemization, $|\eta_+ - \eta_-|$ is suppressed across the board.

It is important to distinguish efficiency from the *absolute* deposited energy. While η_+ drops in the DSC regime, the total injected energy $\sum_j \Delta E_j$ increases monotonically with the collective coupling γ_+ (more absorbers). Thus, raising molecular concentration boosts total energy deposition but reduces the fraction reaching the target matter channel. Practically, this implies an intrinsic trade-off at very large coupling: maximizing overall absorption versus maintaining high enantioselective efficiency.

6.3.4. Energy Transfer in an Imperfect Cavity

We now consider a two-mode cavity driven by a pulsed field that can address both helicities with tunable selectivity C_-/C_+, in the presence of an enantiomeric mixture characterized by γ_-/γ_+. Using Equation (6.39)–Equation (6.40), we focus on the *differential* efficiency

$$\eta_+ - \eta_-,$$

as a measure of enantioselective energy delivery.

Figure 6.7 shows $\eta_+ - \eta_-$ versus C_-/C_+ for several values of γ_-/γ_+. For small γ_-/γ_+, the dependence is *non-monotonic*: opening a modest channel to the opposite helicity ($C_- > 0$) first *enhances* the differential efficiency, reaching a maximum at intermediate C_-/C_+, and only thereafter decreases. Physically, the added photonic pathway activates indirect hybridization routes that funnel additional energy into the target $+$ matter channel; beyond the optimum, the competing leakage dominates and $\eta_+ - \eta_-$ falls. In contrast, for larger γ_-/γ_+ (near racemization), the differential efficiency decreases monotonically with C_-/C_+. As a consistency check, a racemic mixture $\gamma_- = \gamma_+$ yields $\eta_+ - \eta_- = 0$ at $C_- = C_+$.

A broader view is provided in Figure 6.8, mapping $\eta_+ - \eta_-$ over the $(C_-/C_+, \gamma_-/\gamma_+)$ plane. The non-monotonic ridge at smaller γ_-/γ_+ confirms the existence of an optimal, finite C_-/C_+ that *improves* enantioselective transfer in imperfect cavities. Meanwhile, the dominant reduction of $|\eta_+ - \eta_-|$ across the map is driven by the enantiomeric mixture (increasing γ_-/γ_+), in line with the dispersion analysis of subsection 6.2.2.

We can thus conclude that operating in the ultrastrong-coupling window identified in subsection 6.3.3, an *imperfect* cavity can be deliberately tuned (via C_-/C_+) to *increase* differential efficiency when the admixture of opposite enantiomers is moderate (γ_-/γ_+ small). However, as γ_-/γ_+ grows, these beneficial pathways turn detrimental and the optimum disappears. Thus, system design should co-optimize intrinsic and collective molecular chirality (keeping γ_-/γ_+ low), and controlled but finite access to the opposite-helicity drive channel to exploit the intermediate-efficiency maximum.

7. Conclusion and Outlook

In this thesis, we have developed and applied a comprehensive framework for the microscopic simulation of light–matter interactions in nanoscale and quantum-optical systems, spanning from classical optoelectronics to fully quantum descriptions of chiral cavity coupling. The work combines theoretical development, software implementation, and physical applications, establishing a coherent foundation for exploring and optimizing optical phenomena in nanostructured and topological materials.

We began by formulating the theoretical principles underlying the electronic and optical properties of finite nanostructures. Starting from tight-binding and mean-field quantum models, we introduced the simulation environment `GRANAD` (*GRAphene NANoflakes with ADatoms*), a differentiable and extensible framework designed to bridge the gap between atomistic modeling and optical response theory. The formalism encompassed both time- and frequency-domain approaches to light–matter interaction, including mean-field and random-phase approximations, providing a unified basis for describing coherent and driven responses in reduced-dimensional systems.

The implementation of `GRANAD` combined a high-level Python interface for geometry and interaction definition with a high-performance numerical backend built on JAX, supporting automatic differentiation, GPU acceleration, and just-in-time compilation. This architecture enabled real-time and frequency-domain simulations of tight-binding systems with customizable Hamiltonians and interaction terms. Its differentiable design provided direct gradient access to observables, unlocking capabilities for parameter optimization, sensitivity analysis, and integration with machine-learning workflows.

Applications of `GRANAD` demonstrated its versatility across representative problems in nanoscale optoelectronics. We verified its accuracy in computing ground-state magnetization in correlated graphene nanoflakes, tracking charge conservation in time-domain simulations, and modeling vibronic polarization under mechanical perturbations. Further, simulations of Haldane-model nanoflakes revealed spin–angular-momentum–selective optical responses, showing that chiral edge currents in finite topological systems lead to polarization-dependent absorption. These findings highlight finite-size topology as a natural mechanism for spin-selective light–matter coupling and validate `GRANAD` as a robust platform for studying protected optical and transport phenomena.

Building upon this semiclassical foundation, we extended the theoretical framework to include the quantization of the electromagnetic field, developing a fully quantum description of chiral light–matter coupling in optical cavities. Within this setting, we introduced a generalized Hopfield-type Hamiltonian—termed the *chiral Hopfield model*—to capture enantiomer-specific interactions, photonic imperfections, and intrinsic molecular chirality. This model preserved gauge invariance via the inclusion of the diamagnetic A^2 term and enabled a consistent treatment across coupling regimes from weak to deep strong coupling.

Systematic analysis of the resulting polaritonic spectra revealed how chirality, enantiomeric mixtures, and cavity asymmetries shape the hybrid light–matter modes and their energy-transfer properties. For perfectly chiral cavities, the familiar strong-coupling level repulsion was recovered, followed by a reduction in effective coupling in the deep-strong regime due to diamagnetic renormalization. Introducing opposite enantiomers or cavity imperfections reduced chiral selectivity, while strongly chiral molecules ($g \gtrsim 0.5$) mitigated this loss by effectively decoupling unwanted channels. Enantiomeric mixture and photonic imperfection were found to act synergistically, amplifying each other's influence on the excess chiral content $\Delta = C_+ - C_-$.

To describe driven and open scenarios, we developed a fully Hermitian, unitary S-matrix formalism compatible with the Hopfield–Bogoliubov representation. This approach allowed a precise quantification of energy redistribution between light and matter channels under impulsive excitation. The resulting energy-transfer efficiency η_i was shown to depend on the hybrid composition of the polaritonic modes—balanced photonic–matter mixtures maximizing transfer, while purely photonic or material modes were inefficient. Increasing collective coupling enhanced energy transfer up to the onset of diamagnetic saturation, beyond which efficiency decreased. Notably, a controlled degree of counter-chiral excitation could enhance enantioselective energy transfer by opening additional hybridization pathways, revealing that small imperfections can sometimes improve performance.

Overall, the efficiency and selectivity of chiral polaritonic energy transfer were found to be constrained by the degree of enantiomeric mixing and cavity asymmetry. Optimal operation occurs in the ultrastrong-coupling regime, where hybridization is substantial but diamagnetic quenching remains moderate. These insights provide quantitative design principles for future experiments aiming to engineer enantioselective photonic environments.

The present formulation intentionally retained a Hermitian structure to isolate intrinsic chirality and coupling effects from dissipative dynamics. Future extensions will incorporate non-Hermitian elements via quantum Langevin or input–output approaches, enabling a consistent treatment of loss, decoherence, and noise. Including these effects will be crucial for connecting theoretical predictions to measured observables such as linewidths and absorption spectra in realistic molecular and plasmonic systems.

Beyond this, a promising avenue lies in *ab initio* quantum electrodynamics, where electronic structure and cavity modes are treated on equal footing. Such methods could parameterize effective Hopfield Hamiltonians directly from microscopic dipoles and magnetic moments, bridging quantum chemistry and polaritonic device design. Extensions to multimode and dissipative environments would further allow the study of chiral polaritonic transport, cooperative emission, and enantioselective catalysis under strong coupling.

References

[P1] D. Dams and C. Rockstuhl, “Enantiomer selectivity and energy transfer in imperfect chiral cavities”, Physical Review A **112**, 033707 (2025).

[P2] M. Pelc, D. Dams, A. Ghosh, M. Kosik, M. M. Müller, G. Bryant, C. Rockstuhl, A. Ayuela, and K. Słowik, “Single-particle approach to many-body relaxation dynamics”, Physical Review A **109** (2024).

[P3] D. Dams and C. Rockstuhl, “Optical spin angular momentum sensitivity of topological nanoflakes”, Physical Review B **111**, 235147 (2025).

[P4] D. Dams, M. Kosik, M. Müller, A. Ghosh, A. Babaze, J. Szczuczko, G. W. Bryant, A. Ayuela, C. Rockstuhl, M. Pelc, and K. Słowik, “Granad - simulating graphene nanoflakes with adatoms”, Computer Physics Communications **317**, 109818 (2025).

[1] M. Rahmani and C. Jagadish, “Light–matter interactions on the nanoscale”, Beilstein Journal of Nanotechnology **9**, 2125–2127 (2018).

[2] F. H. L. Koppens, D. E. Chang, and F. J. García de Abajo, “Graphene plasmonics: a platform for strong light–matter interactions”, Nano Letters **11**, 3370–3377 (2011).

[3] J. D. Caldwell, A. V. Kretinin, Y. Chen, and et al., “Sub-diffractional volume-confined polaritons in the natural hyperbolic material hexagonal boron nitride”, Nature Communications **5**, 5221 (2014).

[4] K. F. Mak and J. Shan, “Photonics and optoelectronics of 2d semiconductor transition metal dichalcogenides”, Nature Photonics **10**, 216–226 (2016).

[5] G. Eda and S. A. Maier, “Two-dimensional crystals: managing light for optoelectronics”, ACS Nano **7**, 5660–5665 (2013).

[6] J. Christensen, A. Manjavacas, S. Thongrattanasiri, F. H. L. Koppens, and F. J. García de Abajo, “Graphene plasmon waveguiding and hybridization in individual and paired nanoribbons”, ACS Nano **6**, 431–440 (2012).

[7] G. Wang, A. Chernikov, M. M. Glazov, T. F. Heinz, X. Marie, T. Amand, and B. Urbaszek, “Colloquium: excitons in atomically thin transition metal dichalcogenides”, Rev. Mod. Phys. **90**, 021001 (2018).

[8] A. K. Geim and I. V. Grigorieva, “Van der waals heterostructures”, Nature **499**, 419–425 (2013).

[9] S. Latini, E. Ronca, U. De Giovannini, H. Hübener, and A. Rubio, “Cavity control of excitons in two-dimensional materials”, Nano Letters **19**, 3473–3479 (2019).

[10] F. D. M. Haldane, “Model for a quantum hall effect without landau levels: condensed-matter realization of the "parity anomaly"”, Physical Review Letters **61**, 2015–2018 (1988).

[11] N. Hao, P. Zhang, Z. Wang, W. Zhang, and Y. Wang, “Topological edge states and quantum hall effect in the haldane model”, Physical Review B **78**, 075438 (2008).

[12] K. Kondo and R. Ito, “Quantum spin hall phase in honeycomb nanoribbons with two different atoms: edge shape effect to bulk-edge correspondence”, Journal of Physics Communications **3**, 055007 (2019).

[13] G. Jotzu, M. Messer, R. Desbuquois, M. Lebrat, T. Uehlinger, D. Greif, and T. Esslinger, “Experimental realization of the topological haldane model with ultracold fermions”, Nature **515**, 237–240 (2014).

[14] H. S. Kim and H.-Y. Kee, “Realizing haldane model in fe-based honeycomb ferromagnetic insulators”, npj Quantum Materials **2**, 20 (2017).

[15] W. Zhao, K. Kang, Y. Zhang, P. Knüppel, Z. Tao, L. Li, C. L. Tschirhart, E. Redekop, K. Watanabe, T. Taniguchi, A. F. Young, J. Shan, and K. F. Mak, “Realization of the haldane chern insulator in a moiré lattice”, Nature Physics **20**, 275–280 (2024).

[16] S. K. Kim, H. Ochoa, R. Zarzuela, and Y. Tserkovnyak, “Realization of the haldane-kane-mele model in a system of localized spins”, Physical Review Letters **117**, 227201 (2016).

[17] M. Shah, M. S. Anwar, R. Asgari, and G. Xianlong, “Photonic spin hall effect in haldane model materials”, Physical Review B **109**, 235418 (2024).

[18] R. W. Nunes and D. Vanderbilt, “Real-space approach to calculation of electric polarization and dielectric constants”, Physical Review Letters **73**, 712–715 (1994).

[19] D. Vanderbilt, *Berry phases in electronic structure theory: electric polarization, orbital magnetization and topological insulators* (Cambridge University Press, 2018).

[20] S. Thongrattanasiri, A. Manjavacas, and F. J. García de Abajo, “Quantum finite-size effects in graphene plasmons”, ACS Nano **6**, 1766–1775 (2012).

[21] G. Kresse and J. Furthmüller, “Efficient iterative schemes for ab initio total-energy calculations using a plane-wave basis set”, Physical Review B **54**, 11169–11186 (1996).

[22] J. M. Soler, E. Artacho, J. D. Gale, A. García, J. Junquera, P. Ordejón, and D. Sánchez-Portal, “The siesta method for ab initio order-n materials simulation”, Journal of Physics: Condensed Matter **14**, 2745 (2002).

[23] P. Giannozzi, O. Andreussi, T. Brumme, O. Bunau, M. Buongiorno Nardelli, M. Calandra, R. Car, C. Cavazzoni, D. Ceresoli, M. Cococcioni, N. Colonna, I. Carnimeo, A. Dal Corso, S. de Gironcoli, P. Delugas, R. A. DiStasio, A. Ferretti, A. Floris, G. Fratesi, G. Fugallo, R. Gebauer, U. Gerstmann, F. Giustino, T. Gorni, J. Jia, M. Kawamura, H.-Y. Ko, A. Kokalj, E. Küçükbenli, M. Lazzeri, M. Marsili, N. Marzari, F. Mauri, N. L. Nguyen, H.-V. Nguyen, A. Otero-de-la-Roza, L. Paulatto, S. Poncé, D. Rocca, R. Sabatini, B. Santra, M. Schlipf, A. P. Seitsonen, A. Smogunov, I. Timrov, T. Thonhauser, P. Umari, N. Vast, X. Wu, and S. Baroni, “Advanced capabilities for materials modelling with quantum espresso”, Journal of Physics: Condensed Matter **29**, 465901 (2017).

[24] Y. J. Franzke, C. Holzer, J. H. Andersen, T. Begušić, F. Bruder, S. Coriani, F. Della Sala, E. Fabiano, D. A. Fedotov, S. Fürst, S. Gillhuber, R. Grotjahn, M. Kaupp, M. Kehry, M. Krstić, F. Mack, S. Majumdar, B. D. Nguyen, S. M. Parker, F. Pauly, A. Pausch, E. Perlt, G. S. Phun, A. Rajabi, D. Rappoport, B. Samal, T. Schrader, M. Sharma, E. Tapavicza, R. S. Treß, V. Voora, A. Wodyński, J. M. Yu, B. Zerulla, F. Furche, C. Hättig, M. Sierka, D. P. Tew, and F. Weigend, "Turbomole: today and tomorrow", Journal of Chemical Theory and Computation **19**, 6859–6890 (2023).

[25] B. Hourahine, B. Aradi, V. Blum, F. Bonafé, A. Buccheri, C. Camacho, C. Cevallos, M. Y. Deshaye, T. Dumitrică, A. Dominguez, S. Ehlert, M. Elstner, T. van der Heide, J. Hermann, S. Irle, J. J. Kranz, C. Köhler, T. Kowalczyk, T. Kubař, I. S. Lee, V. Lutsker, R. J. Maurer, S. K. Min, I. Mitchell, C. Negre, T. A. Niehaus, A. M. N. Niklasson, A. J. Page, A. Pecchia, G. Penazzi, M. P. Persson, J. Řezáč, C. G. Sánchez, M. Sternberg, M. Stöhr, F. Stuckenberg, A. Tkatchenko, V. W.-z. Yu, and T. Frauenheim, "Dftb+, a software package for efficient approximate density functional theory based atomistic simulations", The Journal of Chemical Physics **152**, 124101 (2020).

[26] R. Hu, Q.-D. Ho, Q. To, G. Bryant, and A. Janotti, "Density-functional Tight-binding Method for Simulation of Rare-earth Mono-pnictide (RE-V):III-V", in Aps march meeting abstracts, Vol. 2022, APS Meeting Abstracts (Mar. 2022), A66.005.

[27] C. W. Groth, M. Wimmer, A. R. Akhmerov, and X. Waintal, "Kwant: a software package for quantum transport", New Journal of Physics **16**, 063065 (2014).

[28] S. M. João, M. Anđelković, L. Covaci, T. G. Rappoport, J. M. V. P. Lopes, and A. Ferreira, "KITE: high-performance accurate modelling of electronic structure and response functions of large molecules, disordered crystals and heterostructures", **7**, 191809 (2020).

[29] S. Coh and D. Vanderbilt, *Python tight binding (pythtb)*, Sept. 2022.

[30] D. Moldovan, M. Anđelković, and F. Peeters, *Pybinding v0.9.5: a python package for tight- binding calculations*, version v0.9.5, Aug. 2020.

[31] G. Van Rossum and F. L. Drake Jr, *Python tutorial* (Centrum voor Wiskunde en Informatica Amsterdam, The Netherlands, 1995).

[32] C. R. Harris, K. J. Millman, S. J. van der Walt, R. Gommers, P. Virtanen, D. Cournapeau, E. Wieser, J. Taylor, S. Berg, N. J. Smith, R. Kern, M. Picus, S. Hoyer, M. H. van Kerkwijk, M. Brett, A. Haldane, J. F. del Río, M. Wiebe, P. Peterson, P. Gérard-Marchant, K. Sheppard, T. Reddy, W. Weckesser, H. Abbasi, C. Gohlke, and T. E. Oliphant, "Array programming with NumPy", Nature **585**, 357–362 (2020).

[33] P. Virtanen, R. Gommers, T. E. Oliphant, M. Haberland, T. Reddy, D. Cournapeau, E. Burovski, P. Peterson, W. Weckesser, J. Bright, S. J. van der Walt, M. Brett, J. Wilson, K. J. Millman, N. Mayorov, A. R. J. Nelson, E. Jones, R. Kern, E. Larson, C. J. Carey, İ. Polat, Y. Feng, E. W. Moore, J. VanderPlas, D. Laxalde, J. Perktold, R. Cimrman, I. Henriksen, E. A. Quintero, C. R. Harris, A. M. Archibald, A. H. Ribeiro,

F. Pedregosa, P. van Mulbregt, and SciPy 1.0 Contributors, “SciPy 1.0: Fundamental Algorithms for Scientific Computing in Python”, Nature Methods **17**, 261–272 (2020).

[34] L. D. Barron, *Molecular light scattering and optical activity* (Cambridge University Press, 2009).

[35] J. Gal, “Molecular chirality in chemistry and biology: historical milestones”, Helvetica Chimica Acta **96**, 1617–1657 (2013).

[36] M. Quack, “Structure and dynamics of chiral molecules”, Angewandte Chemie International Edition in English **28**, 571–586 (1989).

[37] E. Sanganyado, Z. Lu, Q. Fu, D. Schlenk, and J. Gan, “Chiral pharmaceuticals: a review on their environmental occurrence and fate processes”, Water Research **124**, 527–542 (2017).

[38] C. Schäfer and D. G. Baranov, “Chiral polaritonics: analytical solutions, intuition, and use”, The Journal of Physical Chemistry Letters **14**, 3777–3784 (2023).

[39] R. R. Riso, L. Grazioli, E. Ronca, T. Giovannini, and H. Koch, “Strong coupling in chiral cavities: nonperturbative framework for enantiomer discrimination”, Physical Review X **13**, 031002 (2023).

[40] C. Schäfer, M. Ruggenthaler, and A. Rubio, “Ab initio nonrelativistic quantum electrodynamics: bridging quantum chemistry and quantum optics from weak to strong coupling”, Physical Review A **98**, 043801 (2018).

[41] H. Hübener, U. D. Giovannini, C. Schäfer, et al., “Engineering quantum materials with chiral optical cavities”, Nature Materials **20**, 438–442 (2021).

[42] K. Voronin, A. S. Taradin, M. V. Gorkunov, and D. G. Baranov, “Single-handedness chiral optical cavities”, ACS Photonics **9**, 2652–2659 (2022).

[43] Y.-H. Kang, Z.-C. Shi, J. Song, and Y. Xia, “Effective discrimination of chiral molecules in a cavity”, Optics Letters **45**, 4952–4955 (2020).

[44] N. S. Baßler, A. Aiello, K. P. Schmidt, C. Genes, and M. Reitz, “Metasurface-based hybrid optical cavities for chiral sensing”, Physical Review Letters **132**, 043602 (2024).

[45] A. H. Salij, R. H. Goldsmith, and R. Tempelaar, “Theory predicts 2d chiral polaritons based on achiral fabry–pérot cavities using apparent circular dichroism”, Nature Communications **15**, 340 (2024).

[46] D. G. Baranov, C. Schäfer, and M. V. Gorkunov, “Toward molecular chiral polaritons”, ACS Photonics **10**, 2440–2455 (2023).

[47] G. Fedorovich, D. Kornovan, A. Poddubny, and M. Petrov, “Chirality-driven delocalization in disordered waveguide-coupled quantum arrays”, Physical Review A **106**, 043723 (2022).

[48] D. G. Suárez-Forero, R. Ni, S. Sarkar, M. J. Mehrabad, E. Mechtel, V. Simonyan, A. Grankin, K. Watanabe, T. Taniguchi, S. Park, H. Jang, M. Hafezi, and Y. Zhou, “Chiral flat-band optical cavity with atomically thin mirrors”, Science Advances **10**, eadr5904 (2024).

[49] S. Yoo and Q.-H. Park, Nanophotonics **8**, 249–261 (2019).

[50] J. Rosinski, M. Gawełczyk, K. Tarnowski, P. Karwat, D. Wigger, and P. Machnikowski, “Quantum dots as optimized chiral emitters for photonic integrated circuits”, Physical Review B **109**, 085431 (2024).

[51] V. M. Axt, P. Machnikowski, and T. Kuhn, “Reducing decoherence of the confined exciton state in a quantum dot by pulse-sequence control”, Physical Review B **71**, 155305 (2005).

[52] R. R. Riso, E. Ronca, and H. Koch, “Strong coupling to circularly polarized photons: toward cavity-induced enantioselectivity”, The Journal of Physical Chemistry Letters **15**, 8838–8844 (2024).

[53] X. Zhong, T. Chervy, L. Zhang, A. Thomas, J. George, C. Genet, J. A. Hutchison, and T. W. Ebbesen, “Energy transfer between spatially separated entangled molecules”, Angewandte Chemie International Edition **56**, 9034–9038 (2017).

[54] D. Coles, N. Somaschi, P. Michetti, et al., “Polariton-mediated energy transfer between organic dyes in a strongly coupled optical microcavity”, Nature Materials **13**, 712–719 (2014).

[55] J. Singh, J. Lather, and J. George, “Solvent dependence on cooperative vibrational strong coupling and cavity catalysis”, ChemPhysChem **24**, e202300016 (2023).

[56] M. V. Imperatore, J. B. Asbury, and N. C. Giebink, “Reproducibility of cavity-enhanced chemical reaction rates in the vibrational strong coupling regime”, The Journal of Chemical Physics **154**, 191103 (2021).

[57] J. A. Hutchison, T. Schwartz, C. Genet, E. Devaux, and T. W. Ebbesen, “Modifying chemical landscapes by coupling to vacuum fields”, Angewandte Chemie International Edition **51**, 1592–1596 (2012).

[58] D. F. Kornovan, M. I. Petrov, and I. V. Iorsh, “Transport and collective radiance in a basic quantum chiral optical model”, Physical Review B **96**, 115162 (2017).

[59] J. S. Peter, S. Ostermann, and S. F. Yelin, “Chirality dependent photon transport and helical superradiance”, Physical Review Research **6**, 023200 (2024).

[60] S. De Liberato, “Light-matter decoupling in the deep strong coupling regime: the breakdown of the purcell effect”, Physical Review Letters **112**, 016401 (2014).

[61] P. Nataf and C. Ciuti, “No-go theorem for superradiant quantum phase transitions in cavity qed and counter-example in circuit qed”, Nature Communications **1**, 72 (2010).

[62] M. Kosik, M. M. Müller, K. Słowik, G. Bryant, A. Ayuela, C. Rockstuhl, and M. Pelc, “Revising quantum optical phenomena in adatoms coupled to graphene nanoantennas”, Nanophotonics **11**, 3281–3298 (2022).

[63] A. Altland and B. D. Simons, *Condensed matter field theory* (Cambridge university press, 2010).

[64] M. Schüler, J. A. Marks, Y. Murakami, C. Jia, and T. P. Devereaux, "Gauge invariance of light-matter interactions in first-principle tight-binding models", Phys. Rev. B **103**, 155409 (2021).

[65] M. Kira and S. W. Koch, *Semiconductor quantum optics*, 2011.

[66] C.-C. Lee, Y.-T. Lee, M. Fukuda, and T. Ozaki, "Tight-binding calculations of optical matrix elements for conductivity using nonorthogonal atomic orbitals: anomalous hall conductivity in bcc fe", Phys. Rev. B **98**, 115115 (2018).

[67] P. Giannozzi, O. Andreussi, T. Brumme, O. Bunau, M. Buongiorno Nardelli, M. Calandra, R. Car, C. Cavazzoni, D. Ceresoli, M. Cococcioni, N. Colonna, I. Carnimeo, A. Dal Corso, S. de Gironcoli, P. Delugas, R. A. DiStasio, A. Ferretti, A. Floris, G. Fratesi, G. Fugallo, R. Gebauer, U. Gerstmann, F. Giustino, T. Gorni, J. Jia, M. Kawamura, H.-Y. Ko, A. Kokalj, E. Küçükbenli, M. Lazzeri, M. Marsili, N. Marzari, F. Mauri, N. L. Nguyen, H.-V. Nguyen, A. Otero-de-la-Roza, L. Paulatto, S. Poncé, D. Rocca, R. Sabatini, B. Santra, M. Schlipf, A. P. Seitsonen, A. Smogunov, I. Timrov, T. Thonhauser, P. Umari, N. Vast, X. Wu, and S. Baroni, "Advanced capabilities for materials modelling with quantum espresso", Journal of Physics: Condensed Matter **29**, 465901 (2017).

[68] "Quantum Materials: Experiments and Theory", Schriften des Forschungszentrums Jülich. Reihe modeling and simulation **6**, edited by E. Pavarini, E. Koch, J. van den Brink, and G. Sawatzky, 420 S. (2016).

[69] F. Furche, "On the density matrix based approach to time-dependent density functional response theory", The Journal of Chemical Physics **114**, 5982–5992 (2001).

[70] D. Tománek and S. G. Louie, "First-principles calculation of highly asymmetric structure in scanning-tunneling-microscopy images of graphite", Physical Review B **37**, 8327–8336 (1988).

[71] J. C. Slater and G. F. Koster, "Simplified lcao method for the periodic potential problem", Physical Review **94**, 1498–1524 (1954).

[72] T. Stauber, N. M. R. Peres, and A. K. Geim, "Optical conductivity of graphene in the visible region of the spectrum", Physical Review B **78** (2008).

[73] J. M. Link, P. P. Orth, D. E. Sheehy, and J. Schmalian, "Universal collisionless transport of graphene", Physical Review B **93** (2016).

[74] M. M. Müller, M. Kosik, M. Pelc, G. W. Bryant, A. Ayuela, C. Rockstuhl, and K. Słowik, "From single-particle-like to interaction-mediated plasmonic resonances in graphene nanoantennas", Journal of Applied Physics **129**, 093103 (2021).

[75] C. L. Lu, C. P. Chang, Y. C. Huang, R. B. Chen, and M. L. Lin, "Influence of an electric field on the optical properties of few-layer graphene with ab stacking", Phys. Rev. B **73**, 144427 (2006).

[76] J. Bradbury, R. Frostig, P. Hawkins, M. J. Johnson, C. Leary, D. Maclaurin, G. Necula, A. Paszke, J. VanderPlas, S. Wanderman-Milne, and Q. Zhang, *JAX: composable transformations of Python+NumPy programs*, version 0.3.13, 2018.

[77] T. G. Pedersen, K. Pedersen, and T. Brun Kriestensen, “Optical matrix elements in tight-binding calculations”, Physical Review B **63** (2001).

[78] D. Sangalli, J. A. Berger, C. Attaccalite, M. Grüning, and P. Romaniello, “Optical properties of periodic systems within the current-current response framework: pitfalls and remedies”, Physical Review B **95** (2017).

[79] S. Traverso, M. Sassetti, and N. Traverso Ziani, “Emerging topological bound states in haldane model zigzag nanoribbons”, npj Quantum Materials **9**, 9 (2024).

[80] F. Calleja, H. Ochoa, M. Garnica, S. Barja, J. J. Navarro, A. Black, M. M. Otrokov, E. V. Chulkov, Y. H. W. Son, G. Pratzer, T. F. R. Raschke, A. L. V. de Parga, R. Miranda, D. Jacob, T. R. Pollak, D. G. de Oteyza, D. Saúl, and A. Schiffrin, “Spatial variation of a giant spin–orbit effect induces electron confinement in graphene on pb islands”, Nature Physics **11**, 43–47 (2015).

[81] F. Schwabl, *Statistische mechanik* (Springer, 2006).

[82] G. Giuliani and G. Vignale, *Quantum theory of the electron liquid* (Cambridge university press, 2008).

[83] J. D. Cox and F. Javier García de Abajo, “Electrically tunable nonlinear plasmonics in graphene nanoislands”, Nature Communications **5** (2014).

[84] R. Yu, J. D. Cox, J. R. M. Saavedra, and F. J. García de Abajo, “Analytical modeling of graphene plasmons”, ACS Photonics **4**, 3106–3114 (2017).

[85] J. Zhang, L. Zhang, and W. Xu, “Surface plasmon polaritons: physics and applications”, Journal of Physics D: Applied Physics **45**, 113001 (2012).

[86] P. Nataf and C. Ciuti, “No-go theorem for superradiant quantum phase transitions in cavity qed and counter-example in circuit qed”, Nature Communications **1** (2010).

[87] S. Wang, “Generalization of the thomas-reiche-kuhn and the bethe sum rules”, Phys. Rev. A **60**, 262–266 (1999).

[88] G. Czycholl, *Theoretische festkörperphysik: von den klassischen modellen zu modernen forschungsthemen* (Springer, 2008).

[89] P. Potasz, A. D. Güçlü, A. Wójs, and P. Hawrylak, “Electronic properties of gated triangular graphene quantum dots: magnetism, correlations, and geometrical effects”, Physical Review B **85** (2012).

[90] A. Szabo and N. S. Ostlund, *Modern quantum chemistry: introduction to advanced electronic structure theory*, First (Dover Publications, Inc., Mineola, 1996).

[91] “The Physics of Correlated Insulators, Metals, and Superconductors”, Schriften des Forschungszentrums Jülich. Reihe Modeling and Simulation **7**, edited by E. Pavarini, E. Koch, R. Scalettar, and R. Martin, 450 S. (2017).

[92] O. Dmytruk and M. Schirò, “Controlling topological phases of matter with quantum light”, Communications Physics **5** (2022).

[93] *Dynamical Mean-Field Theory of Correlated Electrons*, Vol. 12, Modeling and Simulation, Autumn School on Correlated Electrons, Jülich (Germany), 4 Oct 2022 - 7 Oct 2022 (Forschungszentrum Jülich GmbH Zentralbibliothek, Verlag, Jülich, Oct. 4, 2022).

[94] C. J. Halboth and W. Metzner, “Renormalization-group analysis of the two-dimensional hubbard model”, Physical Review B **61**, 7364–7377 (2000).

[95] F. H. L. Essler, H. Frahm, F. Göhmann, A. Klümper, and V. E. Korepin, “The hubbard hamiltonian and its symmetries”, in *The one-dimensional hubbard model* (Cambridge University Press, 2005), pp. 20–49.

[96] M. M. Müller, “Electronic and photonic excitations in graphene nanostructures and hybrid systems”, 43.31.02; LK 01, PhD thesis (Karlsruher Institut für Technologie (KIT), 2022), 143 pp.

[97] M. Kosik, “Tight-binding framework to study optical properties of graphene nanoantennas with adatoms”, Doctor of Philosophy dissertation, PhD thesis (Nicolaus Copernicus University, Faculty of Physics, Astronomy and Informatics, Jan. 2023).

[98] M. M. Müller, M. Kosik, M. Pelc, G. W. Bryant, A. Ayuela, C. Rockstuhl, and K. Słowik, “Energy-based plasmonicity index to characterize optical resonances in nanostructures”, The Journal of Physical Chemistry C **124**, 24331–24343 (2020).

[99] F. Watson, M. G. Crabb, and W. R. Lionheart, “A polarization tensor approximation for the hessian in iterative solvers for non-linear inverse problems”, Inverse Problems in Science and Engineering **29**, 2804–2830 (2021).

[100] S. Lindenthal, D. Fazzi, N. F. Zorn, A. A. El Yumin, S. Settele, B. Weidinger, E. Blasco, and J. Zaumseil, “Understanding the optical properties of doped and undoped 9-armchair graphene nanoribbons in dispersion”, ACS Nano **17**, 18240–18252 (2023).

[101] J. Fernández-Rossier and J. J. Palacios, “Magnetism in graphene nanoislands”, Phys. Rev. Lett. **99**, 177204 (2007).

[102] E. H. Lieb, “Two theorems on the hubbard model”, Physical Review Letters **62**, 1201–1204 (1989).

[103] N. Ma and M. S. Reis, “Anomalous acoustic phonons as the physical mechanism behind the adiabatic barocaloric effect on graphene”, Scientific Reports **9**, 219 (2019).

[104] A. R. Botello-Méndez, J. C. Obeso-Jureidini, and G. G. Naumis, “Toward an accurate tight-binding model of graphene’s electronic properties under strain”, The Journal of Physical Chemistry C **122**, 15753–15760 (2018).

[105] Z. Dong, F. Yang, and J. S. Ho, “Enhanced electromagnetic energy harvesting with subwavelength chiral structures”, Physical Review Applied **8**, 044026 (2017).

[106] G. K. E. Scriba, “Chiral electromigration techniques in pharmaceutical and biomedical analysis”, Bioanalytical Reviews **3**, 95–114 (2011).

[107] S. Parkin, G. Knüner, T. A. Nieminen, N. R. Heckenberg, and H. Rubinsztein-Dunlop, “Measurement of the total optical angular momentum transfer in optical tweezers”, Opt. Express **14**, 6963–6970 (2006).

[108] A. Qu, L. Xu, C. Xu, and H. Kuang, “Chiral nanomaterials for biosensing, bioimaging, and disease therapies”, Chem. Commun. **58**, 12782–12802 (2022).

[109] A. Schimmoller, S. Walker, and A. S. Landsman, “Photonic angular momentum in intense light–matter interactions”, Photonics **11**, 871 (2024).

[110] A. B. Khanikaev and A. Alù, “Topological photonics: robustness and beyond”, Nature Communications **15**, 931 (2024).

[111] J. D. Cox, M. R. Singh, G. Gumbs, M. A. Anton, and F. Carreno, “Dipole-dipole interaction between a quantum dot and a graphene nanodisk”, Physical Review B **86**, 125452 (2012).

[112] A. Babaze, E. Ogando, P. E. Stamatopoulou, C. Tserkezis, N. A. Mortensen, J. Aizpurua, A. G. Borisov, and R. Esteban, “Quantum surface effects in the electromagnetic coupling between a quantum emitter and a plasmonic nanoantenna: time-dependent density functional theory vs. semiclassical feibelman approach”, Opt. Express **30**, 21159–21183 (2022).

[113] O. Dmytruk and M. Schirò, “Controlling topological phases of matter with quantum light”, Communications Physics **5**, 271 (2022).

[114] Y. Guan, Z. Jiang, and S. Haas, “Control of plasmons in topological insulators via local perturbations”, Physical Review B **104**, 125425 (2021).

[115] L. Ge, T. Zhan, D. Han, X. Liu, and J. Zi, “Unusual electromagnetic scattering by cylinders of topological insulator”, Optics Express **22**, 30833–30842 (2014).

[116] S. Mitra, Á. Jiménez-Galán, M. Aulich, M. Neuhaus, R. E. F. Silva, V. Pervak, M. F. Kling, and S. Biswas, “Light-wave-controlled haldane model in monolayer hexagonal boron nitride”, Nature **628**, 752–757 (2024).

[117] P. Mai, B. E. Feldman, and P. W. Phillips, “Topological mott insulator at quarter filling in the interacting haldane model”, Physical Review Res. **5**, 013162 (2023).

[118] J. Li, S. Sanz, N. Merino-Díez, M. Vilas-Varela, A. Garcia-Lekue, M. Corso, D. G. de Oteyza, T. Frederiksen, D. Peña, and J. I. Pascual, “Topological phase transition in chiral graphene nanoribbons: from edge bands to end states”, Nature Communications **12**, 5538 (2021).

[119] V. Peano, M. Houde, C. Brendel, F. Marquardt, and A. A. Clerk, “Topological phase transitions and chiral inelastic transport induced by the squeezing of light”, Nature Communications **7**, 10779 (2016).

[120] C. Cohen-Tannoudji, J. Dupont-Roc, and G. Grynberg, *Photons and atoms: introduction to quantum electrodynamics* (Wiley-VCH, 1997) Chap. 1.

[121] I. Fernandez-Corbaton, X. Zambrana-Puyalto, and G. Molina-Terriza, “Helicity and angular momentum: a symmetry-based framework for the study of light-matter interactions”, Physical Review A **86**, 042103 (2012).

[122] H. Jürß and D. Bauer, “Topological edge-state contributions to high-order harmonic generation in finite flakes”, Physical Review B **106**, 054303 (2022).

[123] I. Fernandez-Corbaton, M. Fruhnert, and C. Rockstuhl, “Objects of maximum electromagnetic chirality”, Physical Review X **6**, 031013 (2016).

[124] W. Li, F. P. Sabino, F. Crasto de Lima, T. Wang, R. H. Miwa, and A. Janotti, “Large disparity between optical and fundamental band gaps in layered $\mathrm{In_2Se_3}$”, Phys. Rev. B **98**, 165134 (2018).

[125] A. Schleife, J. B. Varley, F. Fuchs, C. Rödl, F. Bechstedt, P. Rinke, A. Janotti, and C. G. Van de Walle, “Tin dioxide from first principles: quasiparticle electronic states and optical properties”, Phys. Rev. B **83**, 035116 (2011).

[126] T. Stauber, T. Low, and G. Gómez-Santos, “Chiral response of twisted bilayer graphene”, Physical Review Letters **120**, 046801 (2018).

[127] H. Schlömer, Z. Jiang, and S. Haas, “Plasmons in two-dimensional topological insulators”, Physical Review B **103**, 115116 (2021).

[128] T.-C. Yi, S. Hu, E. V. Castro, and R. Mondaini, “Interplay of interactions, disorder, and topology in the haldane-hubbard model”, Physical Review B **104**, 195117 (2021).

[129] F. Aguillon, D. C. Marinica, and A. G. Borisov, “Plasmons in graphene nanostructures with point defects and impurities”, The Journal of Physical Chemistry C **125**, 21503–21510 (2021).

[130] J. Li, D. Golez, G. Mazza, A. J. Millis, A. Georges, and M. Eckstein, “Electromagnetic coupling in tight-binding models for strongly correlated light and matter”, Physical Review B **101** (2020).

[131] G. M. Andolina, F. M. D. Pellegrino, V. Giovannetti, A. H. MacDonald, and M. Polini, “Cavity quantum electrodynamics of strongly correlated electron systems: a no-go theorem for photon condensation”, Physical Review B **100** (2019).

[132] O. Dmytruk and M. Schiró, “Gauge fixing for strongly correlated electrons coupled to quantum light”, Physical Review B **103**, 075131 (2021).

[133] R. G. Woolley, “Power-zienau-woolley representations of nonrelativistic qed for atoms and molecules”, Physical Review Research **2**, 013206 (2020).

[134] D. L. Andrews, G. A. Jones, A. Salam, and R. G. Woolley, “Perspective: quantum hamiltonians for optical interactions”, The Journal of Chemical Physics **148**, 040901 (2018).

[135] S. Savasta, O. Di Stefano, A. Settineri, D. Zueco, S. Hughes, and F. Nori, “Gauge principle and gauge invariance in two-level systems”, Physical Review A **103**, 053703 (2021).

[136] K. Rzażewski, K. Wódkiewicz, and W. Żakowicz, “Phase transitions, two-level atoms, and the A^2 term”, Physical Review Letters **35**, 432–434 (1975).

[137] P. Kirton, M. M. Roses, J. Keeling, and E. G. Dalla Torre, “Introduction to the dicke model: from equilibrium to nonequilibrium, and vice versa”, Advanced Quantum Technologies **2**, 1800043 (2019).

[138] C. Ciuti and I. Carusotto, “Input-output theory of cavities in the ultrastrong coupling regime: the case of time-independent cavity parameters”, Physical Review A **74**, 033811 (2006).

[139] L. M. Tomasch, F. Spallek, G. W. Fuchs, T. F. Giesen, and S. Y. Buhmann, “Strong coupling of a chiral molecule with circularly polarised modes inside a cavity”, arXiv preprint arXiv:2412.18700 (2024).

[140] G. M. Andolina, F. M. D. Pellegrino, V. Giovannetti, A. H. MacDonald, and M. Polini, “Cavity quantum electrodynamics of strongly correlated electron systems: a no-go theorem for photon condensation”, Physical Review B **100**, 121109 (2019).

[141] O. Viehmann, J. von Delft, and F. Marquardt, “Superradiant phase transitions and the standard description of circuit qed”, Physical Review Letters **107**, 113602 (2011).

[142] T. M. Autry, G. Nardin, C. L. Smallwood, K. Silverman, D. Bajoni, A. Lemaıtre, S. Bouchoule, J. Bloch, and S. Cundiff, “Excitation ladder of cavity polaritons”, Physical Review Letters **125**, 067403 (2020).

[143] C. Ciuti, G. Bastard, and I. Carusotto, “Quantum vacuum properties of the intersubband cavity polariton field”, Physical Review B **72**, 115303 (2005).

[144] S. Blanes, F. Casas, J. Oteo, and J. Ros, “The magnus expansion and some of its applications”, Physics Reports **470**, 151–238 (2009).

[145] P. Potasz, A. D. Güçlü, and P. Hawrylak, “Spin and electronic correlations in gated graphene quantum rings”, Physical Review B **82** (2010).

[146] P. Giraud, “Study of the electronic structure of hexagonal boron nitride on metals substrates”, MA thesis (2012).

[147] B. Jorissen, L. Covaci, and B. Partoens, “Comparative analysis of tight-binding models for transition metal dichalcogenides”, SciPost Phys. Core **7**, 004 (2024).

[148] D. Manzano, “A short introduction to the lindblad master equation”, AIP Advances **10** (2020).

Code repositories

[R1] D. Dams, *Reproduction code repository*, `https://github.com/GRANADlauncher/granad-scripts/tree/main/thesis`, GitHub repository, 2025.

[R2] D. Dams, *Haldane model code repository*, `https://github.com/GRANADlauncher/granad-scripts/tree/main/haldane_array`, GitHub repository, 2025.

[R3] D. Dams, *Chiral polaritons code repository*, `https://github.com/david-dams/chiral-polaritons`, GitHub repository, 2025.

Appendices

A. GRANAD material specification

This appendix documents the domain-specific language (DSL) used by `GRANAD` to define tight-binding materials in a concise, readable, and composable way. The DSL follows a builder pattern: you instantiate a `Material` and then chain method calls to add structure, orbitals, and interactions.

A.1. Overview

A material specification typically includes:

1. **Lattice vectors** (basis of the Bravais lattice).
2. **Periodic boundary conditions** (which lattice vectors are repeated).
3. **Orbital placement** (species and positions within the unit cell).
4. **Single-particle interaction terms** (e.g., tight-binding Hamiltonian elements).

A minimal workflow:

1. Construct the object: `Material(name: str)`.
2. Define geometry: lattice constant and lattice basis; optionally set periodic directions.
3. Define orbitals: declare species (if required) and place orbitals at fractional coordinates with tags.
4. Define interactions: add single-particle effective terms as square matrices.

A.2. Core API

Construction

```
Material(name: str)
```

Geometry

```
.lattice_constant(a: float)
.lattice_basis(B: list[list[float]])   # rows are Cartesian lattice vectors
```

Optionally indicate which lattice vectors are periodically repeated (periodic boundary conditions).

Orbitals

```
.add_orbital_species(species: str, atom: str)
.add_orbital(position: tuple[float, float] | tuple[float, float, float],
             tag: str,
             species: str)
```

Positions are given in lattice (fractional) coordinates unless otherwise noted.

Interactions

```
.add_interaction(kind: str,
                 participants: tuple[str, str],
                 parameters: list[float],
                 expression: callable | None)
```

Currently supported `kind` values in the stable branch:

- `"hamiltonian"` (tight-binding matrix elements)
- `"coulomb"` (effective two-site potential entering a single-particle term)

A.3. Development Notes

In the development branch:

- Overlap matrices are supported via an additional `"overlap"` interaction kind.
- Declaring orbital species can be optional; orbitals may be added directly with tags and inferred attributes.

A.4. Example: Graphene

The snippet below specifies a standard p_z-only model for graphene.[1]

```
import jax.numpy as jnp

graphene = (
   Material("graphene")
   .lattice_constant(2.46)
   .lattice_basis([
      [ 1.0, 0.0, 0.0],
      [-0.5, jnp.sqrt(3.0) / 2.0, 0.0],
      [ 0.0, 0.0, 1.0], # optional out-of-plane vector
   ])
   .add_orbital_species("pz", atom="C")
   .add_orbital(position=( 0.0, 0.0), tag="sublattice_1", species="pz")
```

---

[1] `jnp.sqrt` refers to `jax.numpy.sqrt`. Replace with `numpy.sqrt` or a numeric constant if JAX is not used.

```
    .add_orbital(position=(-1/3, -2/3), tag="sublattice_2", species="pz"
        )
    .add_interaction(
        "hamiltonian",
        participants=("pz", "pz"),
        parameters=[0.0, -2.66], # onsite, nearest-neighbor hopping (eV)
    )
    .add_interaction(
        "coulomb",
        participants=("pz", "pz"),
        parameters=[16.522, 8.64, 5.333], # model-specific coefficients
        expression=lambda r: 1.0 / r + 0j # radial dependence (example)
    )
)
```

Notes on the example

- The lattice basis gives the 2D hexagonal primitive vectors in the xy-plane.
- Orbital positions are fractional coordinates relative to the provided basis.
- `parameters` encode model-specific numbers (e.g., onsite energies and hoppings in eV). Their interpretation depends on the chosen `kind` and any provided `expression`.
- The callable `expression` (when present) defines the distance dependence used to assemble matrix elements (here shown as $1/r$).

B. Sketch of Topological concepts

In this appendix, we briefly sketch core topological concepts underlying our example of the Haldane model in subsection 2.4.1 and our original analysis of electromagnetic sensitivity in finite topological nanoflakes in section 4.2. To this end, let $H(\lambda)$ denote the Hamiltonian of an insulator that depends smoothly on a control parameter λ. The projector onto the occupied IP states, as defined in Equation (2.13), is given by

$$P(\lambda) = \sum_{i,\text{occ}} |\phi_i(\lambda)\rangle \langle\phi_i(\lambda)| \, , . \tag{B.1}$$

As λ is varied, the Hamiltonian evolves continuously, and so does the ground-state projector, provided no band crossings occur. In such a case, two Hamiltonians are said to be topologically equivalent. If a band crossing does occur, the projector is ill-defined, because it is impossible to determine which band is occupied and which is not. If no continuous interpolation between the two Hamiltonians exists, the Hamiltonians belong to distinct topological classes. Each class is characterized by an integer invariant, and mismatched invariants across different phases give rise to robust edge states. This motivates the idea of *topological protection*: External effects like disorder or even electronic interactions will not alter the topological nature of the Hamiltonian as long as they do not induce band crossings. As such, we expect persistence of topological features even in the presence of these external interactions - a phenomenon which we explicitly demonstrate in section 4.2.

C. GRANAD materials

Table C.1.: Overview of built-in nanomaterial classes available in `GRANAD`.

Material	**Characteristics**	**Parameter source**
Graphene	Spinless, single p_z-orbital per atom with nearest-neighbor hopping	[70], Coulomb matrix elements from [145]
hBN	Spinless, single orbital model. Nearest-neighbor hopping between all involved atomic species	[146]
MoS_2	Spinless model including three p_z orbitals for sulfur and parity-even d orbitals for molybdenum	[147]

D. Lindblad and Phenomenological Damping

In this appendix we show that the phenomenological dissipator Equation (2.57) involved in the non-Hermitian dynamics of Equation (2.56) is a special case of the Lindblad dissipator Equation (2.58). To this end, we restate the two equations. The phenomenological dissipator is given by

$$\mathcal{D}_{\text{phenom}}[\tau(t)] = c\tau(t)\,, \tag{D.1}$$

where we have introduced the equilibrium-shifted 1RDM

$$\tau(t) = \gamma(t) - \gamma_0\,. \tag{D.2}$$

The Lindblad dissipator is given by

$$\mathcal{D}_{\text{Lindblad}}[\tau(t)] = \sum_{k=1}^{K^2-1} r_k \left(L_k \tau(t) L_k^\dagger - \tfrac{1}{2}\{L_k^\dagger L_k, \tau(t)\} \right)\,, \tag{D.3}$$

where we have performed a shift analogous to Equation (D.2). We now express the Lindblad dissipator in the energy eigenstates of the (effective) IP Hamiltonian, assuming them to be indexed in ascending order by energy. Since the operators L_k express transfer between these eigenstates, we can find for each k a pair of states i, j such that

$$L^k = |i\rangle\langle j|\,. \tag{D.4}$$

Excitation is described by $i > j$, while relaxation is described by the converse case. In the case where $i = j$, one talks about decoherence [148]. This induces a similar mapping for the rates r^k, which we relabel as r_{ij}. Consequently, we have

$$\langle a|D_{\text{Lindblad}}[\tau]|b\rangle = \delta_{ab}\sum_i r^{ia}\tau_{ii}(t) - \frac{1}{2}\cdot\sum_j (r^{aj}\tau_{ab}(t) + \tau_{ab}(t)r^{bj}). \tag{D.5}$$

The first term is a matrix-vector multiplication and thus incompatible with the scalar relation $\mathcal{D}_{\text{phenom}}[\tau(t)] = c\tau(t)$ of the phenomenological dissipator. We can get rid of this term by exploiting $\text{Tr}[\tau(t)] = 0$, if we impose

$$r^{ia} = r\,. \tag{D.6}$$

Plugging this back into Equation (D.5), we get

$$\langle a|D_{\text{Lindblad}}[\tau(t)]|b\rangle = -\frac{1}{2}\cdot\sum_j (r\tau_{ab}(t) + \tau_{ab}(t)r) = -Nr\tau_{ab}(t)\,, \tag{D.7}$$

which means that the two approaches are equivalent under the substitution Equation (D.2), provided that

$$c = -rN\,. \tag{D.8}$$

E. Gaussian Drives For Chiral Cavities

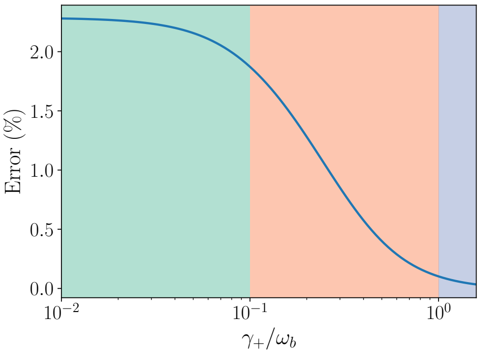

Figure E.1.: Percentage error in energy transfer efficiency, computed for delta and Gaussian excitations. Parameters as in Figure 6.6 of the main text.

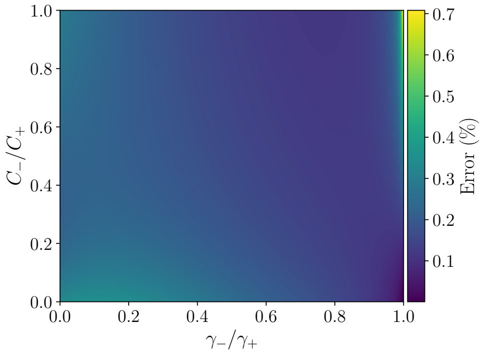

Figure E.2.: Percentage error in energy transfer efficiency, computed for delta and Gaussian excitations. Parameters as in Figure 6.8 of the main text.

In this appendix, we generalize the expression for the energy transfer efficiency to chiral enantiomers given in subsection 6.3.2 to the case of narrow Gaussian drives. For a normalized Gaussian drive $f(t) = \frac{1}{\sqrt{2\pi\sigma^2}} e^{-t^2/(2\sigma^2)}$ (with the same C_ℓ couplings), Equation (6.36) gains an extra factor $e^{-8\pi^2\sigma^2\omega_j^2}$, *i.e.*,

$$\phi_j \;\rightarrow\; \phi_j \, e^{-8\pi^2\sigma^2\omega_j^2}. \tag{E.1}$$

The δ -pulse approximation is thus accurate whenever $\sigma \ll T_j \equiv 2\pi/\omega_j$; numerically, we find robust qualitative agreement up to $\sigma \sim 0.1 \min_j T_j$ and present results in Figure E.1 and Figure E.2 for a Gaussian pulse with a width of $1\,\%$ of the smallest polaritonic timescale.

Selbstständigkeitserklärung

Eidesstattliche Versicherung gemäß § 13 Absatz 2 Ziffer 3 der Promotionsordnung des Karlsruher Instituts für Technologie (KIT) für die KIT-Fakultät für Physik:

1. Bei der eingereichten Dissertation zu dem Thema
   “Light–Matter Interactions in 2D Nanostructures and Chiral Cavities”
   handelt es sich um meine eigenständig erbrachte Leistung.
2. Ich habe nur die angegebenen Quellen und Hilfsmittel benutzt und mich keiner unzulässigen Hilfe Dritter bedient. Insbesondere habe ich wörtlich oder sinngemäß aus anderen Werken übernommene Inhalte als solche kenntlich gemacht.
3. Die Arbeit oder Teile davon habe ich ~~wie folgt/~~ bislang nicht[1] an einer Hochschule des In- oder Auslands als Bestandteil einer Prüfungs- oder Qualifikationsleistung vorgelegt.

   ~~Titel der Arbeit:~~

   ~~Hochschule und Jahr:~~

   ~~Art der Prüfungs- oder Qualifikationsleistung:~~
4. Die Richtigkeit der vorstehenden Erklärungen bestätige ich.
5. Die Bedeutung der eidesstattlichen Versicherung und die strafrechtlichen Folgen einer unrichtigen oder unvollständigen eidesstattlichen Versicherung sind mir bekannt.

Ich versichere an Eides statt, dass ich nach bestem Wissen die reine Wahrheit erklärt und nichts verschwiegen habe.

Ort und Datum Unterschrift

---

[1] Nicht Zutreffendes streichen. Bei Bejahung sind anzugeben: der Titel der andernorts vorgelegten Arbeit, die Hochschule, das Jahr der Vorlage und die Art der Prüfungs- oder Qualifikationsleistung.